UNIVERSITÀ DEGLI STUDI DI PADOVA

UNIVERSITA' DEGLI STUDI DI PADOVA

Dipartimento di Ingegneria Industriale DII

Corso di Laurea Magistrale in Ingegneria dell'Energia Elettrica

Advanced tools for plasma control in magnetic confinement fusion devices

Relatore: Prof. Paolo Bettini

Correlatori: Domenico Abate, Ph.D.
Matteo Bonotto, Ph.D.

Laureando
Nicola Ostoich - 1238374

Anno Accademico 2021/2022

Sommario

Nel contesto dell'esperimento in via di sviluppo RFX-mod2, questo lavoro mira attentamente a valutare possibili condizioni critiche nella ricostruzione in tempo reale dei parametri di plasma (mediante il calcolo di momenti di ordine inferiore della densità di corrente toroidale), ogni qualvolta il nuovo set dei sensori di campo magnetico poloidale dovesse presentare un guasto.

La valutazione viene eseguita su tre scariche sperimentali di RFX-mod e due simulate numericamente per future operazioni di RFX-mod2. Queste presentano varie forme plasma, con nullo singolo superiore, nullo singolo inferiore, limiter ed a triangolarità negativa. Questo viene fatto per verificare se la forma del plasma e le caratteristiche dell'equilibrio in qualche modo influenzino la ricostruzione dei parametri in tempo reale.

Sono state analizzate tutte le possibili configurazioni comprese tra 1 e 12 sensori guasti, fornendo una panoramica completa della validità del metodo di ricostruzione mediante i momenti della densità di corrente toroidale in ogni possibile scenario. Quindi, è stata eseguita un'ulteriore analisi presentante del rumore all'interno delle misure su alcune configurazioni chiave, per dimostrare la robustezza del metodo stesso.

Il lavoro è organizzato come segue. La prima sezione fornisce un'introduzione riguardante la natura della fusione termonucleare e illustra le soluzioni più promettenti per il suo sviluppo. In particolare, si descriverà la fusione a confinamento magnetico in configurazione tokamak, fornendo una panoramica dei principi di funzionamento.

La seconda sezione approfondisce gli aspetti riguardanti il problema magnetostatico e fornisce le informazioni relative alla soluzione del problema free-boundary di equilibrio. In particolare, viene introdotto il codice FRIDA per la soluzione numerica del problema magnetostatico. I dati forniti dall'output del codice serviranno quindi per ricavare le misure virtuali dei sensori di campo magnetico di RFX-mod2.

La terza sezione fornisce un modello per la ricostruzione dei parametri di plasma a partire dalle misure dei sensori di RFX-mod2: il calcolo dei momenti della densità di corrente toroidale di ordine inferiore. L'obiettivo è capire come ricostruire i parametri di plasma, ossia la corrente totale di plasma e la posizione del centroide, quando è presente un numero ridotto di misure, come accade nelle applicazioni reali.

La quarta sezione fornisce una descrizione dell'esperimento RFX-mod2, considerando le principali differenze rispetto al suo predecessore RFX-mod. Particolare attenzione viene data alla descrizione delle operazioni tokamak.

La quinta sezione illustra gli equilibri utilizzati in questo lavoro, scelti tra diverse forme di plasma come precedentemente accennato.

Infine, il sesto capitolo fornisce i risultati dell'analisi della ricostruzione dei parametri di plasma considerando il potenziale guasto di diversi sensori di campo poloidale RFX-mod2. In particolare sono state analizzate tutte le combinazioni di sensori guasti a seconda delle loro posizioni nella macchina.

Abstract

In the context of the in-development RFX-mod2 experiment upgrade, this work carefully aims to evaluate possible critical conditions in real-time plasma parameters reconstruction (by means of computation of lower-order moments of toroidal current density), whenever the new set of poloidal magnetic field sensors would encounter some failures.

The evaluation is performed on three experimental RFX-mod discharges and two numerically defined for future RFX-mod2 operations. Among them, various types of plasma shapes are present, with upper single null, lower single null, limiter plasma and negative triangularity. This is done to verify whether plasma shape and equilibrium characteristics might affect real-time parameters reconstruction.

All the possible configurations between 1 and 12 faulty sensors have been analysed, giving a complete overview of moment reconstruction method behaviour in every possible scenario. Then, a further noise analysis has been performed over some key configurations, to prove the robustness of the method itself.

The work is organized as follows. The first section provides an introduction concerning the nature of thermonuclear fusion and illustrates the most promising solutions for its development. In particular, it will be described the magnetic confinement fusion configuration appealed as *tokamak*, giving an overview of the operating principles.

The second section deepens the aspects of the magnetostatic problem and provides the informations concerning the solution of the free-boundary equilibrium problem. In particular, is introduced the FRIDA code for the numeric solution of the magnetostatic problem. Data retrieved by the code output will then be utilized to obtain virtual measurements on RFX-mod2 magnetic sensor set.

Third section provides a model for plasma parameters reconstruction from the magnetic sensors of RFX-mod2: the computation of lower order moments of the toroidal current density. The focus is put on understanding how to retrieve reliable plasma parameters, i.e. total plasma current and centroid position, when a reduced number of measurement is present, as happens in practical applications.

Fourth section gives a description of the RFX-mod2 experiment, considering the main differences between its predecessor RFX-mod. Particular attention is given in describing the tokamak operations.

Fifth section illustrates the equilibria utilized in this work, chosen among different plasma shapes as previously mentioned.

Finally, the sixth chapter provides the results of the analysis of plasma parameters reconstruction considering the potential failure of several RFX-mod2 poloidal field sensors. In particular, all combinations of faulty sensors are analysed according to their positions in the machine.

Contents

SECTION 1

1 Introduction

1.1 World energy problem

Anthropogenic emissions of carbon dioxide and other greenhouse gasses are the primary driver of climate change. The energy sector must be at the front line of efforts to tackle climate change since the combustion of fossil fuels contributes around two-thirds of global emissions of global greenhouse gas emissions and the bulk of CO_2 emissions [1]. A great reduction of fossil fuels usage to generate electricity is mandatory contextually with a sustained and complete shift to clean energy technologies based on low-carbon sources of energy.

In the last decades, the use of renewable energy sources like hydropower, photovoltaic and wind energy has signed a drastic growth, passing from 0.7 TW installed power in 2000 up to 2.70 TW in 2020 (Fig. 1.1) [2]. However, these sources have intrinsic limits in available power (for hydropower) and variability (for solar and wind), suggesting that other kinds of clean generation strategies must be found; specially to guarantee a baseload generation support [3]. Solar and wind, in fact, are not suitable for baseload generation due to their intrinsic variability, and hydropower has limits on installed capacity, depending mainly on the geographical location.

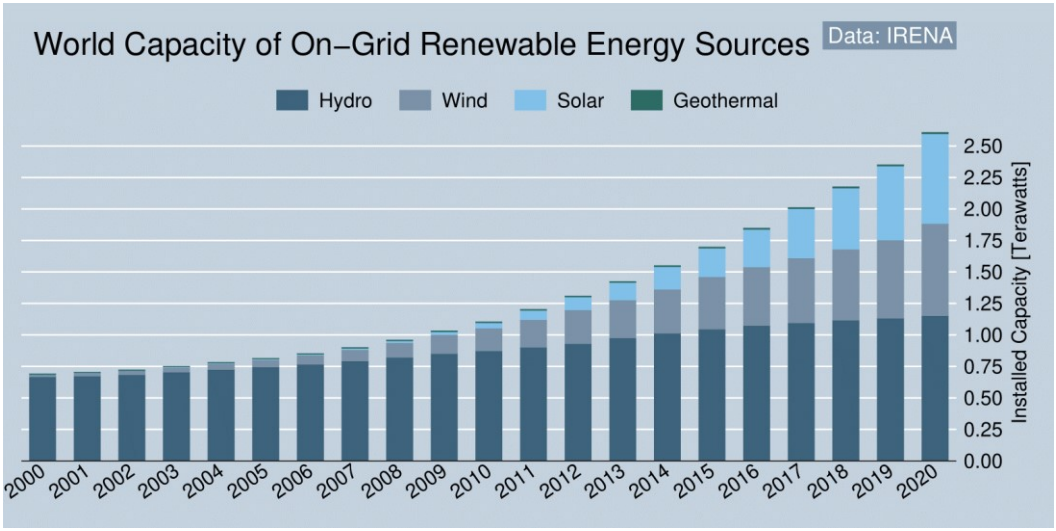

Fig. 1.1: Renewables installed power 2000-2020 [2]

In this context nuclear power can be seen as a concrete possible solution to world energy problem. Many ways of extracting energy directly from atomic nuclei can be exploited and, depending on the type of process, one could refer to nuclear fission or nuclear fusion. The first relies in the rupture of heavy atomic nuclei while fusion, instead, extracts energy from the merging of light atomic nuclei.

The amount of energy released in nuclear reactions is related to the strong nuclear interaction that holds atomic nuclei together. This energy between the single nucleus formants can be quantified and expressed in terms of energy per single nucleon (Fig 1.2) [4], or *binding energy per nucleon*. The presented curve shows how light and heavy nuclei are bound weakly than intermediate elements. This condition arises from a geometric competition between the strong short-range nuclear force and the weak long-range Coulomb force.

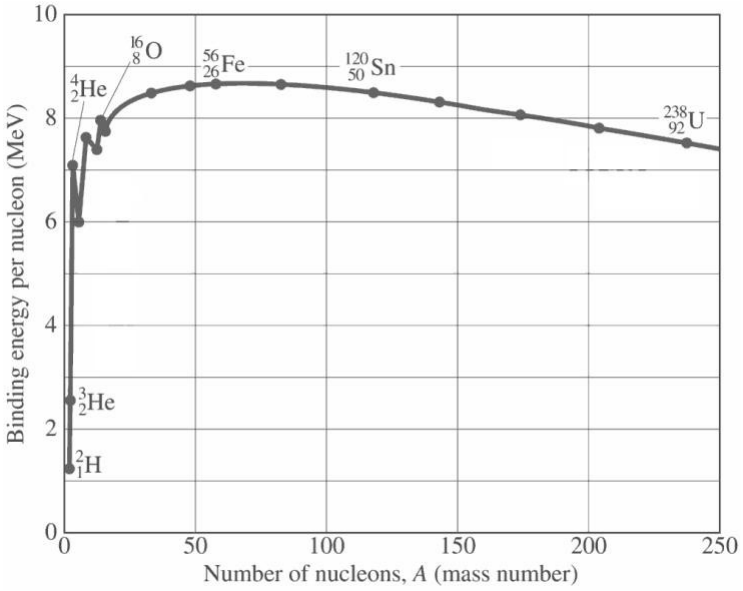

Fig. 1.2 Binding energy per nucleon

Binding energy per nucleon has a maximum around ^{56}Fe (being it actually the most stable nucleus in nature). On the left side of the graph there are lighter atomic nuclei which primary could intervene in fusion reactions, and, on the right side, heavier nuclei that could most probably undergo fission reactions.

In all these processes the energy is extracted by the mass defect between the reactants and the products, obeying the famous Einstein's relation:

$$E = mc^2$$

Hence the mass of the reactants is higher than the mass of the products and the mass defect is released in the process under the form of kinetic energy of the products and/or electromagnetic radiation.

In the last century, one particular kind of nuclear reaction has been exploited: the fission of uranium-235. This process has concrete advantages in terms of CO_2 emissions and baseload generation, therefore it should have a key role in our near-future generation scenario. However, it presents severe drawbacks that could set limits in its exploitation. In particular, nuclear fission suffers of fuel depletion, like fossil fuels [5], and presents various safety aspects that make it unattractive. Among them: the waste product handling, the possibility of having an exponential

reaction and the potential production of nuclear weapons by enriching nuclear fuel. This inevitably leads to a small penetration of nuclear power in our energy generation scenario (Fig. 1.3) [1] (even though it could have a huge potential in baseload support substituting fossil-fuels plants [3]).

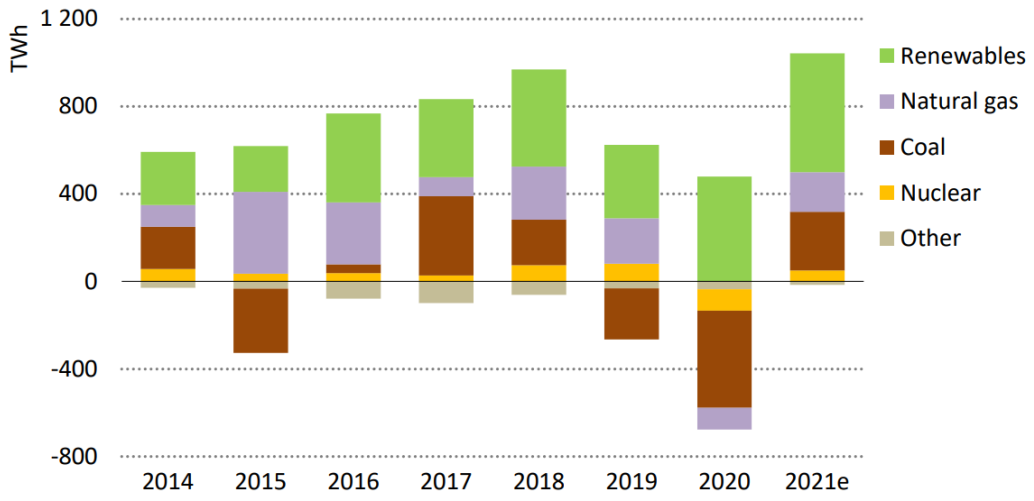

Fig. 1.3 Energy generation by power source 2014-2021 [1]

1.2 Thermonuclear Fusion

The other kind of nuclear reaction is the nuclear fusion and, contrary to nuclear fission, it requires a set of more extreme environmental conditions to allow the reaction to occur. The main challenge that has to be faced in order to accomplish fusion on a large scale, and possibly making it commercially available, is overcoming the electrostatic repulsion forces that acts against the merging of the nuclei.

1.2.1 Coulomb potential

In order to achieve nuclear fusion reactions, the nuclei must have sufficiently high energies to overcome the repulsive Coulomb barrier (Eq. 1.1), whose associated Coulomb force diverts the particle orbits and greatly reduces the likelihood of a nuclear reaction. This is the strategy behind all current fusion research.

$$W = \frac{Z_1 Z_2 e^2}{4\pi\varepsilon_0 r_m} \tag{1.1}$$

In Eq. (1.1), Z_1 and Z_2 are the atomic numbers of the interacting nuclei, e is the unit charge and r_m is the distance between nuclei's centres at which attractive nuclear forces becomes dominant (Fig. 1.4).

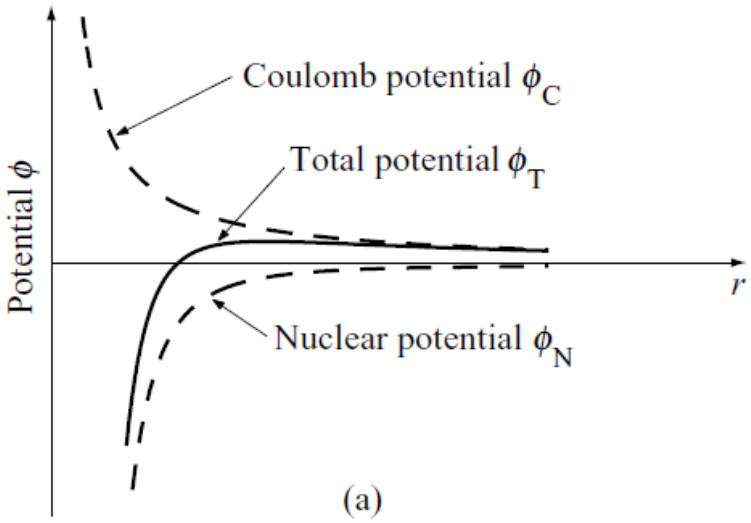

Fig 1.4 Coulomb, nuclear and total potential

Coulomb barrier is therefore proportional to Z^2, meaning that light atomic nuclei could more likely intervene in fusion reactions. This fact suggests a preferable choice in reactants as the elements present in the leftmost part of Fig. 1.2.

Nuclear fusion already happens in nature, in the core of all the stars of the universe, fusing H_1^1 nuclei (i.e. protons) in a chain reaction until an helium atom is obtained (or in older stars other processes involving heavier nuclei up to Fe^{56}, then fusion becomes no more energy-convenient causing the death of the star). In this case the reaction is possible thanks to gravity that compresses the hot core to extremely high densities, pressures and temperatures bringing the nuclei close enough that Coulomb potential barrier is overcomed. This is called inertial confinement fusion.

The fusion of protons in the Sun is possible because of the extreme conditions in its centre: pressures of about 150 billion bar and temperatures of 15 M°C, caused by the gravitational forces from a mass that is about 330,000 times larger than that of the Earth.

The core of our Sun is esteemed to have a density of 160 g/cm^3, a value that cannot be replicated on Earth. Nevertheless, inertial confinement can be performed in laboratory through a different way involving an intense bombardment of a target by means of powerful lasers; several experiments are studying the feasibility of this fusion approach.

A different and much more promising approach to fusion is the Magnetic Confinement Fusion (MCF). This relies on rising the temperature of the reactants up to thermonuclear temperatures (e.g. 100 million °C), when the kinetic energy of the thermal particles is enough to overcome the electrostatic repulsion and

bring the nuclei close enough to fuse; the resulting process is called *thermonuclear fusion*. At these temperatures the fuel is fully ionized, becoming a *plasma*, a high-temperature collection of electrons and ions that can be dominated by electromagnetic forces. In fact, plasma is a hot core of gas that tends to expand; magnetic fields and currents must exist in order to balance this expansion force with the final aim to confine the particles at a desired location in the vacuum chamber of the MCF experiment.

1.2.2 Fusion reactions and approaches

A key parameter to define the feasibility of a nuclear reaction is the cross-section σ. This has the dimension of an area and is linked to the probability that a nuclear reaction could happen, more precisely it depends on the interaction time of the in a determined area.

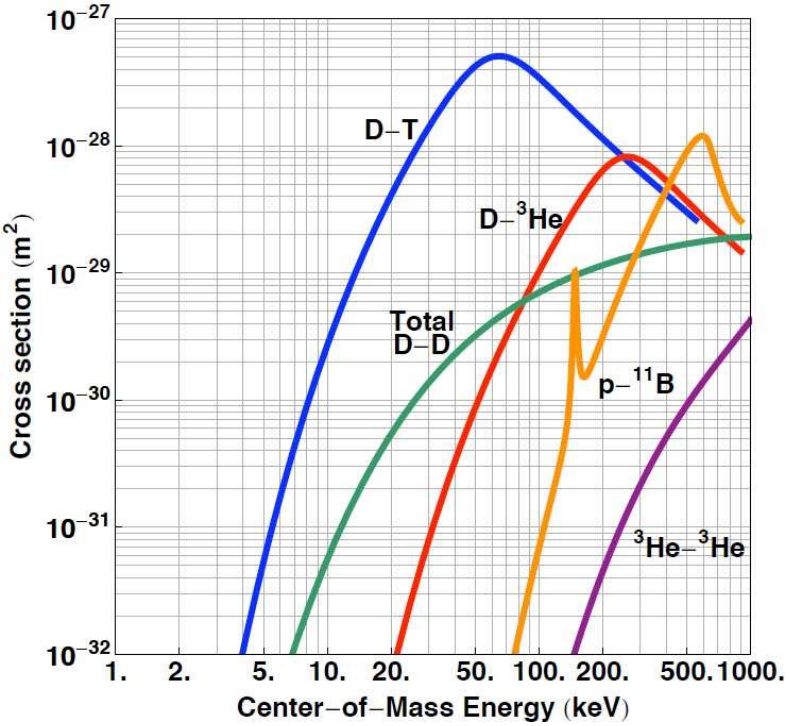

Fig 1.5: Cross-section of main fusion reactions as a function of temperature (i.e. energy) [keV]

$$
\begin{aligned}
D_1^2 + T_1^3 &\rightarrow \alpha + \mathrm{n} + E_{DT} && E_{DT} = 17{,}6\ \mathrm{MeV} \\
D_1^2 + D_1^2 &\rightarrow T_1^3 + \mathrm{p} + E_{DD'} && E_{DD'} = 4{,}03\ \mathrm{MeV} \\
D_1^2 + D_1^2 &\rightarrow He_2^3 + \mathrm{n} + E_{DD''} && E_{DD''} = 3{,}27\ \mathrm{MeV} \\
D_1^2 + He_2^3 &\rightarrow \alpha + \mathrm{p} + E_{DHe} && E_{DHe} = 18{,}3\ \mathrm{MeV} \\
He_2^3 + He_2^3 &\rightarrow \alpha + 2\mathrm{p} + E_{HeHe} && E_{HeHe} = 12{,}86\ \mathrm{MeV} \\
p + B_5^{11} &\rightarrow 3\alpha + E_{pB} && E_{pB} = 8{,}7\ \mathrm{MeV}
\end{aligned}
\tag{1.2}
$$

Comparing experimental cross-section data (Fig. 1.5), the simpler reaction which could be experimented (Eq. 1.2) is the deuterium-tritium reaction (D-T) as it presents the highest σ to accomplish the fusion.

The release of $17{,}6\,MeV$ corresponds to $3{,}52\,MeV$ per nucleon, which macroscopically is equivalent to $338 \cdot 10^6\,MJ/kg$ of fuel.

Nevertheless, despite D-T reaction presents the highest cross-section, it suffers from the tritium supply point of view. In fact, since tritium is a radioactive isotope with a half-life of only about 12 years, there is no natural tritium to be found on Earth. A solution for the tritium demand could be found in using a widely available on Earth isotope of lithium (Li^6), which could breed tritium by absorbing a neutron [6].

Alternatively, a full D-D reaction could minimize the fuel problem, since deuterium is naturally present in our planet and could be majorly found linked to oxygen in the so called "heavy water". A fraction of just 0.0156% (1 atom in 6420) of H_2 is deuterium, but considering a planetary scale, it results in a quite abundant element [7]. However, as shown in Fig 1.3, the DD cross-section impose even more critical conditions to sustain a fusion reaction of this kind.

Another important aspect to be considered in thermonuclear fusion experiments, is the neutron production. This is fundamental to extract thermal energy by its braking in the first wall, but, at the same time, it requires a sophisticated structure in order to handle material activation and radiation damage resulting from high-energy neutrons.

There exist reactions that do not produce neutrons, hence all the products could be confined within magnetic fields. This particular aneutronic reactions, like p-B_{11}, D-He^3 or He^3-He^3 may help simplify the containment structure, but drawbacks regarding the small cross-section and fuel supply (helium-3) are still present.

1.2.3 Power balance in magnetic confinement fusion

A simple analysis to assess the conditions to sustain a thermonuclear fusion reaction relies in the evaluation of a 0D power balance [8].

Considering the D-T reaction of MCF, a first hypothesis of no net power output is set, which implies that power input equals power output (assuming that reagents that have incurred in a fusion reaction could not be confined)

$$P_{in} = P_{out} \tag{1.3}$$

Power input P_{in} consists of two terms: external power P_{ext}, used to sustain the reaction, and P_N, the nuclear power produced by fusion itself, which contributes to

plasma heating. The latter depends on the D-T reaction cross-section σ and temperature (expressed as particles velocity v). Relations can be written as follows:

$$P_{in} = P_N + P_{ext}, \qquad P_N = \frac{n^2}{4}\langle\sigma v\rangle E_{DT}$$

where E_{DT} is the energy released by the DT reaction (Eq. 1.2) and $\frac{n^2}{4}\langle\sigma v\rangle$ is the reaction rate. The latter is defined as $\langle\sigma v\rangle n_1 n_2$, where $\langle\sigma v\rangle$ is the average value of the product between cross-section and particles velocity, and it can be demonstrated to present a maximum when $n_1 = n_2 = \frac{n}{2}$.

Power output is then composed by transport losses P_T, that depends on the energy confinement time τ_E, and bremsstrahlung losses P_B, that are due to irradiation generated by acceleration of charged particles.

$$P_{out} = P_N + P_T + P_B, \qquad P_T = \frac{3nkT}{\tau_E}, \qquad P_B = bn^2\sqrt{T}$$

The final assumption is that $P_{ext} = \eta P_{out}$, where η is the efficiency of energy conversion system.

The power balance equation (1.3) can be solved with respect to the term $n\tau_E$, leading to

$$n\tau_E = \frac{3kT}{\frac{1}{4}\left(\frac{\eta}{1-\eta}\right)\langle\sigma v\rangle E_{DT} - b\sqrt{T}}$$

This relation presents a minimum of the $n\tau_E$ product with respect to the temperature, representing an optimal working point. An even better parameter to describe whether thermonuclear fusion could happen, is found in the triple product $n\tau_E T$, and its minimum takes the name of *ignition criterion*.

Recalling what stated before about the Sun core, it is clear that a density $n = 160\,\frac{g}{cm^3}$ is not practicable, but what the ignition criterion tells us is that the others two parameters of the triple product $n\tau_E T$ can be chosen appropriately to overcome feasibility issues. In fact, rising the temperature, the density parameter can be dropped down to values of practical interest for plasma handling.

$$T \approx 20\ keV, \quad n \approx 10^{20} m^{-3}, \quad \tau_E \approx 1s$$

1.3 Plasma Magnetic Confinement

The simplest magnetic field geometry for MCF is a straight cylinder. However, this geometry has the problem that plasma particles could escape from both ends. This escaping can be greatly reduced by forming two “magnetic mirrors”, which

simply means that the field strength is increased at both ends using additional magnetic coils.

The obvious solution to prevent end losses, is to wind the cylinder onto itself: in other words, to have a configuration with a toroidal shape.

Given a cylindrical coordinates reference system (r, ϕ, z), we define the z-axis to be positioned on the axis of symmetry of the torus (Fig. 1.6). This way, an assumption of axisymmetry could be stated and we can refer to the *poloidal plane* (r, z) for any angle ϕ.

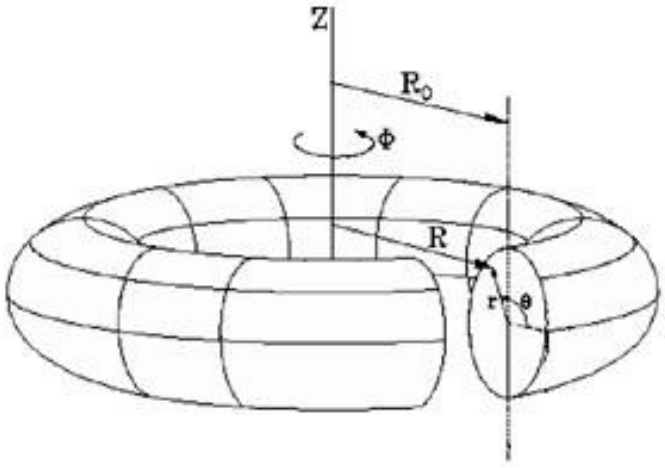

Fig 1.6: Cylindrical coordinates for MCF

To practically obtain confinement in this type of geometry, a set of magnetic coils (Fig. 1.7a) around the toroidal vacuum chamber has to produce a field in the toroidal direction ϕ, the so-called Toroidal Field coils (TF). However, such a system of coils generates a magnetic field that is stronger near the machine's vertical symmetry axis, because at that position the coils are much closer to each other than in the outer part of the torus. This causes a vertical drift of the particles that finally leads to charge build-up and a consequent plasma loss. This drift can be compensated if the magnetic field lines, instead of being simply circular, are wound around the torus in such a way that the drift in the outer part of the trajectory compensates that in the inner part. The “amount of field-line winding” around the torus is called the *rotational transform*. After a certain number of turns around the torus, the field line has covered a surface, called the *magnetic surface* (Fig. 1.7b); every such surface is characterized by a winding number, called the safety factor q, equal to the number of turns the field line makes in the toroidal direction per turn in the cross-sectional poloidal direction.

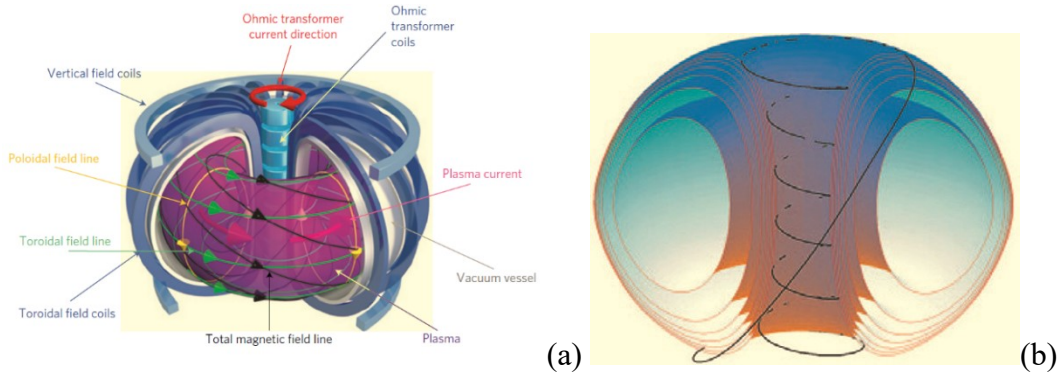

Fig. 1.7: (a) MCF coil configuration, (b) magnetic surfaces [9]

Moreover, a set of coils disposed in the toroidal direction generates magnetic field in the poloidal plane θ, the Poloidal Field coils (PF). A special set of poloidal field coils called Ohmic Heating coils or Magnetizing coils (M) are placed within the torus to induce the plasma current by transformer effect with a big flux swing. The remaining active PF coils, instead, provides horizontal stability, generating forces on the plasma and preventing its natural outward displacement.

The two main magnetic configurations based on an induced current-carrying plasma are the Tokamak and the Reversed Field Pinch (RFP).

1.3.1 Tokamak

The most remarkable magnetic configuration in MCF experiments is the Tokamak [8], [9]. This is an axisymmetric configuration with a large toroidal magnetic field produced by external TF coils and a significant toroidal current flowing in the plasma itself. The poloidal component of the magnetic field is generated by the plasma current which is induced by transformer action of the M coils. The related inductive voltage (i.e. loop voltage) drives and sustains the plasma current along the plasma torus (the secondary of the transformer). The Tokamak configuration is characterized by a prevalence of the toroidal magnetic field component B_ϕ with respect to the poloidal one, produced by external coils, over the B_θ one, practically about 10 times higher:

$$B_\phi \approx 10 B_\theta \tag{1.4}$$

1.3.2 Reversed Field Pinch

The reversed field pinch (RFP) [10], [11] is a particular kind of toroidal pinch configuration in which the plasma is still confined by a combination of a poloidal and toroidal magnetic field, but the magnitude of toroidal field is comparable with the poloidal one (Fig. 1.8). Toroidal field in RFP is in fact mainly generated by a combination of poloidal plasma currents and currents flowing in external coil, thus allowing the utilization of simpler and cheaper TF coils. Poloidal field, instead, is mainly produced by the induced toroidal plasma current.

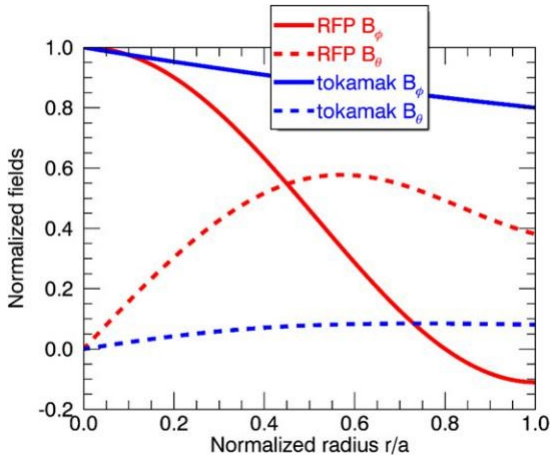

Fig. 1.8 Toroidal (B_ϕ) and poloidal (B_θ) magnetic field profiles in RFP and Tokamak

SECTION 2

2 Plasma equilibrium in axisymmetric conditions

Plasma is described by Magneto Hydro Dynamics (MHD) theory [13], where, for simplicity, the existence of different particles (e^-, i^+) is neglected, and plasma is treated as a single conducting fluid. Maxwell equations give reason of the interaction with external fields, and Navier-Stokes equation model fluid dynamics.

To further simplify the model, plasma is treated as ideally conductive, leading to what is called *ideal MHD*. The quantities involved are the electric field $\boldsymbol{E}$; magnetic field $\boldsymbol{B}$; current density $\boldsymbol{J}$; fluid velocity $\boldsymbol{v}$; pressure p; mass density ρ_m.

$$\frac{\partial \rho_m}{\partial t} + \nabla(\rho_m \boldsymbol{v}) = 0 \tag{2.1}$$

$$\rho_m \frac{d\boldsymbol{v}}{dt} = \rho \boldsymbol{E} + \boldsymbol{J} \times \boldsymbol{B} - \nabla p \tag{2.2}$$

$$\frac{d}{dt}\left(\frac{p}{\rho_m^{\gamma}}\right) = 0 \tag{2.3}$$

$$\boldsymbol{E} + \boldsymbol{v} \times \boldsymbol{B} = 0 \tag{2.4}$$

$$\nabla \times \boldsymbol{B} = \mu_0 \boldsymbol{J} \tag{2.5}$$

$$\nabla \times \boldsymbol{E} = -\frac{\partial \boldsymbol{B}}{\partial t} \tag{2.6}$$

$$\nabla \cdot \boldsymbol{B} = 0 \tag{2.7}$$

From this set of equations, it is possible to derive a further simplification that focuses solely on plasma equilibrium, considering a condition where inertial effects could be neglected and net force acting on the plasma is zero.

2.1 The Grad-Shafranov equation

Plasma equilibrium relies on two main assumptions:

- All quantities are time-independent: $\partial/\partial t = 0$
- Plasma is assumed to be static: $\boldsymbol{v} = 0$

The second one imposes that Eq. (2.4) becomes:

$$\boldsymbol{E} = 0$$

furthermore simplifying Eq. (2.2).

The set of equations (2.1-7), hence, can be reduced to

$$\begin{aligned} \boldsymbol{J} \times \boldsymbol{B} &= \nabla p \\ \nabla \times \boldsymbol{B} &= \mu_0 \boldsymbol{J} \\ \nabla \cdot \boldsymbol{B} &= 0 \end{aligned} \tag{2.8}$$

Consider a generic cylindrical coordinate system (r, ϕ, z) as shown in figure 1.3. In this reference system the problem of the ideal MHD equilibrium for the plasma configuration is addressed.

Referring to a generic poloidal plane (r, z) as shown in Fig. 2.1,

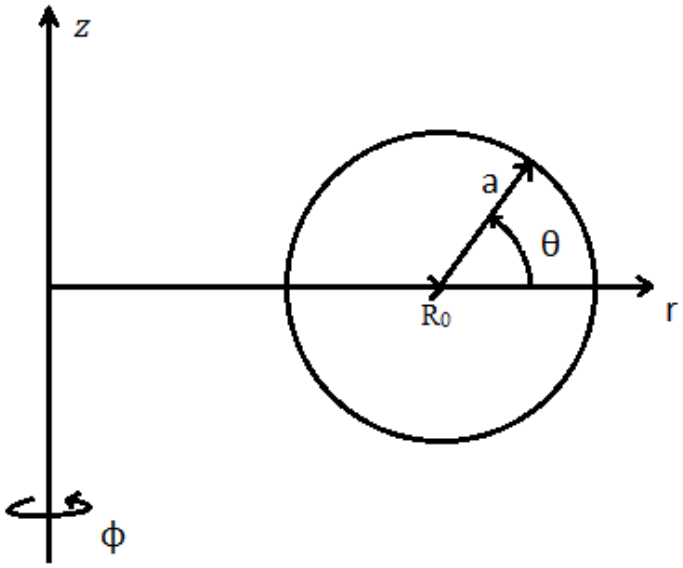

Fig. 2.1 Poloidal plane (r, z)

Eq. (2.7) can be written as

$$\frac{1}{r}\frac{\partial}{\partial r}\,(rB_r) + \frac{\partial B_z}{\partial z} = 0$$

and a function $\psi(r,z) : \mathbb{R}^2 \rightarrow \mathbb{R}$, that takes the name of *normalized poloidal flux function*, is so defined such as the two components of the poloidal field can be expressed as follows:

$$B_r = -\frac{1}{r}\frac{\partial \psi}{\partial z}\,, \qquad B_z = \frac{1}{r}\frac{\partial \psi}{\partial r} \tag{2.9}$$

Considering $\boldsymbol{u}_\phi$ as toroidal unit vector, the total magnetic field can be written as the vectorial sum of toroidal component B_ϕ and poloidal component B_θ:

$$\boldsymbol{B} = B_\phi \boldsymbol{u}_\phi + \boldsymbol{B}_\theta \tag{2.10}$$

with $\boldsymbol{B}_\theta = \frac{1}{r}(\nabla\psi \times \boldsymbol{u}_\phi)$

Current density can also be written as the vectorial sum of toroidal and poloidal components.

$$\boldsymbol{J} = J_\phi \boldsymbol{u}_\phi + \boldsymbol{J}_\theta \tag{2.11}$$

and a similar parametrization, as what was done for the magnetic field, could be implemented also for the *poloidal current density*; so a function $f(r,z)$, defined as $f = \frac{rB_\phi}{\mu_0}$, is introduced as:

$$J_r = -\frac{1}{r}\frac{\partial f}{\partial z}\,, \qquad J_z = \frac{1}{r}\frac{\partial f}{\partial r} \tag{2.12}$$

Then, from Ampere's law (2.5):

$$J_r = -\frac{1}{\mu_0}\frac{\partial B_\phi}{\partial z}, \qquad J_z = \frac{1}{\mu_0}\frac{1}{r}\frac{\partial}{\partial r}(rB_\phi) \tag{2.13}$$

Assumed to be $f = f(\psi)$ and $p = p(\psi)$, it could be stated that:

$$\boldsymbol{J} \times \boldsymbol{B} = \nabla p \rightarrow J_\theta \times \boldsymbol{u}_\phi B_\phi + \boldsymbol{u}_\phi J_\phi \times B_\theta = \nabla p \tag{2.14}$$

$$\frac{1}{r}(\nabla f \times \boldsymbol{u}_\phi) \times \boldsymbol{u}_\phi B_\phi + \boldsymbol{u}_\phi J_\phi \times \frac{1}{r}(\nabla\psi \times \boldsymbol{u}_\phi) = \nabla p \tag{2.15}$$

$$\frac{-B_\phi}{r}\nabla f + \frac{-J_\phi}{r}\nabla\psi = \nabla p \tag{2.16}$$

$$J_\phi = R\frac{dp}{d\psi} + B_\phi\frac{df}{d\psi} \tag{2.17}$$

The toroidal magnetic field component can be eliminated thanks to the relation $f = \frac{rB_\phi}{\mu_0}$

$$J_\phi = R\frac{dp}{d\psi} + \frac{\mu_0}{r}f\frac{df}{d\psi} \tag{2.18}$$

and toroidal current density can be eliminated using Ampere's law (2.5):

$$\mu_0 J_\phi = \frac{\partial B_r}{\partial z} - \frac{\partial B_z}{\partial r}$$

then substituting (2.9):

$$\mu_0 J_\phi = \frac{1}{r}\frac{\partial^2\psi}{\partial z^2} - \frac{\partial}{\partial r}\left(\frac{1}{r}\frac{\partial\psi}{\partial r}\right)$$

At this point the **Grad-Shafranov equation** (GSE) is obtained.

$$\frac{1}{r}\frac{\partial^2\psi}{\partial z^2} - \frac{\partial}{\partial r}\left(\frac{1}{r}\frac{\partial\psi}{\partial r}\right) = -\mu_0 r^2 p'(\psi) - \mu_0^2 f(\psi)f'(\psi) \tag{2.19}$$

Introducing then the *Shafranov operator*

$$\Delta^{*}\# = \frac{1}{r}\frac{\partial^{2}\#}{\partial z^{2}} - \frac{\partial}{\partial r}\left(\frac{1}{r}\frac{\partial \#}{\partial r}\right)$$

eq. (2.21) can be written in a more compact form

$$\Delta^{*}\psi = -\mu_0 r^2 p' - \mu_0^2 f f' \tag{2.20}$$

The constant value contours of the solution $\psi(r,z)$ give the shape of the magnetic surfaces on the poloidal plane.

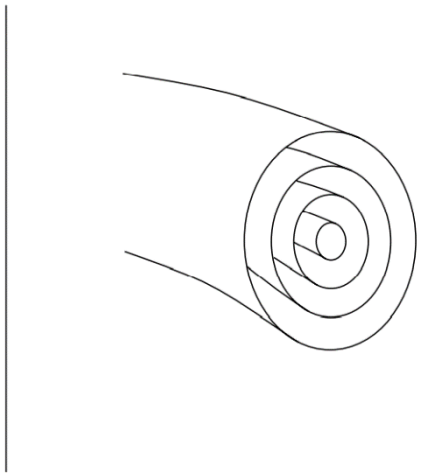

Fig. 2.2: Magnetic flux surfaces

This fact descends from the momentum equation of the system (2.8). Since ∇p is, by definition, perpendicular to the $p = \text{const}$ contours, it follows that $\boldsymbol{J}$ and $\boldsymbol{B}$ are orthogonal to the pressure gradient, so

$$\boldsymbol{B}\cdot\nabla p = 0 \qquad \text{and} \qquad \boldsymbol{J}\cdot\nabla p = 0$$

The first relation implies that the pressure is constant along magnetic field lines and therefore on the magnetic surfaces. The second relation implies that the pressure is constant along current density lines, and therefore such lines lie onto the magnetic surfaces. Since f is also constant along current density lines, we can conclude that ψ, f and p are all constant on the magnetic surfaces.

From these considerations the definition of *plasma boundary* can be extrapolated, as it is usually referred to be the Last Closed Flux Surface (LCFS). It represents ideally the limit flux surface within which is present a plasma current density. In a real environment, this statement is not true, since transport losses are present and the LCFS is continuously crossed by plasma particles.

According to this definition, it is possible to show that there are two possibilities:

- the plasma boundary touches the wall of the vacuum chamber (limiter plasma) (Fig. 2.3a)
- the plasma boundary does not touch the wall of the vacuum chamber (diverted or x-point plasma) (Fig. 2.3b)

In the latter case, the poloidal flux function has a saddle on the plasma boundary; near this point, the field line is "x" shaped, and therefore this point is called the x-point (or null point, since the magnetic field is zero). This solution is found imposing to the GSE the condition of $\nabla\psi = 0$ in the x-point. Diverted configuration is usually preferable to the limiter one because allows to exploit more available volume in the vacuum chamber (reducing the investments costs) and reduces drastically the plasma-wall interaction.

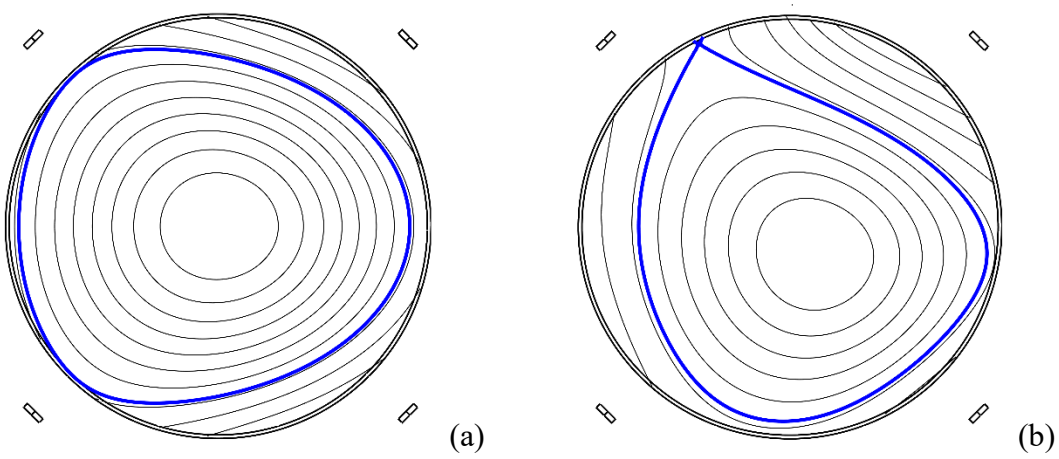

Fig 2.3: (a) Limiter plasma, (b) Diverted plasma

2.2 FRIDA Code – a tool for the numerical solution of the GSE

The solution of the GSE (2.20) presents various challenges, it depends on non-linear parameters and plasma boundary, i.e. the plasma domain, is not known a priori. For this reason, the problem can be addressed as *free-boundary problem*. In order to obtain a solution of practical interest, an iterative numeric solution is preferable to an analytical one. The basic principle of the numeric solution of the GSE relies on providing a tentative solution $\psi_0(r,z)$, so computing backwards the $p_i(\psi)$ and $f_i(\psi)$ parameters and thus finding a new solution $\psi(r,z)$. The procedure is so iterated to convergence. For this work, the newly developed FRIDA (Free-boundary Integro-Differential Axisymmetric) code has been used [14].

The magnetostatic equilibrium problem can be written as:

$$\begin{aligned} L(\psi) &= -\mu_0 J_\phi(\vec{\boldsymbol{r}}) \\ \psi(\vec{\boldsymbol{r}})|_{[r=0]} &= 0 \\ \lim_{\|\boldsymbol{r}\|\to\infty} \psi(\vec{\boldsymbol{r}}) &= 0 \end{aligned} \tag{2.21}$$

Where $L(\psi) = \nabla \cdot \left(\frac{1}{r}\nabla\psi\right) = \Delta^*$, $\vec{\boldsymbol{r}} = (r,z)$ and $\psi(\vec{\boldsymbol{r}})$ is the poloidal flux per radian defined as

$$\psi(\boldsymbol{r}) = \frac{1}{2\pi}\int_{S_\phi(\boldsymbol{r})} (\nabla \times \boldsymbol{A}) \cdot \boldsymbol{n}\, dS,$$

where $\boldsymbol{A}$ is the magnetic vector potential and $S_\phi(\vec{\boldsymbol{r}})$ is the circular surface centred on the z axis ad obtained by rotating a certain point $\vec{\boldsymbol{r}}$ around the z axis.

The domains of the problem are:

- vacuum internal region Ω_v, the vacuum region available to the plasma (vacuum chamber)
- vacuum external region Ω_v^*, a narrow region which encircles Ω_v and not available to the plasma (due to computational reasons)
- plasma domain Ω_p
- coils region $\Omega_c = \cup_{i=1}^{N_c} \Omega_{Ci}$, the region of the N_c active coils
- $\partial\Omega$ is the boundary of the computational domain

The source term $J_\phi(\boldsymbol{r})$ assumes different definitions depending on the region:

$$J_{\phi(\boldsymbol{r})} = \begin{cases} J_p(\vec{\boldsymbol{r}},\psi) = \lambda\left[r\dfrac{dp(\overline{\psi})}{d\overline{\psi}} + \dfrac{f(\overline{\psi})}{\mu_0 r}\dfrac{df(\overline{\psi})}{d\overline{\psi}}\right] & \text{In } \Omega_p \\ J_{Ci} & \text{In } \Omega_{c_i} \\ 0 & \text{elsewhere} \end{cases} \tag{2.22}$$

where the profiles $p(\overline{\psi})$, $f(\overline{\psi})$ are given in terms of normalized poloidal flux $\left(\overline{\psi} = \frac{\psi - \psi_a}{\psi_b - \psi_a}\right)$, where ψ_a and ψ_b are the fluxes at magnetic axis and plasma boundary respectively.

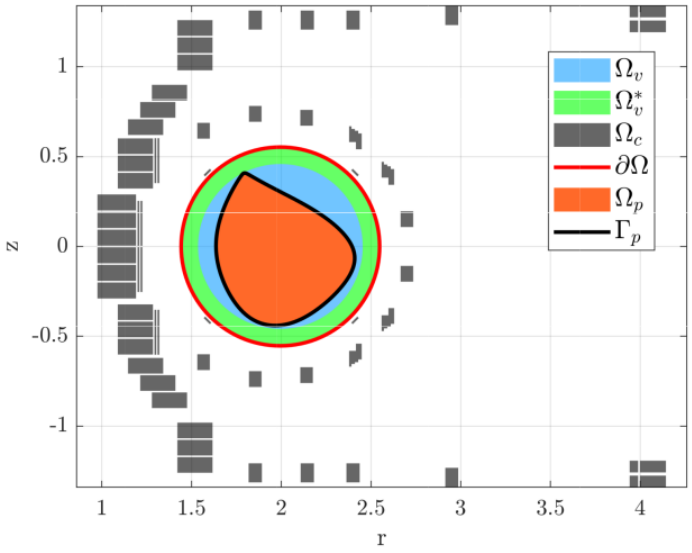

Fig 2.4: FRIDA Computation domains $\Omega_v, \Omega_v^*, \Omega_c$ and Ω_p

From a rigorous point of view, the computational domain is $[r, z] \in [0 \times \infty, -\infty \times \infty]$, but a limited-bounded domain is required to solve the problem numerically. For this reason a limited region of vacuum, which surrounds the plasma region without intersecting or overlapping the active conductors, is considered. An example of this configuration is shown in Fig. 2.4, where the limited computational domain $\Omega_d = \Omega_v \cup \Omega_v^*$ is highlighted. From a mathematical point of view, this means that the regularity conditions at infinity expressed by (2.21) can be replaced with:

$$\psi(\vec{r})|_{\partial\Omega} = \hat{\psi}$$

The BCs on $\partial\Omega$ impose to find a suitable coupling method with the FEM block, hence, the total flux at the boundary can be split into:

$$\hat{\psi}(\vec{r}, \psi) = \hat{\psi}_p(\vec{r}, \psi) + \hat{\psi}_c(\vec{r}) \tag{2.23}$$

where $\hat{\psi}_p$, $\hat{\psi}_c$ are the contributions of the plasma and the external coils, respectively. The total flux at the boundary depends both on the known total value I_p and on the current density distribution, which is a non-linear function of ψ: for this reason $\hat{\psi}(\vec{r}, \psi)$ is also non-linear and depends on ψ. The contribution of the external coils, instead, is fixed and depends only on the geometry and the current in the external coils.

The typical way to reduce the computation on the unbounded domain to a limited-bounded domain relies on the analytical Green's function [15].

Equation (2.23) is treated recalling the fundamental solution of eq. (2.21), also known as Green function of $L(\psi)$, giving the integral formulation of the Boundary Element problem:

$$\hat{\psi}_p(\vec{\boldsymbol{r}}, \psi) = \int_{\Omega_p} G(\vec{\boldsymbol{r}}_{\boldsymbol{b}}, \vec{\boldsymbol{r}}) J_p(\vec{\boldsymbol{r}}, \psi) d\Omega \tag{2.24}$$

$$\hat{\psi}_c(\vec{\boldsymbol{r}}) = \sum_{i=1}^{N_c} \int_{\Omega_p} G(\vec{\boldsymbol{r}}_{\boldsymbol{b}}, \vec{\boldsymbol{r}}) J_{Ci} d\Omega \tag{2.25}$$

Where $\vec{\boldsymbol{r}}_{\boldsymbol{b}} \in \partial\Omega$, Ω_{Ci} is the i−th active coil, N_c is the total number of active coils and $G(\vec{\boldsymbol{r}}, \vec{\boldsymbol{r}}')$ is the Green's function:

$$G(\vec{\boldsymbol{r}}, \vec{\boldsymbol{r}}') = \frac{\mu_0 \sqrt{rr'}}{2\pi k(\vec{\boldsymbol{r}}, \vec{\boldsymbol{r}}')} \left[\left(2 - k^2(\vec{\boldsymbol{r}}, \vec{\boldsymbol{r}}')\right) K\left(k(\vec{\boldsymbol{r}}, \vec{\boldsymbol{r}}')\right) - 2E\left(k(\vec{\boldsymbol{r}}, \vec{\boldsymbol{r}}')\right) \right] \tag{2.26}$$

with

$$k^2(\vec{\boldsymbol{r}}, \vec{\boldsymbol{r}}') = \frac{4rr'}{(r + r')^2 + (z - z')^2} \tag{2.27}$$

And $K(k)$, $E(k)$ are the complete elliptic integrals of the first and second kind, respectively:

$$K(k) = \int_0^{\pi/2} \frac{1}{\sqrt{1 - k^2 \sin^2 \theta}} d\theta \tag{2.28}$$

$$E(k) = \int_0^{\pi/2} \sqrt{1 - k^2 \sin^2 \theta}\, d\theta \tag{2.29}$$

Recalling the domain subdivisions presented above, the additional region Ω_v^*, forbidden to the plasma, is intended to avoid singularities on integral (2.24 - $\hat{\psi}_p(\vec{\boldsymbol{r}}, \psi)$). By doing this, the mesh nodes of the FEM formulation of Ω_p, which are the sources of (2.24), and the boundary nodes never coincide.

FEM approach is so treated with a Quadratic Lagrangian Element method, by means of the GMSH code [16], a versatile tool for domains discretization. The basis function used in this context is

$$w(\vec{\boldsymbol{r}}) = a_1 r^2 + a_2 z^2 + a_3 rz + a_4 r + a_5 z + a_6 \tag{2.30}$$

Considering the whole mesh nodes, and, for each node, the triangles sharing the same node (local support); $\psi(w(\vec{\boldsymbol{r}}), \vec{\boldsymbol{r}})$ and $J_p(w(\vec{\boldsymbol{r}}), \vec{\boldsymbol{r}}, \overline{\psi})$ can be computed.

$$\psi(\vec{\boldsymbol{r}}) = \sum_{\boldsymbol{i=1}}^{\boldsymbol{N_n}} \left(\sum_{\boldsymbol{j=1}}^{\boldsymbol{N_e^i}} w_j^{\boldsymbol{i}}(\vec{\boldsymbol{r}}) \right) \psi_i$$

$$J_p(\vec{\boldsymbol{r}},\overline{\psi}) = \sum_{\boldsymbol{i=1}}^{\boldsymbol{N_n}} \left(\sum_{\boldsymbol{j=1}}^{\boldsymbol{N_e^i}} w_j^i(\vec{\boldsymbol{r}}) \right) J_p(\overline{\psi}_i)$$

Where N_n is the number of mesh nodes and for each i-th node N_e nodes forming the local support are present.

The current density can be obtained from the profiles of the pressure and the poloidal current function f, or through a suitable parametrization. In the following, we will set:

$$J_\phi(\vec{\boldsymbol{r}},\psi) = \lambda g(\psi,\psi_a,\psi_b) \tag{2.31}$$

where the current density function $g(\psi,\psi_a,\psi_b)$ can be defined as:

$$g(\psi,\psi_a,\psi_b) = r\frac{dp(\overline{\psi})}{d\overline{\psi}} + \frac{f(\overline{\psi})}{\mu_0 r}\frac{df(\overline{\psi})}{d\overline{\psi}} \tag{2.32}$$

or

$$g(\psi,\psi_a,\psi_b) = \left[\frac{r\beta_0}{R_0} + \frac{(1-\beta_0)R_0}{r}\right]\left(1-\overline{\psi}^{\alpha_M}\right)^{\alpha_N} \tag{2.33}$$

depending on the available informations, knowing that, in eq. (2.33), R_0 is the machine major radius and the parameters α_M, α_N and β_0 have to be chosen properly to match the values of plasma internal inductance l_i and poloidal β_θ.

At this point the final system of equation can be obtained, as The GSE could be written in weak form by means of a weighted residual approach

$$\begin{aligned}\int_{\Omega_d} \frac{1}{r}\nabla w(\vec{\boldsymbol{r}})\cdot\nabla\psi(\vec{\boldsymbol{r}})d\Omega - \int_{\partial\Omega}\frac{1}{r}w(\vec{\boldsymbol{r}})\cdot\frac{\partial\hat{\psi}(\vec{\boldsymbol{r}})}{\partial\boldsymbol{n}}dS \\ = \int_{\Omega_d}\mu_0 w(\vec{\boldsymbol{r}})J_\phi(\vec{\boldsymbol{r}})d\Omega\end{aligned} \tag{2.34}$$

where $w(\vec{\boldsymbol{r}})$ is a scalar test function. Then considering $\hat{\psi}$ as defined in eq. (2.23), substituting the source term with (2.31) and knowing ψ_a and ψ_b, the imposition of the total plasma current leads to:

$$\begin{aligned}\int_{\Omega_d}\frac{1}{r}\nabla w(\vec{\boldsymbol{r}})\cdot\nabla\psi(\vec{\boldsymbol{r}})d\Omega + \int_{\Omega_d}\frac{1}{r}\nabla w(\vec{\boldsymbol{r}})\cdot\nabla\hat{\psi}(\vec{\boldsymbol{r}})d\Omega \\ = \lambda\int_{\Omega_d}\mu_0 w(\vec{\boldsymbol{r}})g(\psi,\psi_a,\psi_b)d\Omega\end{aligned} \tag{2.35}$$

$$\hat{\psi}_c(\vec{\boldsymbol{r}}) + \lambda\int_{\Omega_p} G(\vec{\boldsymbol{r}},\vec{\boldsymbol{r}}_{\boldsymbol{p}})w(\vec{\boldsymbol{r}})\,g(\psi,\psi_a,\psi_b)d\Omega = \hat{\psi}(\vec{\boldsymbol{r}}) \tag{2.36}$$

$$\max_{\Omega_p}\{\psi\} = \psi_a \tag{2.37}$$

$$\max_{\partial\Omega_v^- \cup \Omega_{v0}} \{\psi\} = \psi_b \tag{2.38}$$

$$\lambda \int_{\Omega_p} w(\boldsymbol{r})\, g(\psi, \psi_a, \psi_b) d\Omega = I_p \tag{2.39}$$

where $\partial\Omega_v^-$ is the portion of $\partial\Omega_v$ where $\vec{n} \cdot \nabla\psi < 0$, with $\vec{n}$ unit vector outgoing from $\partial\Omega_v$ and Ω_{v0} is the region inside Ω_v where the poloidal magnetic field vanishes.

The discrete version of the system (2.35-39) can be written in matrix form by defining a vector of unknowns $x = \left[\boldsymbol{\psi}, \widehat{\boldsymbol{\psi}}, \psi_a, \psi_b, \lambda\right]^T$:

$$\begin{bmatrix} \boldsymbol{K} & \boldsymbol{K_{bc}} & 0 & 0 & -\mu_0 \boldsymbol{i}(x) \\ 0 & \boldsymbol{E} & 0 & 0 & -G_{bp} \boldsymbol{i}(x) \\ \chi_a(x) & 0 & -1 & 0 & 0 \\ \chi_b(x) & 0 & 0 & -1 & 0 \\ 0 & 0 & 0 & 0 & I_t(x) \end{bmatrix} \begin{bmatrix} \boldsymbol{\psi} \\ \widehat{\boldsymbol{\psi}} \\ \psi_a \\ \psi_b \\ \lambda \end{bmatrix} = \begin{bmatrix} 0 \\ \widehat{\boldsymbol{\psi}}_{\boldsymbol{c}} \\ 0 \\ 0 \\ I_p \end{bmatrix} \tag{2.40}$$

where $\boldsymbol{\psi}$, $\widehat{\boldsymbol{\psi}}$ are the discrete counterparts of ψ, $\hat{\psi}$ and $\boldsymbol{E}$ is the identity matrix. The matrix blocks $\boldsymbol{K}(i,j)$ and $\boldsymbol{K_{bc}}(i,j)$ are defined as:

$$\boldsymbol{K}(i,j) = \int_{\Omega_{ij}} \frac{1}{r} \nabla w_i \nabla w_j d\Omega, \qquad i,j \in N_d \tag{2.41}$$

$$\boldsymbol{K_{bc}}(i,j) = \int_{\Omega_{ij}} \frac{1}{r} \nabla w_i \nabla w_j d\Omega, \qquad i \in N_d\ , j \in N_b \tag{2.42}$$

where $\Omega_{ij} = \Omega_e^i \cap \Omega_e^j$.

The term $i(x)$ is the vector of discrete currents, whose elements $Ii(x), i = 1, \ldots, N_n$ are obtained by integrating the source function $g\left(\overline{\psi}_i, \psi_a, \psi_b\right)$ on the mesh elements:

$$I_i(x) = I_i(\boldsymbol{\psi}, \psi_a, \psi_b) = \int_{\Omega_e^i} \left(\sum_{j=1}^{N_e^i} w_j^i(\vec{\boldsymbol{r}}) \right) g\left(\overline{\psi}_i, \psi_a, \psi_b\right) d\Omega \tag{2.43}$$

while I_t is the total current:

$$I_t(x) = \sum_{i=1}^{N_n} I_i(x)$$

Elements $\chi_a(x)$ and $\chi_b(x)$, are vectors of weights to identify the positions of the magnetic axis and the XP/limiter points respectively in terms of ψ. Since ψ is parameterized in terms of quadratic basis functions, the weight vector $\chi_a(x)$ is different from zero only on the triangle containing the magnetic axis, with weights equal to the values of each node's basis function on $\vec{\boldsymbol{r}}_a$. The same holds for ψb

and $\chi_b(x)$. To search for these points a proper algorithm is set to find where $\|\nabla\psi\| = 0$

Substituting the term $\lambda i(x)$ from the FEM block

$$\lambda i(x) = \frac{1}{\mu_0}(\boldsymbol{K}\psi + \boldsymbol{K_{bc}}\hat{\psi})$$

Into the BEM block, we get

$$-\frac{1}{\mu_0}\underbrace{\boldsymbol{G_{bp}}\boldsymbol{K}\boldsymbol{\psi} + \left(\boldsymbol{E} - \frac{1}{\mu_0}\boldsymbol{G_{bp}}\boldsymbol{K_{bc}}\right)}_{\widehat{\boldsymbol{K}}}\underbrace{\widehat{\boldsymbol{\psi}} - \widehat{\boldsymbol{\psi}}_c}_{\widehat{\boldsymbol{K}}_{\boldsymbol{bc}}}$$

Thus, the system (2.43) becomes:

$$\begin{bmatrix} \boldsymbol{K} & \boldsymbol{K_{bc}} & 0 & 0 & -\mu_0\boldsymbol{i}(x) \\ \widehat{\boldsymbol{K}} & \widehat{\boldsymbol{K}}_{\boldsymbol{bc}} & 0 & 0 & 0 \\ \chi_a(x) & 0 & -1 & 0 & 0 \\ \chi_b(x) & 0 & 0 & -1 & 0 \\ 0 & 0 & 0 & 0 & I_t(x) \end{bmatrix} \begin{bmatrix} \boldsymbol{\psi} \\ \widehat{\boldsymbol{\psi}} \\ \psi_a \\ \psi_b \\ \lambda \end{bmatrix} = \begin{bmatrix} 0 \\ \widehat{\boldsymbol{\psi}}_{\boldsymbol{c}} \\ 0 \\ 0 \\ I_p \end{bmatrix} \tag{2.44}$$

Furthermore, it can be written in a more compact form as:

$$\boldsymbol{A}(x)\boldsymbol{x} = \boldsymbol{b} \tag{2.45}$$

being $\boldsymbol{A}(x)$ the coefficients matrix of (2.44), $\boldsymbol{x}$ the vector of unknowns and $\boldsymbol{b}$ the vector of known terms.

The problem is non-linear because the source term $I_t(x)$ in Ω_p is a non-linear function of the solution $\boldsymbol{x}$, and because the plasma domain, delimited by the plasma boundary, is not known a priori

The article [14] proposes three methods to solve the system, but in this case only Newton-Raphson (NR) scheme is used to find the zero of

$$\boldsymbol{F}(x) = \boldsymbol{A}(x)\boldsymbol{x} - \boldsymbol{b} = 0 \tag{2.46}$$

NR scheme is more stable and reliable than the other methods proposed, like Picard and Newton-Krylov, if a suitable initial guess is given, and has, under certain assumptions, a quadratic convergence. Moreover, a relaxed (or damped) NR algorithm is used in order to guarantee better convergence (Fig. 2.5):

$$\begin{aligned} \boldsymbol{J_F}(\boldsymbol{x}_k)\boldsymbol{h}_{k+1} &= -\boldsymbol{F}(\boldsymbol{x}_k) \\ \boldsymbol{x}_{k+1} &= \boldsymbol{x}_k + \alpha_k\boldsymbol{h}_{k+1} \end{aligned} \tag{2.47}$$

where $\boldsymbol{J_F}$ is the jacobian matrix and the relaxation parameter α_k is suitably chosen at every iteration to avoid an overshoot of the solution, especially during the very first iterations when the change between two following steps is quite important.

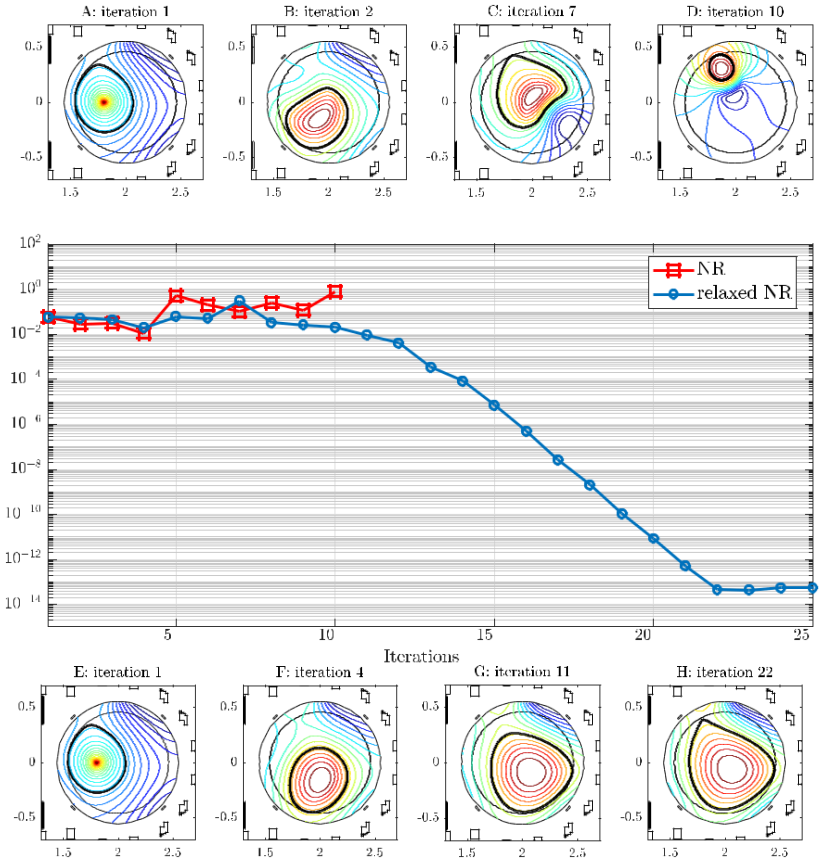

Fig 2.5: Impact on the relaxation parameter on the convergence: standard NR (top) and relaxed (bottom). In the middle results are presented

For this specific problem, $\boldsymbol{J_F}(x_k)$, defined as $\boldsymbol{J_F}(x_k) = \frac{\partial \boldsymbol{F}(x_k)}{\partial \boldsymbol{x_k}}$ can be written into two terms:

$$\boldsymbol{J_F}(x_k) = \boldsymbol{J'_F}(x_0) + \boldsymbol{J"_F}(x_k)$$

one dependent only on the geometry of the problem and the other instead changes at each iteration. This way the fixed part can be calculated once and then stored, saving time and lowering the computational cost of the method (Fig. 2.6).

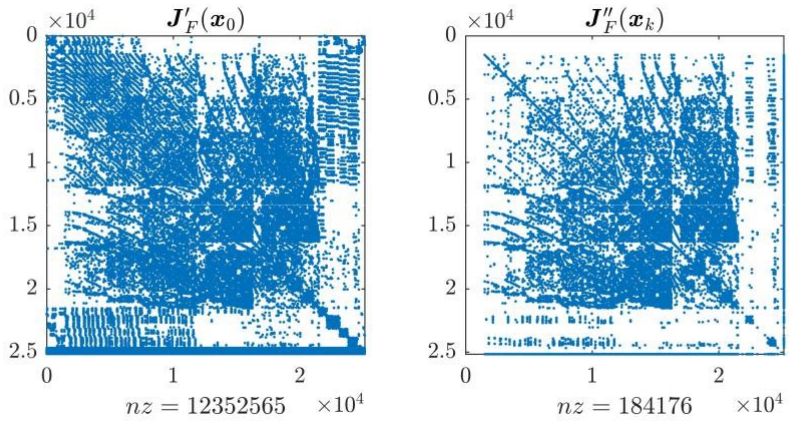

Fig. 2.6: Sparsity pattern of terms $\boldsymbol{J'_F}(x_0)$ and $\boldsymbol{J"_F}(x_k)$

SECTION 3

3 A method for plasma parameters reconstruction

In this section the goal is to derive a suitable model for plasma parameters reconstruction by means of the *moments of toroidal current density*. These are particularly useful because their values are related to key parameters of a plasma discharge, such as the total plasma current, position and shape aspects.

These informations are crucial for active control, meaning that a fast and flexible method to obtain them is mandatory. For this purpose, as it will be shown, moments evaluation could be performed directly from magnetic diagnostics measurements present in real devices, making possible the real-time evaluation of key plasma values.

Before deepening the moments computation, it is useful to report how magnetic field generated by an axisymmetric loop current can be computed, since it will be extensively used when calculating the moments of toroidal current density.

3.1 Poloidal field in a generic point of space

Considering a generic poloidal plane (r, z), poloidal field sources can be considered as toroidal axisymmetric current loops. This way they can be visualized as a point in the poloidal plane, and relations among them can be written referring to poloidal coordinates only. A generic circular coil with radius a enjoying of axial symmetry and crossed by the induction field $\vec{B}(r, \phi, z)$ in a generic point of space, has the following components:

$$B_r(r,0,z) = \frac{2\mu_0 I z}{2\pi r\sqrt{z^2+(a+r)^2}}\left[-K(k) + E(k)\frac{a^2+r^2+z^2}{(a-r)^2+z^2}\right] \tag{3.1}$$

$$B_\phi(r,0,z) \equiv 0$$

$$B_z(r,0,z) = \frac{2\mu_0 I}{2\pi\sqrt{z^2+(a+r)^2}}\left[K(k) + E(k)\frac{a^2-r^2-z^2}{(a-r)^2+z^2}\right] \tag{3.2}$$

Where $K(k)$ and $E(k)$ are the complete elliptic integrals of first and second kind defined in (2.28-29), and k is linked with problem's geometry:

$$k^2 = \frac{4ar}{(a-r)^2+z^2} \tag{3.3}$$

This representation of magnetic field is particularly useful, meaning that, for any toroidal current, magnetic field can be easily computed for any point in the

poloidal plane. Since magnetic probes used in this work (illustrated in Sections 4 and 6) are placed along a circumference measuring the magnetic field with respect to the tangential and normal components, a suitable parametrization has to be chosen to obtain desired projections from the (r, z) components.

Let:

$$(\zeta) = \big(\gamma_1(\zeta), \gamma_2(\zeta)\big) \tag{3.4}$$

With γ a closed curve in the poloidal plane (r, z), with $\zeta \subset [0,1]$ normalized curvilinear abscissa. This allows to calculate the $\vec{B}_\theta$ components with respect to the curve γ: B_t, B_n (tangent and normal components). Given such versors defined as:

$$\vec{\boldsymbol{t}} = \frac{1}{\|\gamma(\zeta)\|}\big(\gamma_1'(\zeta),\ \gamma_2'(\zeta)\big)\,, \quad \vec{\boldsymbol{n}} = \frac{1}{\|\gamma(\zeta)\|}\big(\gamma_2'(\zeta),\ -\gamma_1'(\zeta)\big) \tag{3.5}$$

We obtain

$$B_t(r,z) = \vec{B}_\theta \cdot \vec{\boldsymbol{t}} = \frac{1}{\|\gamma(\zeta)\|}\Big(B_r\big(\gamma(\zeta)\big)\gamma_1'(\zeta) + B_z\big(\gamma(\zeta)\big)\gamma_2'(\zeta)\Big)$$

$$B_n(r,z) = \vec{B}_\theta \cdot \vec{\boldsymbol{n}} = \frac{1}{\|\gamma(\zeta)\|}\Big(B_r\big(\gamma(\zeta)\big)\gamma_2'(\zeta) - B_z\big(\gamma(\zeta)\big)\gamma_1'(\zeta)\Big)$$

3.2 Moments of toroidal current density

Considering the plasma domain $\Omega_p \in (r, z)$, as defined for FRIDA in par. 2.2, let Ω_d be generic domain such that $\Omega_p \subseteq$ Ωd.

The n-th order moment of the plasma toroidal current density is defined as the following integral calculated over domain Ω_d [17]:

$$q_n = \int_{\Omega_d} \chi_n(r,z) J_\phi(r,z)\, dr dz \tag{3.6}$$

Weight function $\chi_n(r, z)$ it's a n-th order polynomial that's solution of the homogeneous GSE equation: $\Delta^* \chi_n(r, z) = 0$, which has the following expression:

$$\chi_n(r,z) = r^n \sum_{k=0}^{\left\lfloor \frac{n}{2} \right\rfloor - 1} (-4)^{-k} \frac{(n-2)!}{k!\,(k+1)!\,(n-2k-2)!} \left[\frac{z}{r}\right]^{n-2k-2} \tag{3.7}$$

where $\lfloor \# \rfloor$ is the function $floor(\#)$.

An extensive description on the method to obtain this formulation is given in [17]

The lower-order moments $n = 0, 1, 2$ allow to determine the fundamental quantities for the plasma, respectively the current I_p and the coordinates of the position of the plasma centroid (r_p, z_p). For polynomials of higher order, moments provide information on elongation of skew κ_{sk} and vertical κ_v, respectively, and upper triangularity δ_{up} and lower δ_{down}. Indeed, featuring (3.7) for orders n = 0, ..., 6 we obtain:

$$\chi_0 = 1 \quad \Longrightarrow \quad q_0 = \int_{\Omega_d} \chi_0(r,z) j_\phi(r,z) dr dz = I_p$$

$$\chi_1 = z \quad \Longrightarrow \quad q_0 = \int_{\Omega_d} \chi_1(r,z) J_\phi(r,z) dr dz = z_p I_p$$

$$\chi_2 = r^2 \quad \Longrightarrow \quad q_0 = \int_{\Omega_d} \chi_1(r,z) J_\phi(r,z) dr dz = r_p^2 I_p$$

$$\chi_3 = r^2 z \quad \Longrightarrow \quad q_0 = \int_{\Omega_d} \chi_3(r,z) J_\phi(r,z) dr dz = \kappa_{sk}^3 I_p$$

$$\chi_4 = r^2 z^2 - \frac{1}{4} r^4 \quad \Longrightarrow \quad q_0 = \int_{\Omega_d} \chi_4(r,z) J_\phi(r,z) dr dz = \kappa_v^4 I_p$$

$$\chi_5 = r^2 z^3 - \frac{3}{4} r^4 z \quad \Longrightarrow \quad q_0 = \int_{\Omega_d} \chi_5(r,z) J_\phi(r,z) dr dz = \delta_{up}^5 I_p$$

$$\chi_6 = r^2 z^4 - \frac{3}{2} r^4 z^2 + \frac{1}{8} r^6 \quad \Longrightarrow \quad q_0 = \int_{\Omega_d} \chi_6(r,z) J_\phi(r,z) dr dz = \delta_{down}^6 I_p$$

In this work, we will focus just on the first three moments with $n = 0, 1, 2$. The zeroth order moment gives directly the total plasma current, while the centroid can be extracted with the following integral and discrete relations:

$$r_p = \sqrt{\frac{\int_{\Omega_d} r^2 J_\phi(r,z) dr dz}{\int_{\Omega_d} J_\phi(r,z) dr dz}} \longrightarrow \sqrt{\frac{\sum_{k=1}^{n_p} i_{p0,k} r_k^2}{\sum_{k=1}^{n_p} i_{p0,k}}}$$

$$z_p = \frac{\int_{\Omega_d} z J_\phi(r,z) dr dz}{\int_{\Omega_d} J_\phi(r,z) dr dz} \longrightarrow \frac{\sum_{k=1}^{n_p} i_{p0,k} z_k}{\sum_{k=1}^{n_p} i_{p0,k}}$$

However, in a real environment, the input term of the moment computation should be the poloidal magnetic field, since this is the data one could dispose from magnetic measurements. For this reason, it is useful to express the (3.6) in function of the desired B-field components. Consider a positively oriented closed curve $\gamma(\zeta)$ – as defined in (3.4) – such that $\gamma(\zeta) = \partial\Omega_d$ and $\gamma(\zeta) \in C^1$

$$\int_{\Omega_d} \frac{1}{\mu_0 r}(\psi\Delta^*\chi_n - \chi_n\Delta^*\psi)drdz = \int_{\Omega_d} -\frac{1}{\mu_0 r}(\chi_n\Delta^*\psi)drdz$$

$$= \int_{\Omega_d} \chi_n(r,z)J_\phi(r,z)drdz = q_n$$

Exploiting the second Green's identity it is possible to go from the integral over Ω_d to a surface integral through the curve $\gamma(\zeta) = \partial\Omega_d$. So we'll obtain

$$q_n = \int_{\Omega_d} \frac{1}{\mu_0 r}(\psi\Delta^*\chi_n - \chi_n\Delta^*\psi)drdz$$

$$= \int_{\partial\Omega_d} \frac{1}{\mu_0 r}(\psi\nabla\chi_n - \chi_n\nabla\psi)\cdot\vec{\boldsymbol{n}}\, d\gamma$$

$$= \int_{\partial\Omega_d} \frac{1}{\mu_0 r}\left(\psi\frac{\partial\chi_n}{\partial\vec{\mathbf{n}}} - \chi_n\frac{\partial\psi}{\partial\vec{\mathbf{n}}}\right)d\gamma \tag{3.8}$$

At this point the function $\xi_n(r,z): \mathbb{R}^2 \to \mathbb{R}$, conjugated of the $\chi_n(r,z)$ function, is introduced, such as:

$$\frac{\partial}{\partial r}\left(\frac{\xi_n}{\mu_0 r}\right) = -\frac{1}{\mu_0 r}\frac{\partial\chi_n}{\partial z} \tag{3.9}$$

$$\frac{\partial}{\partial z}\left(\frac{\xi_n}{\mu_0 r}\right) = \frac{1}{\mu_0 r}\frac{\partial\chi_n}{\partial r} \tag{3.10}$$

That implies the following result:

$$\nabla\left(\frac{\xi_n}{\mu_0 r}\right) \perp \frac{1}{\mu_0 r}\nabla\chi_n \tag{3.11}$$

and as the unit vectors are defined:

$$\int_\gamma \frac{1}{\mu_0 r}\nabla\chi_n\vec{\boldsymbol{n}}\, d\gamma = \oint_\gamma \nabla\left(\frac{\xi_n}{\mu_0 r}\right)\vec{\boldsymbol{t}}\, d\gamma$$

Therefore, the integral (3.8) becomes:

$$q_n = \int_\gamma \psi\nabla\left(\frac{\xi_n}{\mu_0 r}\right)\vec{\boldsymbol{t}}\, d\gamma - \int_\gamma \frac{1}{\mu_0 r}\chi_n\nabla\psi\,\vec{\boldsymbol{n}}\, d\gamma$$

where integrals over γ indicates respectively a circuitaiton and a flux.

writing:

$$\nabla\left(\frac{\xi_n}{\mu_0 r}\right) = \psi\nabla\left(\frac{\xi_n}{\mu_0 r}\right) + \left(\frac{\xi_n}{\mu_0 r}\right)\nabla\psi \tag{3.12}$$

and accounting the fact that integration domain is simply connected, and that such vector field is conservative, the line integral along a close path of the first term of the (3.12) is always zero. Therefore, being the poloidal flux defined as (2.9) the term q_n becomes:

$$q_n = -\int_\gamma \left(\frac{\xi_n}{\mu_0 r}\right) \nabla\psi \vec{\boldsymbol{t}}\, d\gamma - \int_\gamma \frac{1}{\mu_0 r} \chi_n \nabla\psi\, \vec{\boldsymbol{n}}\, d\gamma$$

$$= -\int_0^1 \frac{\chi_n}{\mu_0} (\mathrm{B_z}\gamma_2' + B_r\gamma_1')\, d\zeta + \int_0^1 \frac{\xi_n}{\mu_0} (\mathrm{B_z}\gamma_1' + B_r\gamma_2')\, d\zeta$$

$$= -\frac{1}{\mu_0}\oint_\gamma \chi_n \vec{\mathrm{B}}_\theta \cdot \vec{\boldsymbol{t}}\, d\gamma - \frac{1}{\mu_0}\int_\gamma \xi_n \vec{\mathrm{B}}_\theta \cdot \vec{\boldsymbol{n}}\, d\gamma \tag{3.13}$$

The first integral is a line integral along the curve γ, and the second one a surface integral through the same closed curve.

The moment q_n has been defined involving a closed curve in anticlockwise direction. Moving clockwise, the relation becomes:

$$q_n = \frac{1}{\mu_0}\oint_\gamma \chi_n \vec{\mathrm{B}}_\theta \cdot \vec{\boldsymbol{t}}\, d\gamma + \frac{1}{\mu_0}\int_\gamma \xi_n \vec{\mathrm{B}}_\theta \cdot \vec{\boldsymbol{n}}\, d\gamma \tag{3.14}$$

A useful consideration on this last (3.16) equation can be focusing on the moment q_0. This leads to compute the weights $\chi_0 = 1$ and $\xi_0 = 0$ so the relation becomes

$$q_0 = \int_{\Omega_d} \chi_0(r,z) J_\phi(r,z) dr dz = I_p = \frac{1}{\mu_0}\oint_\gamma \vec{B}_\theta \cdot \vec{\boldsymbol{t}}\, d\gamma$$

That is exactly the integral formulation of the Ampere's Circuital Law. Hence the quantity q_n, through the relation (3.7), represents a generalization of the idea of search for information about a current by evaluating the components B_t, B_n of the induction field generated by it along a curve γ which concatenates it. In particular, is clear how Ampere's law is a particular case of moment calculation for the degree $n = 0$. The term q_n can give gradually different information on the position and shape of the current of plasma according to the choice of different weights χ_n, ξ_n, and consequently different linear combinations of the terms B_t, B_n.

3.2.1 Computation of the moments of the current density for realistic applications

When a limited number of probes is considered, which commonly happens when realistic devices are considered, the computation of the moments of the current density cannot be performed by the definition (i.e. eq. (3.14)) because of the discrete line integral on such a low number of points. This would mean to assume

the value of B_{meas} constant along the path between two calculation points (the sensors). For this reason, an optimization method, as introduced in [17], is used to solve the problem of computing the moments of the current density for realistic cases.

The moment q_n is written as a linear combination of the induction field measurements. This implies that, known the resulting moments in a high number of reference cases, the weight coefficients for the linear combination of the measurements could be found solving an optimization problem. Ideally, if a suitably high number of reference configurations are considered, these optimal weights will be independent from the plasma current configuration.

Considering a generic moment q_n of a plasma configuration, relation (3.6) is written as follows:

$$k_{n_1} m_1 + k_{n_2} m_2 + \cdots + k_{n_{14}} m_{14} = I_p \tag{3.15}$$

With m_h $(h = 1, \dots N_s)$ induction field measured by the h-th sensor. Vector $\boldsymbol{k}_n$ contains N_s weights, one for each measure of the N_s sensors, which linear combination with the respective measurements, allows to reconstruct the moment.

In order to compute the coefficients, the following configuration is considered. A plasma cross-section composed of $N_p = N_{mesh}$ equivalent filamentary conductors is considered, giving N_p scenarios. Each scenario is so composed by the presence of one single filament that carries unitary current. Therefore, for every single loop, the moments of order 0, 1 and 2 are computed as:

$$q_{0,i} = I_{p,i} = 1$$

$$q_{1,i} = z_i I_{p,i} = z_i$$

$$q_{2,i} = r_i^2 I_{p,i} = r_i^2$$

with $i = 1, \dots, N_p$ and (r_i, z_i) the poloidal coordinates of each filament. Hence the relation (3.15) can be used to write the system for every scenario: In matrix form:

$$\boldsymbol{G}_{p,s} \boldsymbol{k}_{I_p} = \boldsymbol{1}$$

$$\boldsymbol{G}_{p,s} \boldsymbol{k}_{z_p} = \boldsymbol{z_p}$$

$$\boldsymbol{G}_{p,s} \boldsymbol{k}_{r_p} = \boldsymbol{r_p^2}$$

being $\boldsymbol{G}_{p,s} \in \mathbb{R}^{N_p \times N_s}$ the matrix giving, for each filament, the measurements on each sensor, with N_s number of sensors.

The result can't be computed exactly, being $N_p \neq N_s$: therefore, a least square solution is found writing the problems in the form

$$\begin{aligned} &\min_{\boldsymbol{K_{I_p}}} \left\| \boldsymbol{G}_{p,s}\boldsymbol{k}_{I_p} - \boldsymbol{b}_{I_p} \right\|_2 \\ &\min_{\boldsymbol{K_{z_p}}} \left\| \boldsymbol{G}_{p,s}\boldsymbol{k}_{z_p} - \boldsymbol{b}_{z_p} \right\|_2 \\ &\min_{\boldsymbol{K_{r_p}}} \left\| \boldsymbol{G}_{p,s}\boldsymbol{k}_{r_p} - \boldsymbol{b}_{r_p} \right\|_2 \end{aligned} \tag{3.16}$$

where $\boldsymbol{b}$ indicates the vector of the known terms and $\|\#\|_2$ is the Euclidean norm.

Since problem is ill-conditioned, a Truncated Singular Value Decomposition (TSVD) is required, through which some regularity of the solution can be gained. However, some data-fit might be lost in the process, and some fine-tuning on the truncation index parameter k_t has to be performed.

The SVD decomposition of the matrix $\boldsymbol{G}_{p,s}$ leads to

$$\boldsymbol{G}_{p,s} = \boldsymbol{U}\boldsymbol{S}\boldsymbol{V}^T \tag{3.17}$$

with $\boldsymbol{U} \in \mathbb{R}^{N_p \times N_p}$, $\boldsymbol{V} \in \mathbb{R}^{N_s \times N_s}$ and $\boldsymbol{S} \in \mathbb{R}^{N_p \times N_s}$ extension of the square matrix $\boldsymbol{S}^* = diag(\sigma_1, \dots, \sigma_{N_s})$ setting to zero all the terms of the matrix outside the diagonal of $\boldsymbol{S}^*$.

From eq. (3.17) is possible to obtain the solution vector for least squares problem:

$$\boldsymbol{k} = \boldsymbol{V}\boldsymbol{S}^{+}\boldsymbol{U}^T\boldsymbol{b} = \sum_{i=1}^{N_s} \frac{(\boldsymbol{U}^T\boldsymbol{b})(i)}{\sigma_i}\mathbf{v_i} \tag{3.18}$$

The SVD solution is not sufficiently regular because the sets of coefficients are too sensitive with respect to the position and the value of the currents. This happens because the problem is ill-conditioned, as already stated. To gain more regularity on the solution, the aforementioned truncation index k_t is introduced, so that the first k_t greater singular values are retained, and the remaining smaller ones are disregarded. Therefore, the solution becomes:

$$\boldsymbol{k} = \boldsymbol{V}_{k_t}\boldsymbol{S}_{k_t}^{+}\boldsymbol{U}_{k_t}^T\boldsymbol{b} = \sum_{i=1}^{N_s} \frac{(\boldsymbol{U}_{k_t}^T\boldsymbol{b})(i)}{\sigma_k}\mathbf{v_i} \tag{3.19}$$

where $\boldsymbol{U} \in \mathbb{R}^{N_p \times k_t}$, $\boldsymbol{V} \in \mathbb{R}^{N_s \times k_t}$ and $\boldsymbol{S} \in \mathbb{R}^{k_t \times k_t}$ diagonal matrix composed by $\text{diag}(\sigma_1, \dots, \sigma_{k_t})$.

From the experimental analysis it was seen that, for the RFX-mod2 set of sensors, a $k_t = 8$ is the best compromise between precision and regularity of the solution. In Sec. 6 the computation will be carried out with an even smaller number of sensors, hence the utilized rule for calculating the truncation index is $k_t = ceil(\frac{N_s}{2})$ ($+1$ if N_s even).

SECTION 4

4 The RFX-mod2 Experiment

4.1 Introduction

RFX-mod [18] was a toroidal device, with minor radius of $0.46m$ and major radius of $2m$, designed to operate as RFP with plasma current up to $2MA$. Similarly to a tokamak, the RFP carries a toroidal plasma current confined by an equilibrium magnetic field whose main components are toroidal and poloidal. Contrarily to a tokamak, the RFP confines the same plasma current with an average toroidal field which is ten times smaller than that in a tokamak (poloidal and toroidal magnetic fields are comparable in amplitude). Furthermore, the toroidal magnetic field produced by the external coils is extremely small compared to the one in a tokamak, of the order of some mT during the flat-top reversal phase in a typical MA RFP plasma discharge, since the field is mainly produced through a self-organization process by currents flowing in the plasma itself. Thanks to its flexibility, RFX-mod experiment has been operated both as an RFP and a tokamak. In fact, the toroidal field circuit can provide toroidal magnetic field far in excess of that needed for RFP operation. Therefore, ohmic tokamak operations were performed in the past involving circular plasma discharges with toroidal field up to $0.55\ T$ and plasma current up to $100\ kA$. The same engineering flexibility on the other magnet system, the field shaping circuit, allowed to perform shaped tokamak operations with different shapes of plasma poloidal cross sections and current up to $60\ kA$.

One of the key parameters for the stability of RFP plasma operations is the distance between the passive stabilizing conductor, consisting of a copper shell $3\ mm$ thick, and the plasma. Based on the wide evidences of the experimental activity of RFX-mod, an upgrade of the experiment, dubbed RFX-mod2 [19] is presently in its manufacturing phase. It consists in the removal of the highly resistive Inconel vacuum vessel (VV) in order to bring the highly conductive passive stabilizing shell (PSS) as close as possible to the plasma. In particular, the shell/plasma radius ratio will reduce from $b/a = 1.11$ to $b/a = 1.04$, thus widening the chamber minor radius to $0.49m$, and the stainless-steel support structure will be made vacuum-tight (Fig 4.1a). A detailed description of the conducting structures of RFX-mod2 is reported in the next paragraph where comparisons with respect to RFX-mod are also provided.

4.1.1 Passive conductors

The RFX-mod PSS was a copper toroidal structure, 3 mm thick, surrounding the VV and providing MHD stabilization of RFP plasma in short time scale. This

conductive shell was provided with an electrical discontinuity in both toroidal and poloidal direction.

In RFX-mod2, due to the removal of the vessel, the PSS will be deeply modified [20] in order to sustain the new first wall and considering that a wide system of in-vessel diagnostics have to operate in vacuum conditions.

Concerning the vacuum toroidal support structure (VTSS), this is being manufactured starting from the already existing RFX-mod stainless steel toroidal structure, which presents, as the PSS, two poloidal and two toroidal insulated gaps [20] [21]. The gaps have to be insulated since the new structure has also the function of maintaining the vacuum condition.

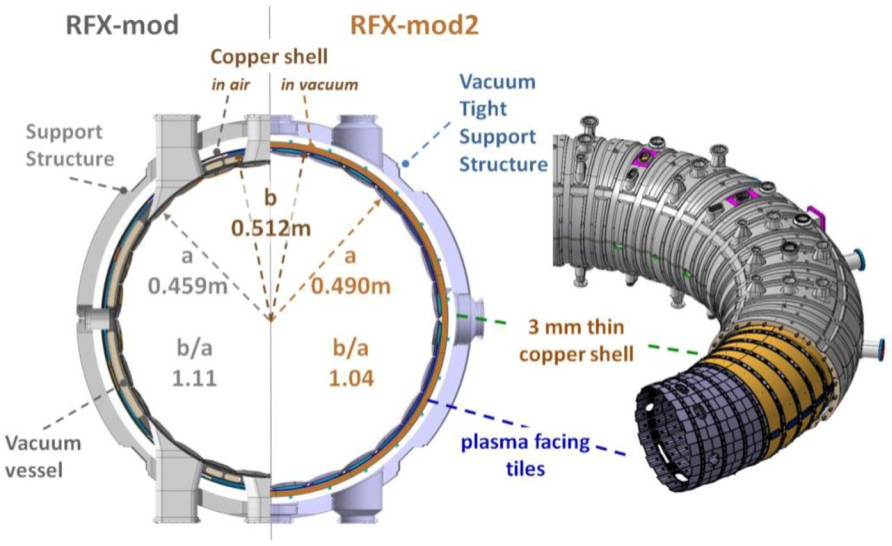

Fig: 4.1: (a) RFX-mod2 cross-section highlighting new structural radiuses, (b) isometric view [20]

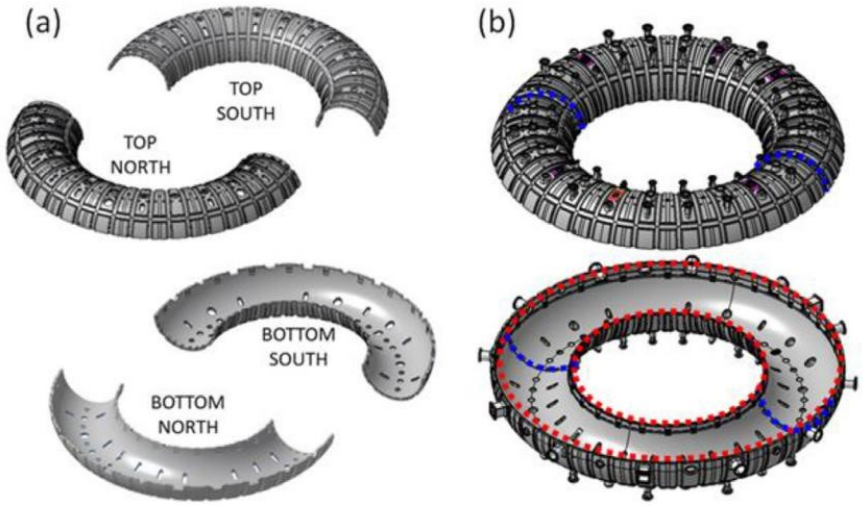

Fig 4.2: VTSS – mechanical support and vacuum vessel, (a) four parts exploded, (b) top/bottom halves exploded [21]

4.2 RFX-mod2 tokamak magnet system

RFX-mod2 magnet system [22] has not been changed from the previous RFX-mod design and it is constituted by two set of windings: the Toroidal Field winding (TFW) and the Poloidal Field windings (PFW). The TFW system consists of 48 coils uniformly distributed along the toroidal direction dedicated to produce the toroidal magnetic field necessary for tokamak operations, up to a maximum magnetic field of 0.7 T. The PFW is constituted by two set of coils: the Field Shaping winding (FSW), devoted to provide the equilibrium field, and the Magnetizing winding (MW), inducing the loop voltage necessary to sustain the plasma current.

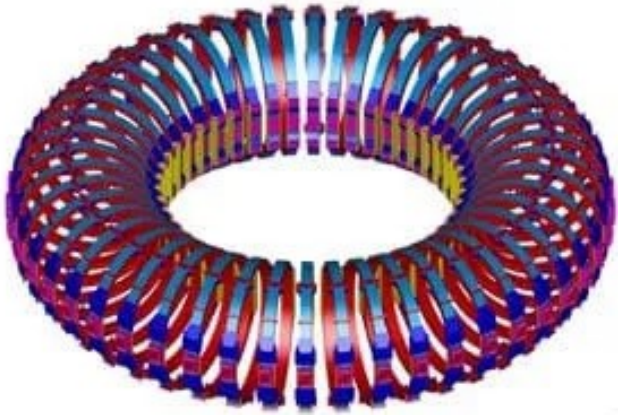

Fig 4.3 Toroidal Field coils

Fig 4.4: (a) Magnetizing / Ohmic heating coils, (b) Field Shaping coils

Moreover, a set of Saddle coils (SC), distributed along torus surface, are meant to provide a radial field component for stabilization purposes.

In the following we will focus solely on Tokamak operations, providing a brief description of the magnet system requirements for both limiter and diverted plasma discharges.

4.2.1 Poloidal field circuit

The poloidal field circuit is constituted by the previously introduced set of windings, the FSW and MW, properly connected for different plasma scenario

operations. The standard RFP and circular tokamak operation circuit is represented in Fig. 4.5.

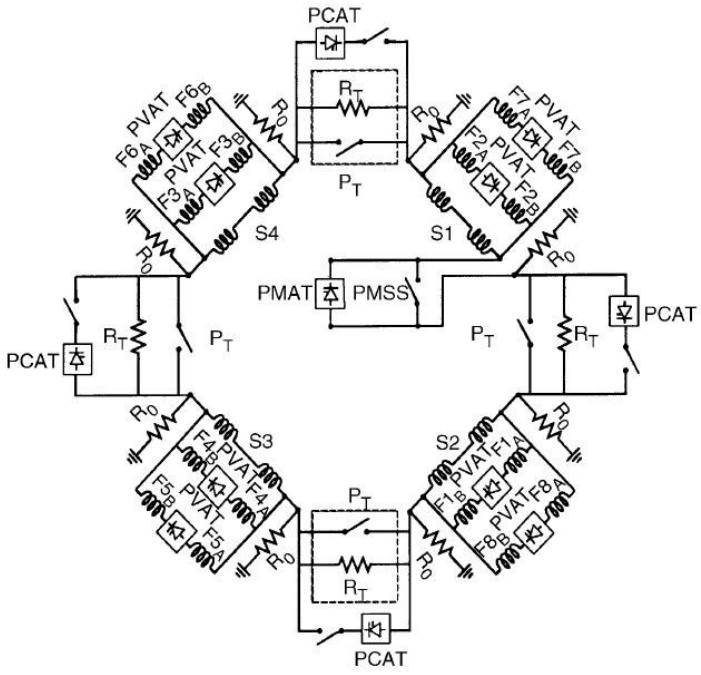

Fig. 4.5: RFX-mod2 poloidal field circuit

In RFX-mod2 the MW constitute four sectors each connecting different magnets as described by Tab. 4.1 (numeration of MW can be seen in Fig. 4.6).

S Sector	MW in series				
1	1	5	9	13	17
2	2	6	10	14	18
3	3	7	11	15	19
4	4	8	11	16	20

Tab. 4.1: RFX-mod2 PFW circuit sectors with MW coils interconnections

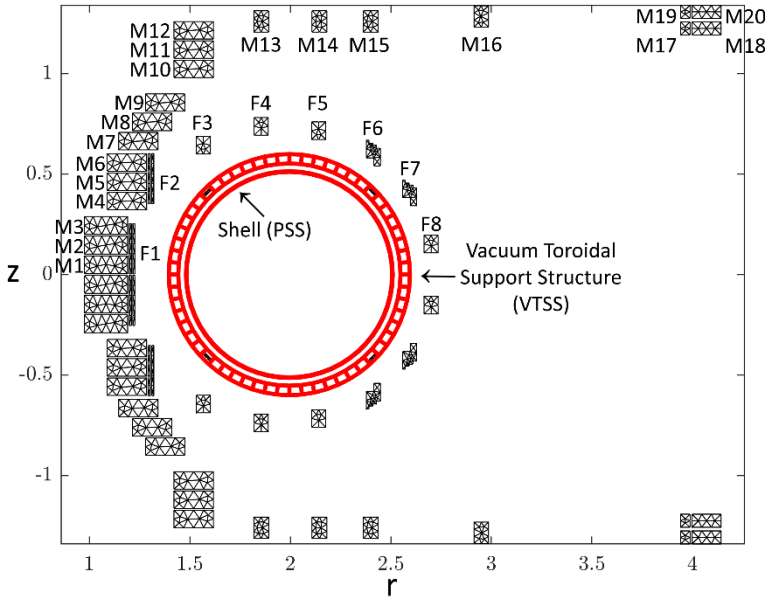

Fig. 4.6: RFX-mod2 poloidal section: coils and passive conductive structures

During the operations, a flux swing is generated by decreasing the current in the MW inducing the necessary loop voltage, to initiate and drive the plasma discharge.

FSW [23] are formed by eight couples of coils which are top/down symmetric and each one is connected in series with the correspondent symmetrical with respect to the equatorial plane (Fig. 4.6.). Each coil presents 24 turns, so that electromagnetic L and M parameters guarantee a build-in balance of the voltage induced in the FSW and in the MW sectors (parallel connected Fig. 4.5).

Single null operations require to break the equatorial plane symmetry and to reverse few currents in order to obtain both lower single null (LSN) or upper single null (USN) configurations with either positive or negative triangularity [24].

Plasma density (particles)	up to $8 \cdot 10^{18}$ m^{-3}
Max plasma temperature	20 M°C
Max. toroidal field	0.7 T
Max. plasma current	200 kA
Current rise time	200 ms
Flat-top time	~1 s
Discharge time	~1,2 s

Tab 4.2: RFX-mod2 tokamak specifications

4.2.2 Saddle coils

RFX-mod2 is equipped with a system of 192 Saddle Coils (SC) for active MHD control (Fig. 4.7) for both RFP and circular tokamak operations. They are arranged in 48 toroidal positions within each one 4 coils are located. These last ones are disposed with top/bottom and left/right symmetry guaranteeing a production of a radial magnetic field up to 50 mT DC and 3.5 mT at 100 Hz. In shaped tokamak discharges, the inner-outer SC are operated in order to provide the horizontal component of the magnetic field needed for the vertical stabilization.

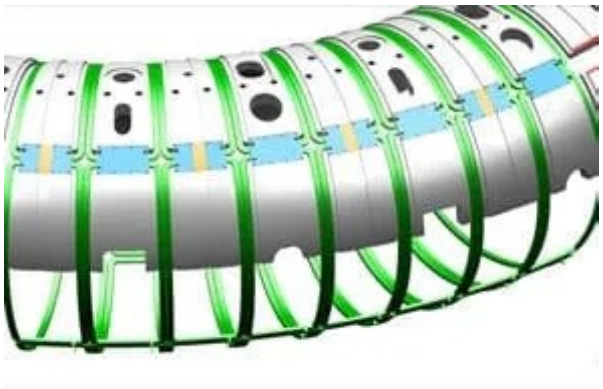

Fig 4.7: Saddle Coils

4.3 RFX-mod2 magnetic diagnostic system

The magnetic diagnostic system of RFX-mod2 is constituted by different magnetic sensors to fully characterize the plasma magnetic configuration.

Among the magnetic sensors, **Pick-up coils** are the main ones of interest for the purpose of this article. They are constituted by a wire loop which, being crossed by magnetic field, displays an induced loop voltage according to Faraday's law.

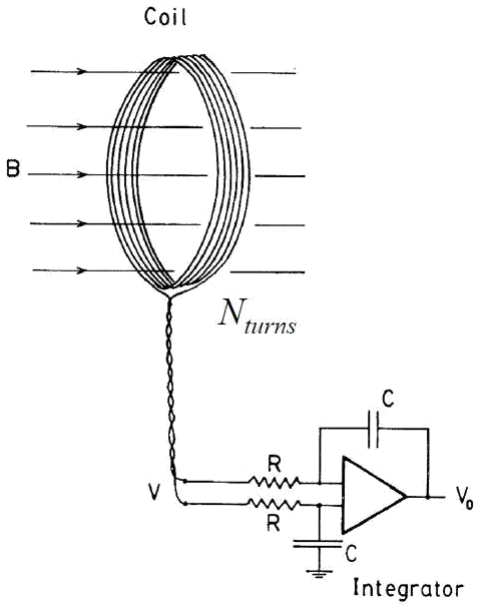

Fig 4.8: Pick-up coil circuit scheme

Considering the circuit shown in Fig. 4.8 and being S the loop surface and Γ its boundary, it stands:

$$\varepsilon(t) = \oint_{\Gamma} E \cdot \boldsymbol{t}\, dl$$

$$= -\int_{S} B \cdot \boldsymbol{n}\, dl$$

Exploiting this relation, the induced voltage in the loop is evaluated, and from that, the B-field is extrapolated. However non-ideality effects or capacitive couplings could lead to the circulation of a current in the loop, thus weakening the accuracy of the measurement.

Since the pick-up coil can evaluate the magnetic field normal to S, other two coils are implemented in the device, so that all the three spatial components of B could be measured.

For the purpose of this work, from the pick-up coils used in RFX-mod2, will be accounted the poloidal field components that corresponds to the tangential and normal field with respect to the sensor circumference detailed in Tab 4.3.

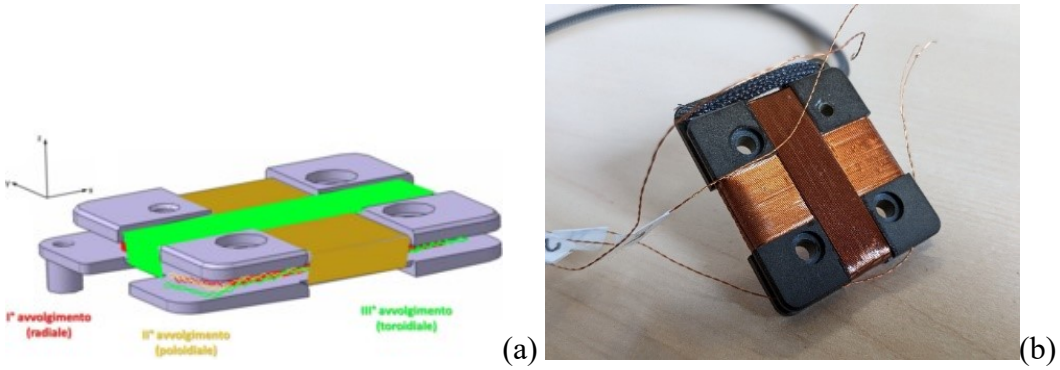

(a) (b)

Fig. 4.9: RFX-mod2 pick-up coil: (a) Sketch, (b) Physical sensor

The upgrade from RFX-mod to RFX-mod2 will bring some important improvements in the pre-existent set of magnetic sensors. In particular, the new set of pickup coils will be made up of 12 staggered poloidal arrays of 14 three-axial pickup coil sensors each.

Considering the machine centre being located at

$$r_{MC} = 1.995\ m$$

$$z_{MC} = 0\ m$$

RFX-mod2 pick-up coils are located on a circumference of:

$$r_{pickup} = 0.5085\ m$$

and

$$\theta_{pickup} = 6.43 + k \cdot 25.71, \qquad \text{with } k = 0, \dots, 13$$

$$\phi_{pickup} = 18 + l \cdot 30°, \qquad \text{with } l = 0, \dots, 11$$

Sensors are located in the inner part of the PSS, protected from the plasma by the graphite tiles of the first wall. Fig.10 shows the position of the pickup coils among the RFX-mod2 geometry, while Tab 4.3 provides their coordinates.

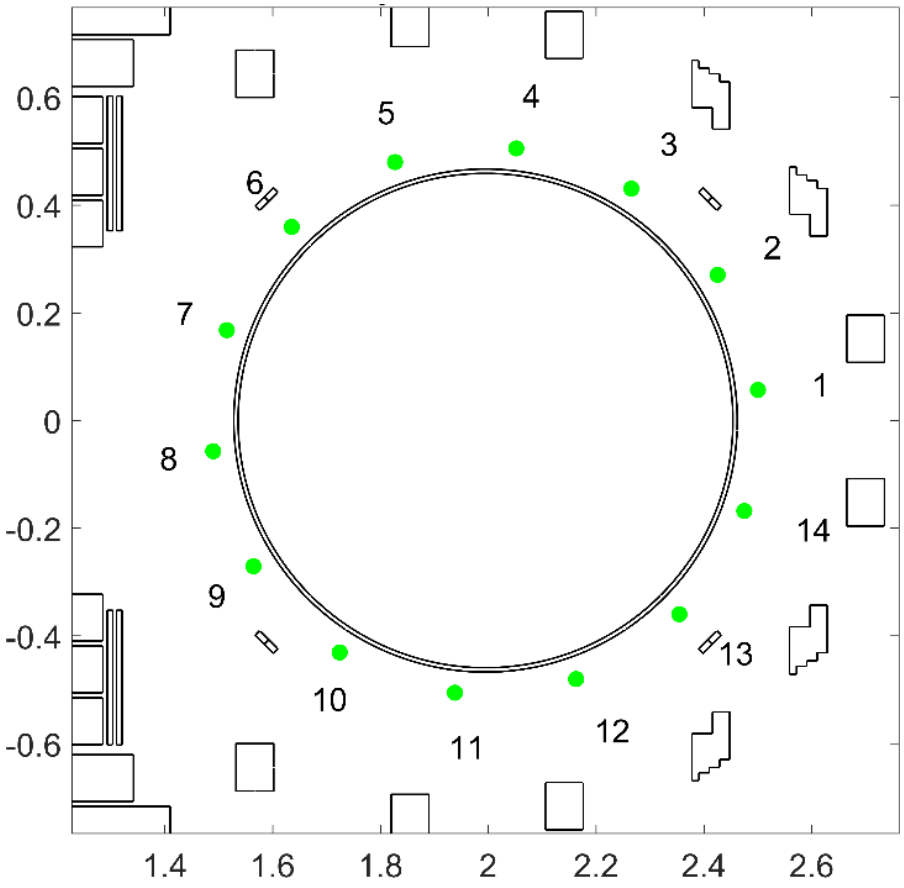

Fig. 4.10: RFX-mod2 sensors location on the poloidal plane

ID	r [m]	z [m]	θ [m]
1	2.500	0.057	6.43
2	2.426	0.270	32.14
3	2.266	0.431	57.86
4	2.052	0.505	83.57
5	1.827	0.480	109.29
6	1.635	0.360	135.0
7	1.515	0.168	160.71
8	1.490	-0.057	186.43
9	1.564	-0.272	212.14
10	1.724	-0.432	237.86
11	1.938	-0.505	263.57
12	2.163	-0.480	289.29
13	2.355	-0.360	315.0
14	2.475	-0.168	340.71

Tab. 4.3 coordinates of the RFX-mod2 pickup coils

SECTION 5

5 Plasma Equilibria in RFX-mod2

Along this work five plasma equilibria have been considered: three are computed from RFX-mod experimental data of past tokamak discharges, while the others were numerically defined for future RFX-mod2 operations [24].

Equilibria are calculated availing of the FRIDA code presented in Par. 2.2. The inputs of the computation are the currents circulating in the active coils (i.e. MW, FW and SC) and global plasma parameters. Active coils follow the numeration of the RFX-mod2 PFW mentioned in par. 4.2.1 (Fig. 4.6 /Tab. 4.1), thus the MW will be addressed recalling the sector subdivision. Plasma parameters are the total plasma current and current density profile parameters $\alpha_M, \alpha_N, \beta_0$, as defined in (2.33). For all equilibria $R_0 = 1.995\ m$ parameter is the machine major radius.

The FRIDA code provides the solution of the equilibria giving as result the poloidal flux map and the plasma current map. For the purpose of this work, it is useful to evaluate the current on the output mesh nodes, since they will be utilized for the reconstruction of the magnetic field in the positions of the new RFX-mod2 set of magnetic field sensors.

Other output parameters, like centroid position, total plasma current and plasma boundary will be useful as references for the sensitivity analysis performed in next section. In particular, the centroid position and total plasma current will be used as references to calculate the errors with respect to the parameters that will be calculated with the moments computation presented in par 3.2.1. Plasma boundary will instead be used as a meter of comparison to evaluate whether failures in certain sensors positions may lead to coarser reconstructions.

In the following are reported the errors on parameters reconstruction by means of the moments method without considering failures in the sensor set (i.e. considering all the 14 sensors).

5.1 *Shot 39122*

Active Currents [kA]	
S1	-3.344
S2	-5.424
S3	-7.314
S4	-4.923
F1	-0.07
F2	-1.266
F3	0.612
F4U	2.344
F4L	0
F5U	-2.248
F5L	0
F6	-0.653
F7	-0.351
F8	0.346
SC 1	0.015
SC 2	0.015

Plasma Parameters	
I_p	63.34 kA
α_M	0.9662
α_N	1.0529
β_0	0.7885

Moment Reconstructed Parameters (14 sensors)	
$i_{p\%}$	0.19 %
ΔCentroid	0.115 cm

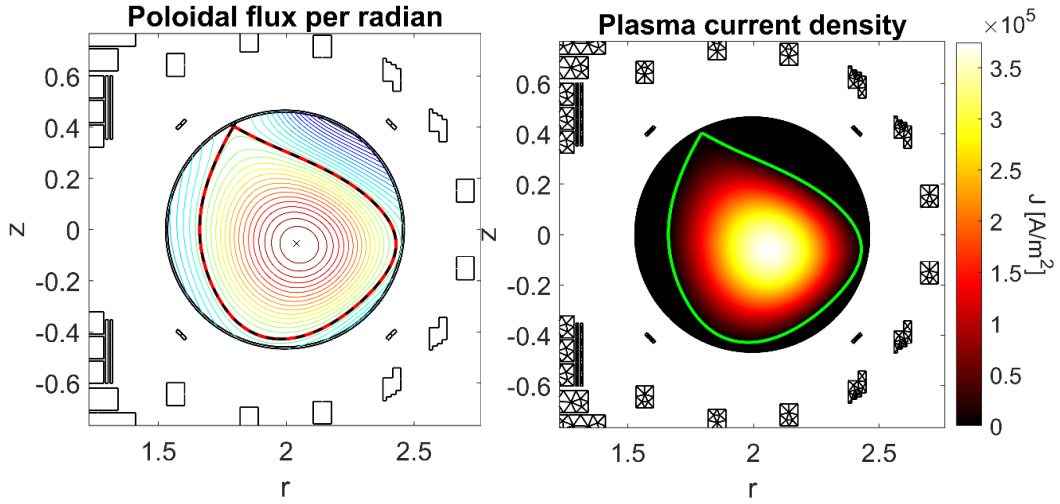

Fig. 5.1 *Shot 39122* equilibrium results: (a) Poloidal flux per radian*, (b) Plasma current density

* *Black dashed line: experimental boundary.*

5.1 *Shot 36922*

Active Currents [kA]	
S1	-2.429
S2	-4.345
S3	-4.627
S4	-5.265
F1	-0.309
F2	-1.694
F3	1.257
F4U	2.149
F4L	0
F5U	-1.970
F5L	0
F6	-0.441
F7	-0.319
F8	0.206
SC 1	0.006
SC 2	0.006

Plasma Parameters	
I_p	58.24 kA
α_M	1.2846
α_N	0.9985
β_0	0.3000

Moment Reconstructed Parameters (14 sensors)	
$i_{p\%}$	0.17 %
ΔCentroid	0.055 cm

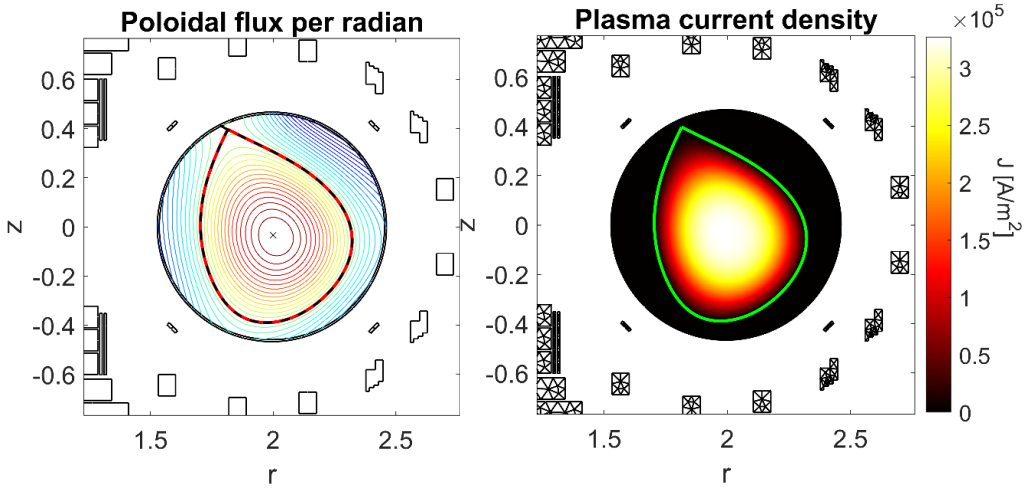

Fig. 5.2 *Shot 36922* equilibrium results: (a) Poloidal flux per radian*, (b) Plasma current density

* *Black dashed line: experimental boundary.*

5.1 *Shot 37829*

Active Currents [kA]	
S1	-0.249
S2	-2.094
S3	-4.128
S4	-2.945
F1	-0.290
F2	-1.652
F3	1.156
F4U	0
F4L	1.944
F5U	0
F5L	-1.695
F6	-0.392
F7	-0.275
F8	0.204
SC 1	-0.001
SC 2	0.001

Plasma Parameters	
I_p	58.24 kA
α_M	1.3237
α_N	1.1998
β_0	0.1000

Moment Reconstructed Parameters (14 sensors)	
$i_{p\%}$	0.17 %
ΔCentroid	0.076 cm

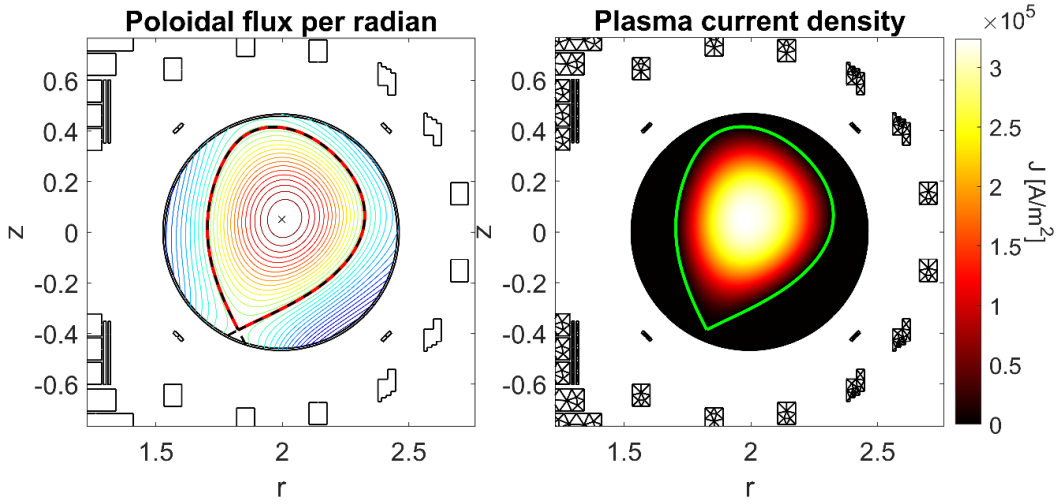

Fig. 5.3 *Shot 37829* equilibrium results: (a) Poloidal flux per radian*, (b) Plasma current density

* *Black dashed line: experimental boundary.*

5.1 *Shot DEMO-like* δ_L

Active Currents [kA]

S1	-0.176
S2	-0.176
S3	-0.176
S4	-0.176
F1	-2.337
F2	-3.168
F3	-0.004
F4	-1.191
F5	-1.313
F6	-0.772
F7	-0.354
F8	-0.226

Plasma Parameters	
I_p	89.16 kA
α_M	1.0810
α_N	1.0170
β_0	0.4890

Moment Reconstructed Parameters (14 sensors)	
$i_{p\%}$	0.16 %
ΔCentroid	0.006 cm

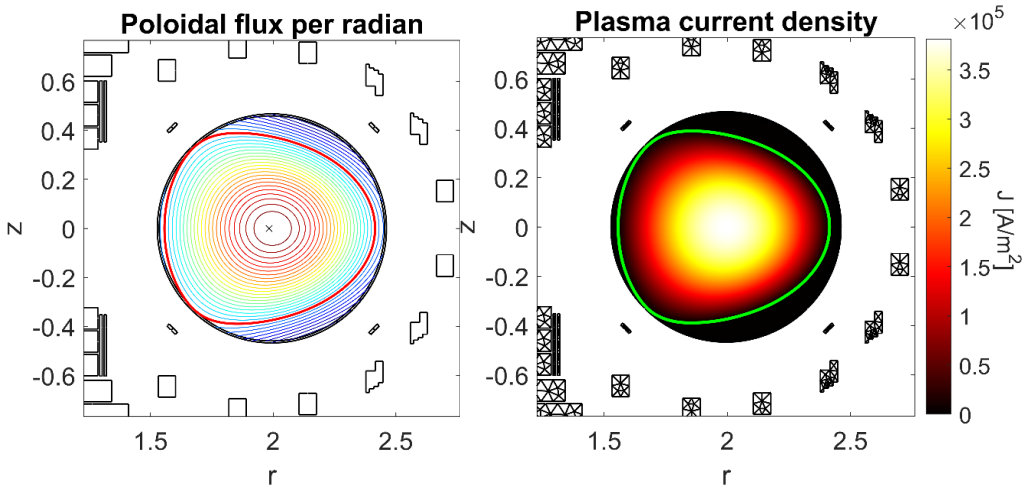

Fig. 5.4 *Shot* δ_L equilibrium results: (a) Poloidal flux per radian*, (b) Plasma current density

5.1 *Shot Negative Triangularity – L-mode (NT_L)*

Active Currents [kA]

S1	-1.231
S2	-2.740
S3	-3.684
S4	-2.179
F1	0.338
F2	-0.286
F3	-1.031
F4U	-2.266
F4L	0
F5U	1.936
F5L	0
F6	0.250
F7	-1.019
F8	0.014

Plasma Parameters	
I_p	61.05 kA
α_M	0.5014
α_N	1.0985
β_0	0.6801

Moment Reconstructed Parameters (14 sensors)	
$i_{p\%}$	0.18 %
ΔCentroid	0.061 cm

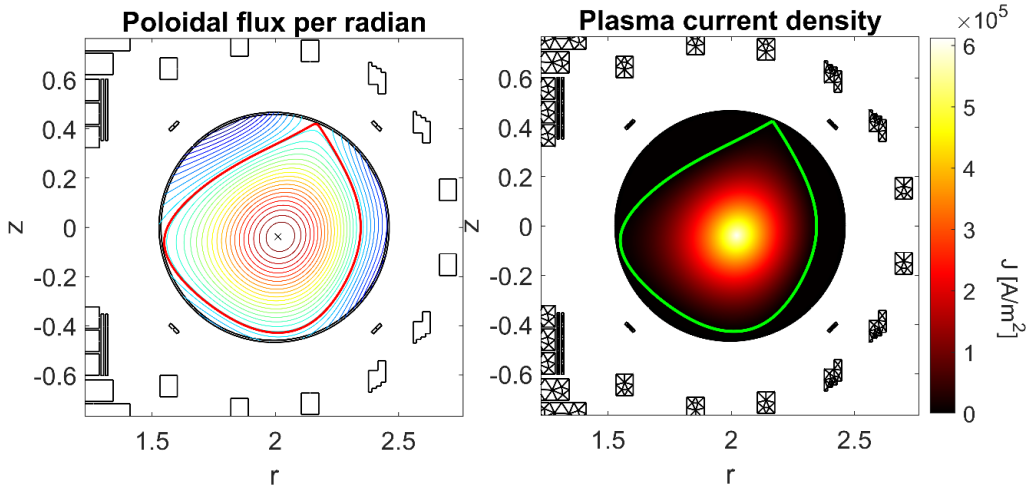

Fig. 5.5 *Shot NT_L* equilibrium results: (a) Poloidal flux per radian*, (b) Plasma current density

SECTION 6

6 Analysis of plasma parameters reconstruction, considering the potential failure of RFX-mod2 poloidal field sensors

In this section, the goal is to analyse the robustness of the moment reconstruction method presented in Section 3, considering several fault conditions of the magnetic sensors. In particular, the focus is on evaluating which could be the most impacting fault configurations in plasma parameters reconstruction. Thus, a sensitivity analysis on the magnetic reconstruction of plasma parameters in several RFX-mod2 equilibria is presented considering the impact of sensor failures in different configurations. Then, the robustness of the model is tested against the presence of noise in the measurements.

The results could be of particular interest for the plasma control system. Since real-time active control is based on data retrieved from discharge parameters, it is mandatory that a suitable reconstruction method should be sufficiently accurate, even in fault conditions.

6.1 Analysis Procedure

In this section, different sets of sensors from the future magnetic sensor system of RFX-mod2 experiment will be used for the reconstruction of the main plasma parameters.

In first place, the equilibria presented in Section 5 are characterized with FRIDA code and the reference parameters (i.e. plasma centroid position and total plasma current) are evaluated. Then, with suitable Green matrices, synthetic measurements on RFX-mod2 pick-up coil positions are computed and a reconstruction of $n = 0, 1, 2,$ moments, with the method presented in par. 3.2.2, is performed. The synthetic field components are mapped from (r, z) coordinates system to a local one with tangential and normal components (t, n), which is related to the measurement directions of each sensor. The moment computation has been performed considering only the tangential component B_t, which is higher in magnitude with respect to the normal one.

The impact of sensor failures is considered in the computation of the moments for different plasma equilibria, with particular focus in trying to find the most critical configurations in terms of higher errors on plasma parameters reconstruction. Moreover, the impact of noise on sensor measurements will be quantified for

some of the considered sensor failure configurations and for different plasma equilibria.

In order to define the possible configurations of faulty sensors, a *characteristic angle* is defined. Then, the relation between this angle and the error on the computed centroid and total plasma current is evaluated. The analysis shows a strong correlation between errors and few equilibrium parameters such:

- the position of the FRIDA centroid with respect to the machine centre
- the plasma-first-wall distance (PL-FW)
- the amplitude of magnetic field B_t measured by the sensors, with respect to the normal component. This is meant to assess whether the magnitude of the tangential component may bias the sensitivity of the sensors.

In the following, we will refer to a reference polar coordinate system derived from the one presented in Section 2 and represented in Fig. 2.1: the origin is the machine centre, MC: $(r_{MC} = 1.995;\ z_{MC} = 0)$, and the poloidal angle θ is counted counterclockwise, as show in Fig 6.1:

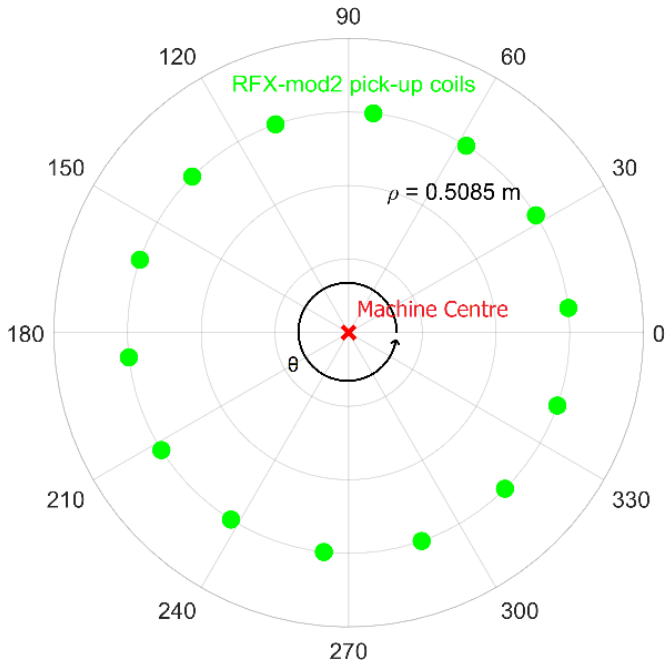

Fig. 6.1: Pick-up coils reference system

Computation of moments is performed for all the possible combinations of sensor failures, from one to 12 faulty sensors, which means that they are not considered in the moments computation ("turned off").

Given $n = 14$ total number of sensors and let k be the number of faulty sensors, the combination of sensors to analyse are the simple combinations of k of n elements

$$\boldsymbol{C} = \binom{n}{k} = \frac{n!}{k!\,(n-k)!} \tag{4.6}$$

For each combination, the characteristic angle of the sensors is computed, representing the "direction" in which the sensor failure is considered.

For each equilibria, the position of the centroid is calculated by means of the FRIDA code. Considering the reference system of Fig 6.1, the angle between FRIDA centroid and MC will be accounted as *reference direction*.

The computation of the characteristic angle considers the position of the FRIDA centroid with respect to the MC, thus giving more importance to the measurements in the reference direction. This allows to take into account the higher probability of having higher errors when faults happen in the FRIDA reference direction.

The procedure for the calculation of the characteristic angle can be found in Section A of the Appendix.

The results of the various combinations depending on the number of faulty sensors k are here presented. Data are ordered by the characteristic angle in the reference system of Fig 6.1; then, and PL-FW distance and B_n/B_t are plotted against θ; in order to highlight relevant regions.

Two configurations, the best and the worst case for centroid reconstruction, are analysed with respect to several noise percentages in the poloidal field measurements, for each number of faulty sensors. This allows to verify the capability of the moment method for properly reconstruction of plasma parameters under several disturbances conditions.

The noise is generated starting from a timestamp seed ("simdTwister" fast algorithm) [25] to ensure that for every computation the error will result always different: in fact, starting from a fixed seed, could lead to patterns in the noise generation and therefore make the algorithm not random.

Since the noise generated is between 0 and 1, this value is added to another random term but this time with negative sign, making it to fall in the range [-1, 0]. So, as wanted the sum of the two terms is a random value $r \in [-1, 1]$.

The new value of the magnetic field on sensor positions can thus be calculated:

$$\boldsymbol{B_t} = \boldsymbol{B_t} + \boldsymbol{n}_{\%} * \|\boldsymbol{B_{tn}}\| * r \tag{4.7}$$

where $\|\boldsymbol{B_t}\|$ is the 2-norm of the vector of measured field along the tangential component, $\boldsymbol{n}_{\%} = l \cdot 0.002$, with $l = 1, \dots, 20$, and $r \in [-1, 1]$ is a random number.

It is important to mind that the $\boldsymbol{n}_{\%}$ values refer to the maximum noise values, and since $r \in [-1, 1]$, the actual added noise value won't correspond exactly to $\boldsymbol{n}_{\%}$. Due to this fact, for every percentage of noise, the calculation of the moments is carried out 100 times, and a statistical analysis is performed on the data (Fig. 6.2).

Average values of the centroid distance from 0%-noise centroid position, and error with respect to 0%-noise plasma current are computed, and the result are shown in the following paragraph.

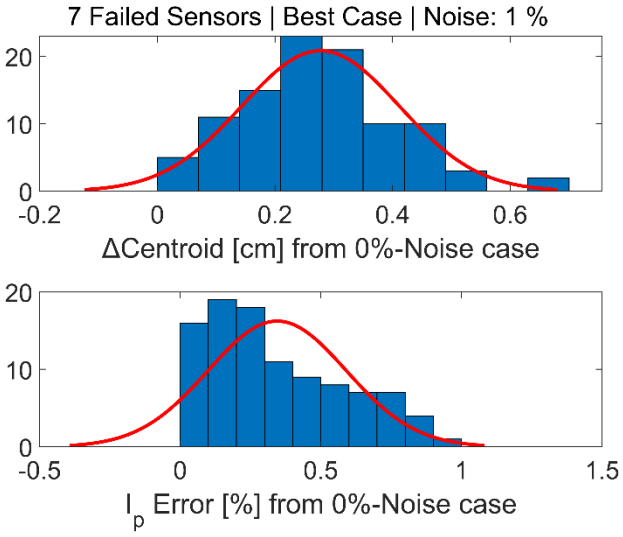

Fig 6.2: Noise computation example: *Shot 39122*, 7 failed sensors best case (1, 4, 5, 6, 8, 9, 11 OFF), 100 values distribution with 1% noise

6.2 Results

In the following paragraph will be reported the most relevant results of the analysis. In first place, considerations with just one faulty sensor are reported, since it is a very useful limit case to assess the changes in plasma reconstructed parameters for each empty position in the sensor set. In Fig 6.3-6.7 are reported the centroid distances from FRIDA reference for each faulty sensor with a colormap scale; in particular, Fig 6.3a-6.7a display the distance in terms of the characteristic angle calculated as Appendix, (banally the sensor angle with respect to the MC for this limit case).

The procedure shows that higher errors (i.e. worst reconstructions) are obtained when faults occur in the reference direction, where PL-FW distance is lower, and, less preponderantly, where is present a higher magnitude of B_t over B_n. In Fig. 6.3b-6.7b colormap is shown over the very sensor position, to better visualize the most critical positions to have fault in the sensor set, and it is clear how, for different equilibria, the worst positions relate to the plasma shape as described.

An exception in this PL-FW criterion is seen in the region of the null point, where a close distance between plasma and first-wall is present, but parameters can be reconstructed with a quite high accuracy. This can be explained by the fact that the tangential component of magnetic field has a minimum in amplitude as required by X-point configurations.

Shot 39122

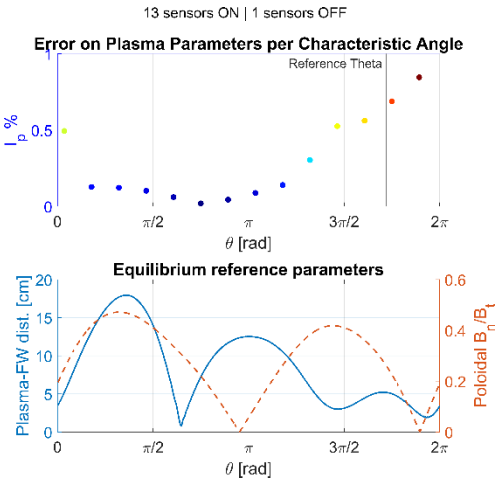

Fig. 6.3a: *Shot 39122* Centroid distance in function of angle of the broken sensor. Exact position of the sensor in reported in 4.2b. The lower graph reports the PL-FW distance and the absolute value of the quantity of the poloidal B_n/B_t

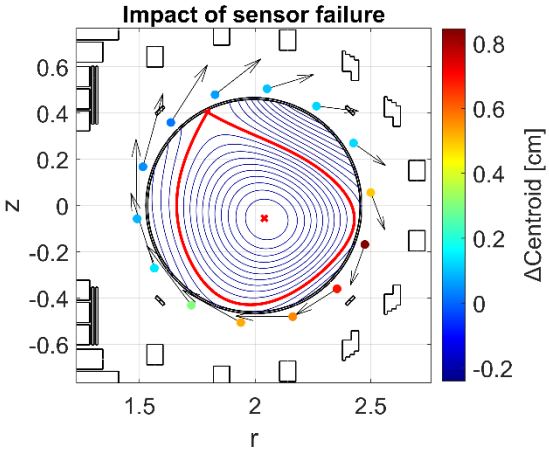

Fig 6.3b: *Shot 39122* Sensor positions with ΔCentroid colormap over.

Shot 36922

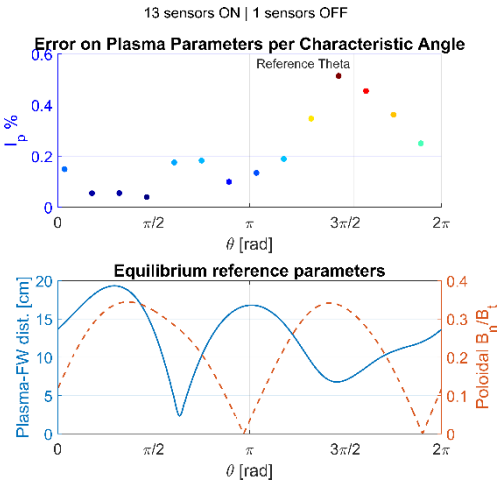

Fig. 6.4a: *Shot 36922* Centroid distance in function of angle of the broken sensor.

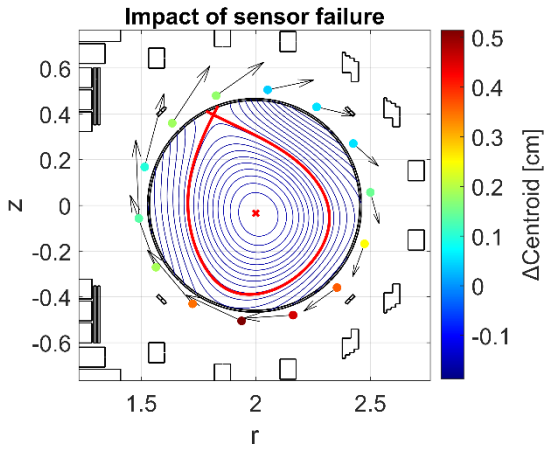

Fig 6.4b: *Shot 36922* Sensor positions with ΔCentroid colormap over.

Shot 37829

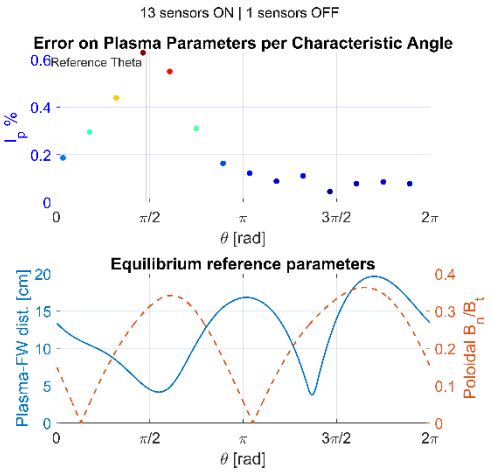

Fig. 6.5a: *Shot 37829* Centroid distance in function of angle of the broken sensor.

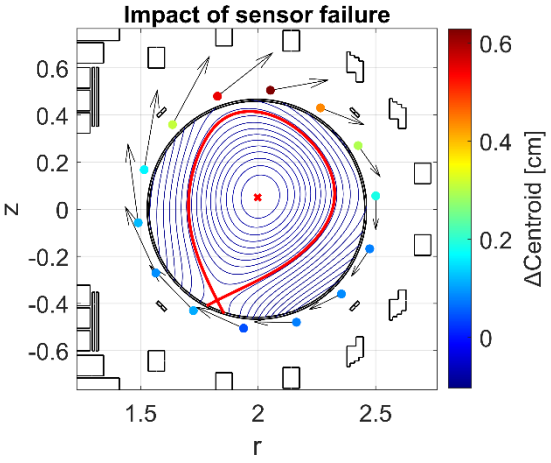

Fig 6.5b: *Shot 37829* Sensor positions with ΔCentroid colormap over.

Shot DEMO-like δ_L

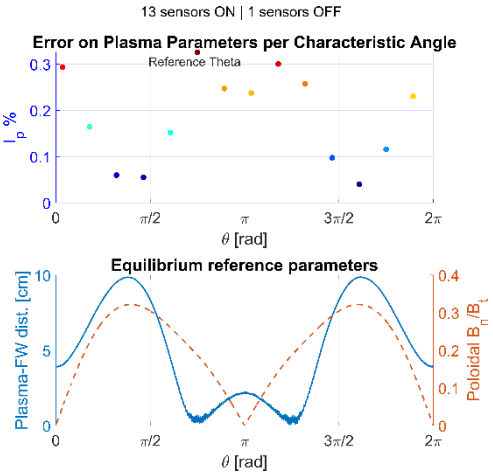

Fig. 6.6a: *Shot δ_L* Centroid distance in function of angle of the broken sensor.

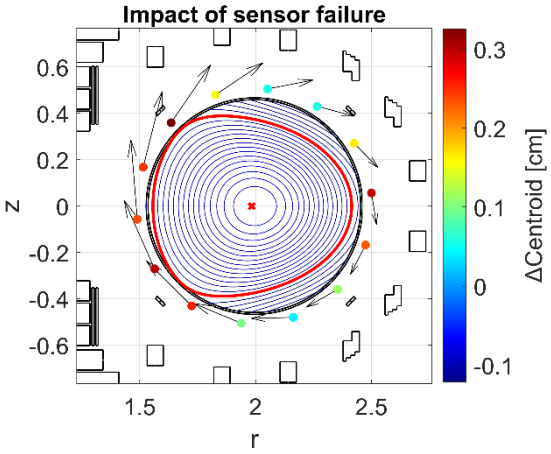

Fig 6.6b: *Shot δ_L* Sensor positions with ΔCentroid colormap over.

Shot Negative Triangularity (L-mode) - NT_L

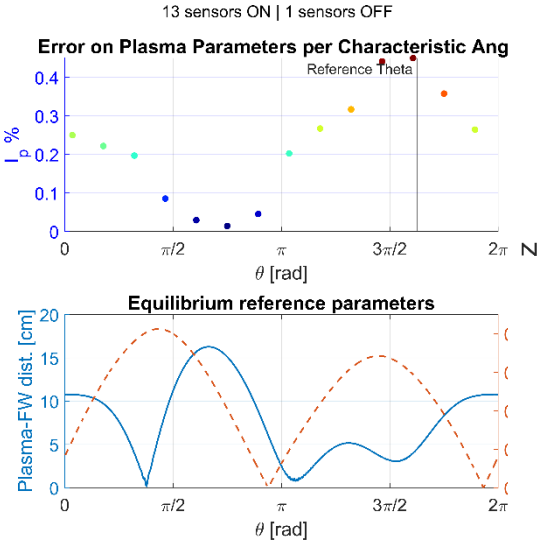

Fig. 6.7a: *Shot* NT_L Centroid distance in function of angle of the broken sensor.

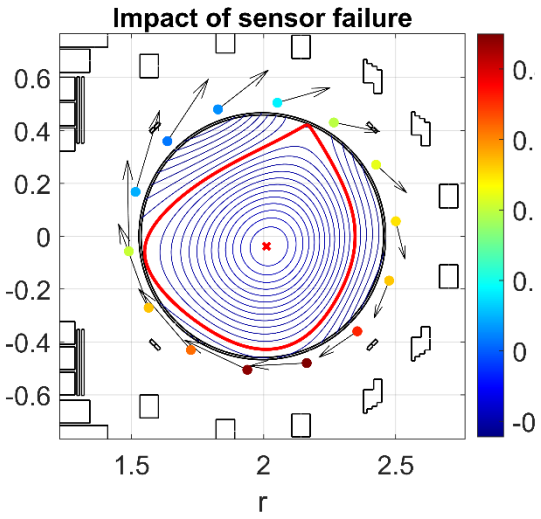

Fig 6.7b: *Shot* NT_L Sensor positions with ΔCentroid colormap over.

The following graphs (Fig. 6.8-12) shows angular distribution of calculated parameters accounting the characteristic angle of the faulty sensor set. For each set of faulty sensors, their characteristic angle is computed with the aforementioned method, thus errors on plasma parameters are placed in the corresponding angle of the reference system (Fig. 6.1). The same pattern as the case considering the failure of one sensor is repeated along other configurations when increasing the numbers of failures; being clear that, in some cases, when the characteristic angle is located near the reference direction, parameters maybe result still well reconstructed. This fact is due to compensations between sensors in opposite positions (i.e. symmetric configurations). Nevertheless, worst configurations results when sensors fail in reference direction.

To highlight these worst directions, the upper bound of configurations' angular distribution is put in evidence and, as expected, the peak of the highest error values is located in proximity of the reference direction. In particular, is interesting to notice how, for different equilibria, the peak of displacements matches the angle of FRIDA centroid with remarkable precision.

The same results are displayed also on polar plots (Fig. 6.8-12 (b,d,f)) for a better visualization. Other configurations with different numbers of faulty sensors have been reported in Section B.1 of the Appendix.

Shot 39122

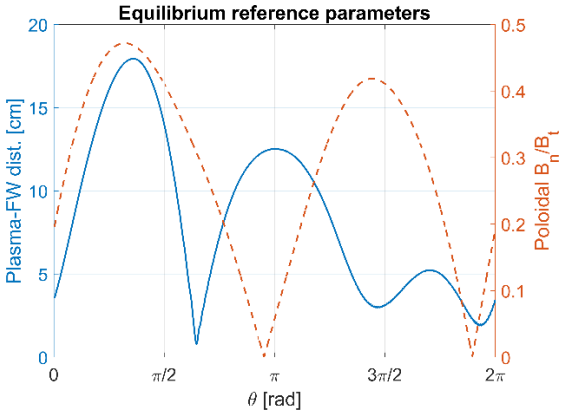

Fig. 6.8a: *Shot 39122* – Reference Parameters

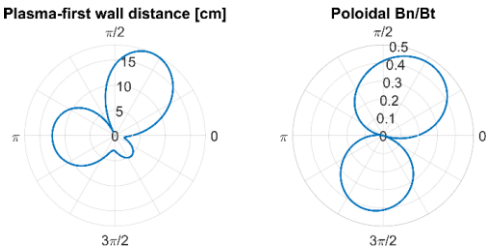

Fig 6.8b: *Shot 39122* – Reference Parameters (polar plot)

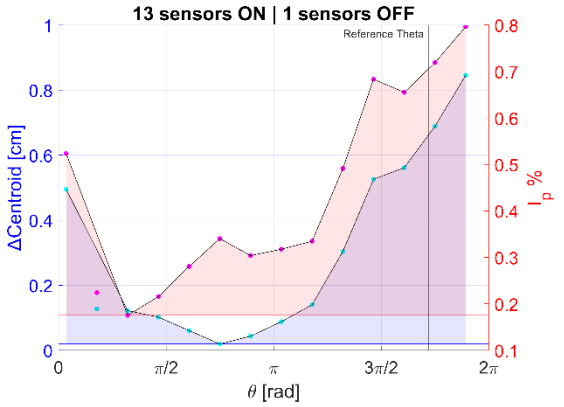

Fig. 6.8c: *Shot 39122* – 1 sensor off

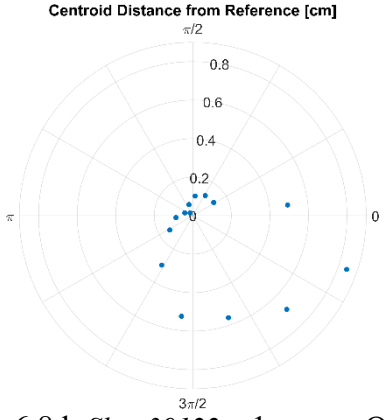

Fig 6.8d: *Shot 39122* – 1 sensor OFF (polar plot)

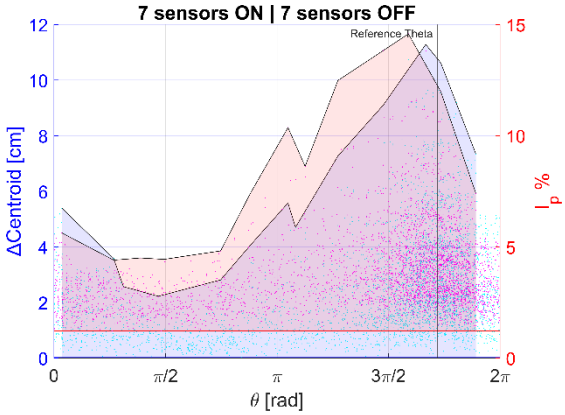

Fig. 6.8e: *Shot 39122* – 7 sensors off

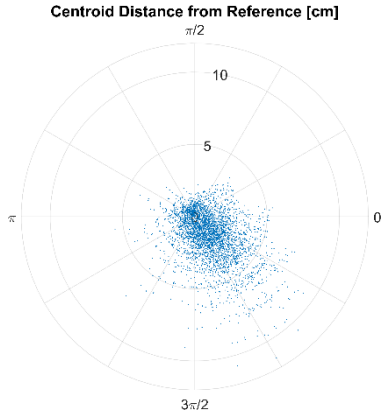

Fig 6.8f: *Shot 39122* – 7 sensors OFF (polar plot)

Shot 36922

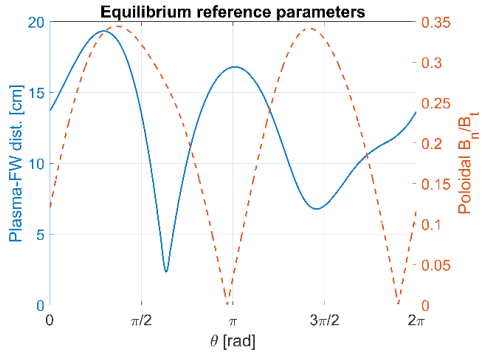

Fig. 6.9a: *Shot 36922* – Reference Parameters

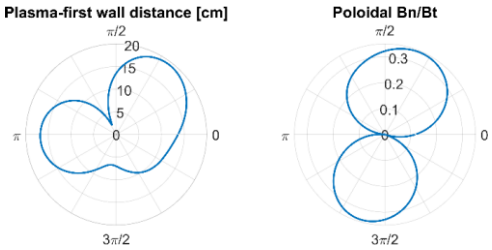

Fig 6.9b: *Shot 36922* – Reference Parameters (polar plot)

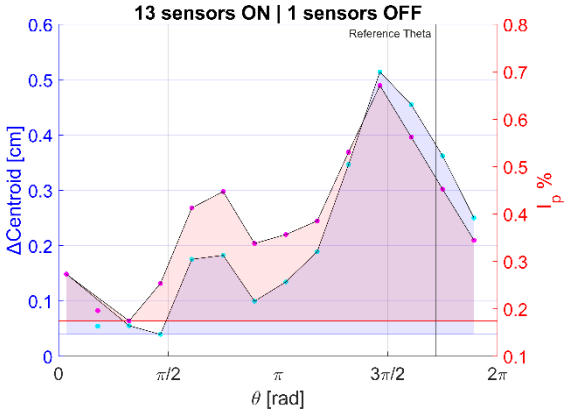

Fig. 6.9c: *Shot 36922* – 1 sensor off

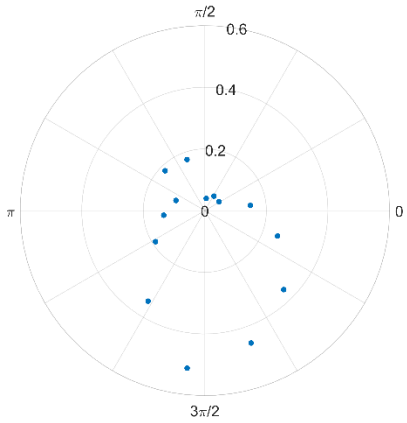

Fig 6.9d: *Shot 36922* – 1 sensor OFF (polar plot)

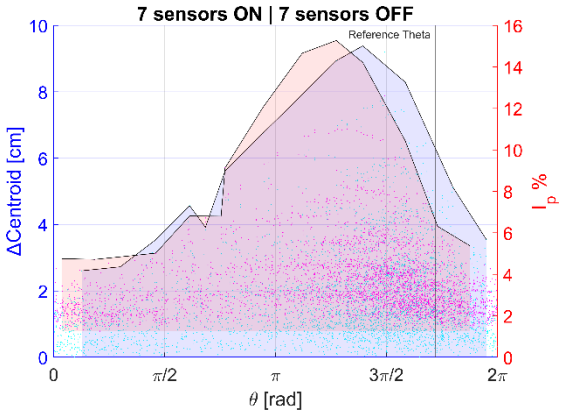

Fig. 6.9e: *Shot 36922* – 7 sensors off

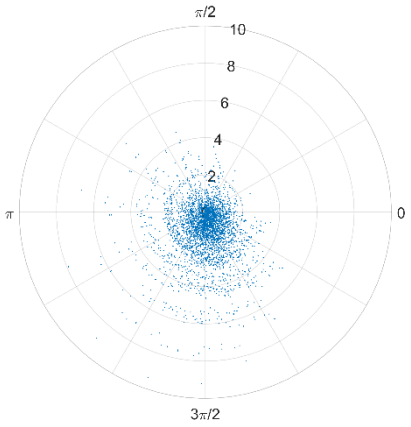

Fig 6.9f: *Shot 36922* – 7 sensors OFF (polar plot)

Shot 37829

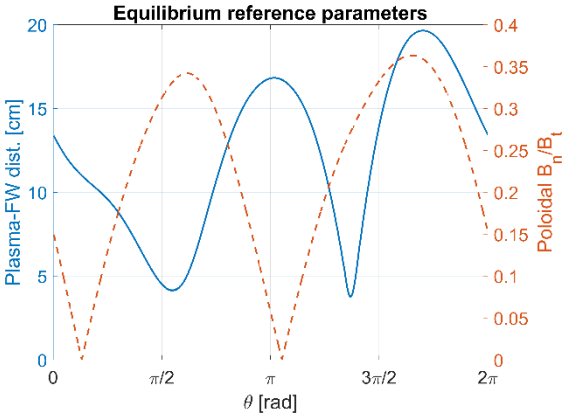

Fig. 6.10a: *Shot 37829* – Reference Parameters

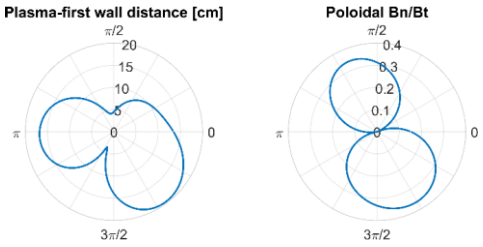

Fig 6.10b: *Shot 37829* – Reference Parameters (polar plot)

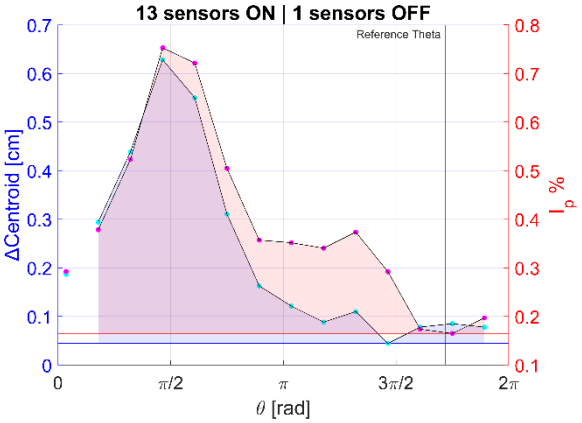

Fig. 6.10c: *Shot 37829* – 1 sensor off

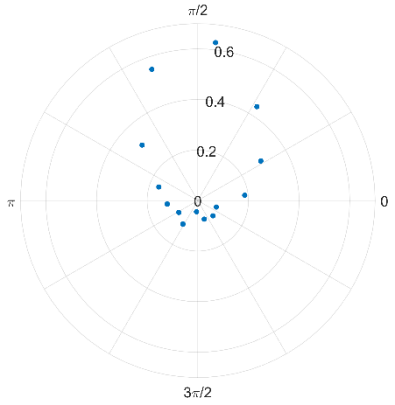

Fig 6.10d: *Shot 37829* – 1 sensor OFF (polar plot): Centroid distance from reference

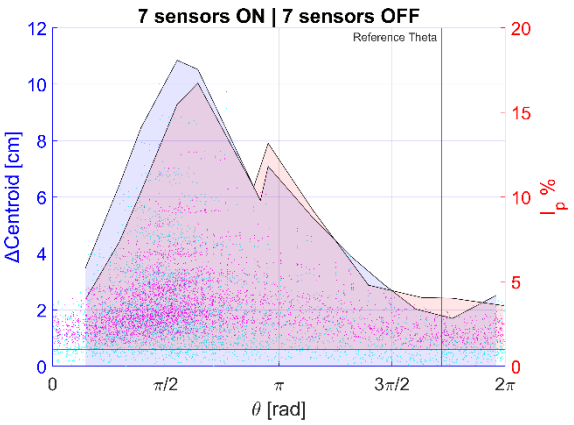

Fig. 6.10e: *Shot 37829* – 7 sensors off

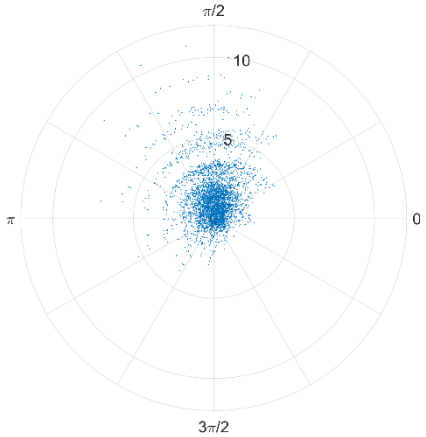

Fig 6.10f: *Shot 37829* – 7 sensors OFF (polar plot): Centroid distance from reference

Shot DEMO-like δ_L

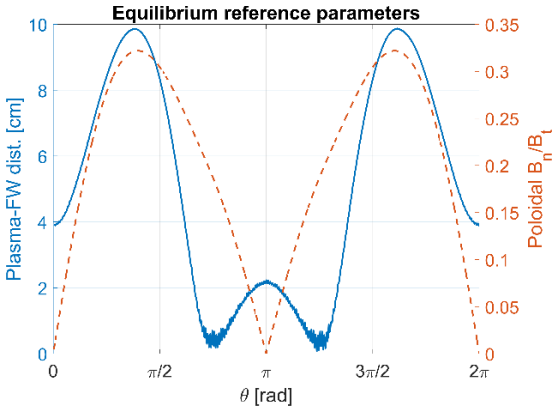

Fig. 6.11a: *Shot* δ_L – Reference Parameters

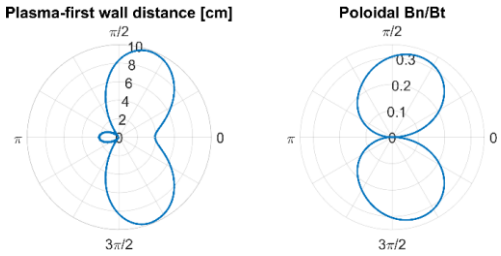

Fig 6.11b: *Shot* δ_L – Reference Parameters (polar plot)

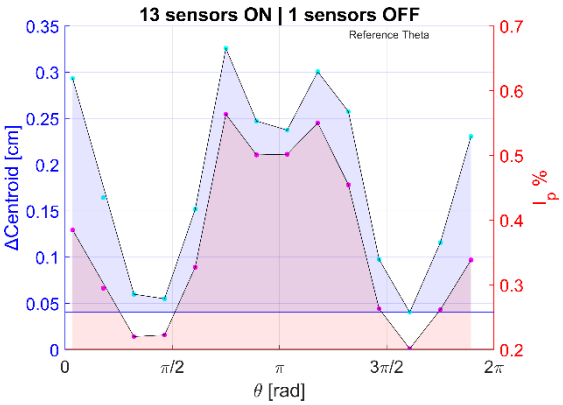

Fig. 6.11c: *Shot* δ_L – 1 sensor off

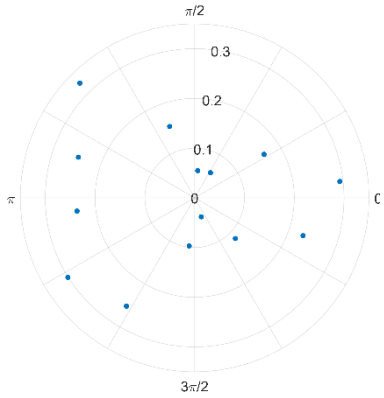

Fig 6.11d: *Shot* δ_L – 1 sensor OFF (polar plot): Centroid distance from reference

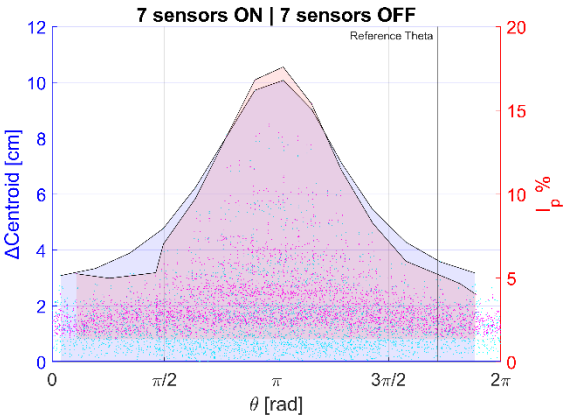

Fig. 6.11e: *Shot* δ_L – 7 sensors off

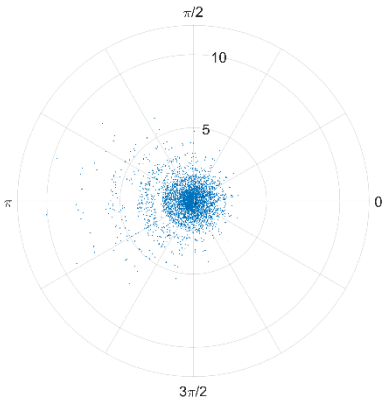

Fig 6.11f: *Shot* δ_L – 7 sensors OFF (polar plot): Centroid distance from reference

Shot NT_L

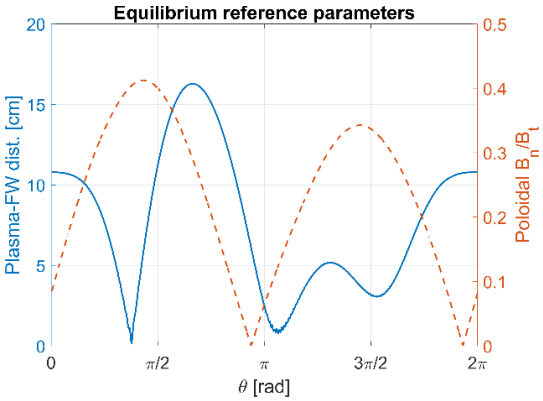

Fig. 6.12a: *Shot NT_L* – Reference Parameters

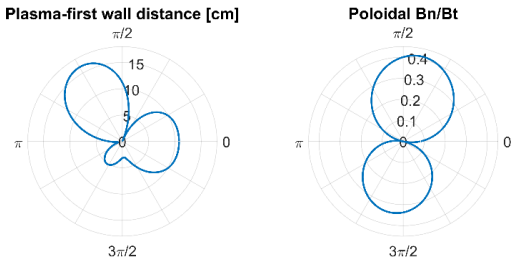

Fig 6.12b: *Shot NT_L*– Reference Parameters (polar plot)

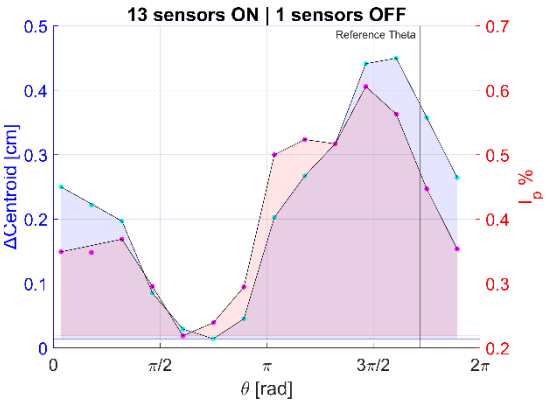

Fig. 6.12c: *Shot NT_L* – 1 sensor off

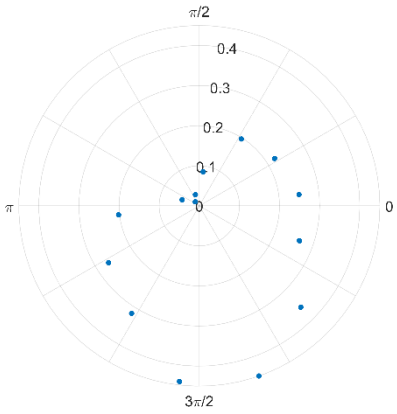

Fig 6.12b: *Shot NT_L* – 1 sensor OFF (polar plot): Centroid distance from reference

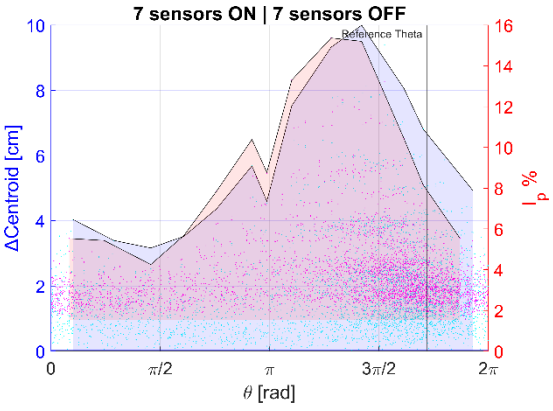

Fig. 6.12e: *Shot NT_L* – 7 sensors off

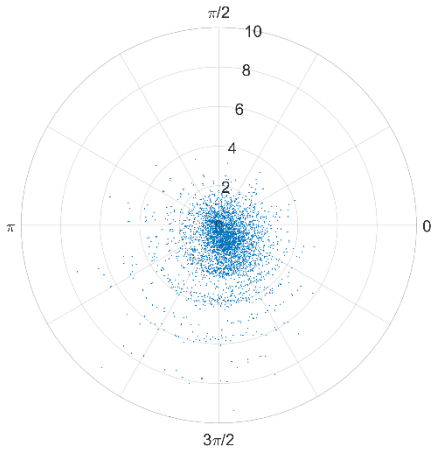

Fig 6.12f: *Shot NT_L* – 7 sensors OFF (polar plot): Centroid distance from reference

6.2.1 Configurations overview

Until it was shown each graph representing the distribution of the calculated error on plasma parameters in function of the characteristic angle, and has been shown how the fault of a sensor in the reference direction (or a sensor in a region where plasma-first-wall distance is very low) could lead to a coarser reconstruction of plasma current and centroid position.

Now, instead, all the configurations represented in the plot against θ are considered at once and attributed to the respective number of faulty sensors. Due to the relatively big amount of data some graphical simplifications are performed. For each equilibrium a confidence plot has been produced (Fig 6.13). These represent, for each number of faulty sensors, the mean value of plasma parameters (solid line) and the interval between minimum and maximum value between all the configuration of the case (coloured area).

Furthermore, a box-plot has been adopted to better frame up parameters distribution as the number of faulty sensors increases (Fig 6.14). On each box, the central mark indicates the median, and the bottom and top edges of the box indicate the 25^{th} and 75^{th} percentiles, respectively. The whiskers extend up to one interquartile length, being $w_{max} = q_{75} + (q_{75} - q_{25})$ and $w_{min} = q_{25} - (q_{75} - q_{25})$. Percentiles are extremely useful in this case because can quantify the value under which is located a certain percentage of data, making it useful to evaluate, in a real case, the entity of plasma parameter errors, relying solely on the number of faulty sensors.

Both the types of graphs show a steeper slope of the upper bound with respect to the lower one. The lower bound represents the best reconstructions for each number of faulty sensors, in particular, it is shown how centroid (Fig. 6.13a) can be reconstructed with remarkable precision even when a low number of working sensors is present. This could happen under the condition of having the sensors almost equally distributed (i.e. in a symmetric sensors configurations).

The upper bound represents the worst configurations and can be seen that centroid displacement follows an almost linear behaviour. Error on plasma current instead does not increase linearly with the number of faulty sensors (Fig. 6.13b).

In this section is reported only the case for *Shot 39122*. Graphs concerning other equilibria are similar (errors show similar behaviours and magnitudes) with respect to the ones shown in Fig. 6.13-14 and thus can be found in section B.2 of the Appendix.

Shot 39122

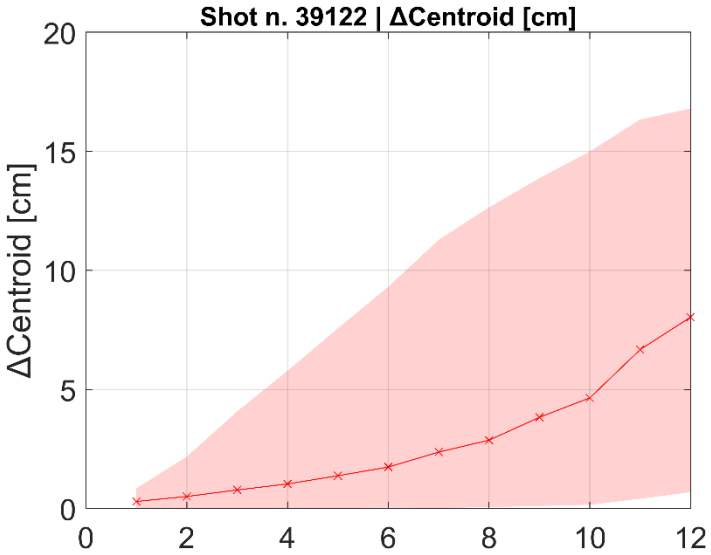

Fig. 6.13a: *Shot 39122*: ΔCentroid (range plot vs. n. of faulty sensors)

	[cm]		
n.	*Mean*	*Min.*	*Max.*
1	0.29	0.02	0.85
2	0.50	0.01	2.17
3	0.78	0.02	4.07
4	1.03	0.02	5.78
5	1.37	0.02	7.56
6	1.74	0.04	9.31
7	2.36	0.02	11.28
8	2.86	0.06	12.65
9	3.80	0.10	13.87
10	4.65	0.16	14.99
11	6.66	0.41	16.34
12	8.04	0.68	16.80

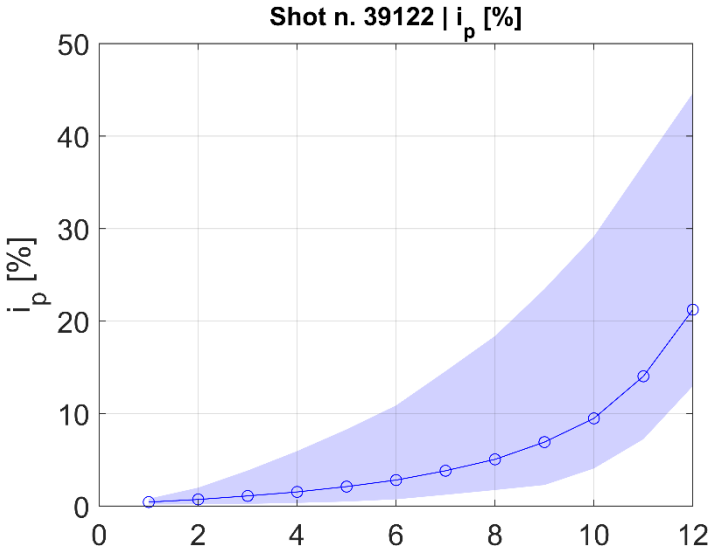

Fig. 6.13b: *Shot 39122*: I_p error (range plot vs. n. of faulty sensors)

	[%]		
n.	*Mean*	*Min.*	*Max.*
1	0.43	0.18	0.80
2	0.72	0.18	1.99
3	1.10	0.24	3.84
4	1.53	0.34	5.95
5	2.11	0.49	8.29
6	2.81	0.73	10.88
7	3.82	1.23	14.58
8	5.05	1.74	18.38
9	6.92	2.28	23.46
10	9.48	4.07	29.16
11	14.03	7.23	36.92
12	21.23	12.97	44.64

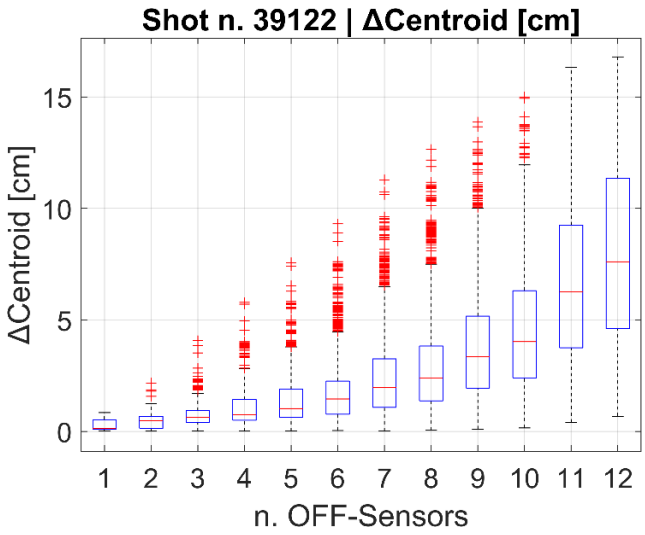

[cm]

n.	*Median*	*75 pc*	*25 pc*
1	0.13	0.53	0.09
2	0.48	0.68	0.14
3	0.64	0.93	0.41
4	0.76	1.43	0.50
5	1.03	1.89	0.62
6	1.46	2.26	0.77
7	1.96	3.25	1.08
8	2.38	3.83	1.38
9	3.35	5.17	1.94
10	4.03	6.31	2.40
11	6.26	9.25	3.75
12	7.61	11.35	4.60

Fig. 6.14b: *Shot 39122*: ΔCentroid (Box-plot)

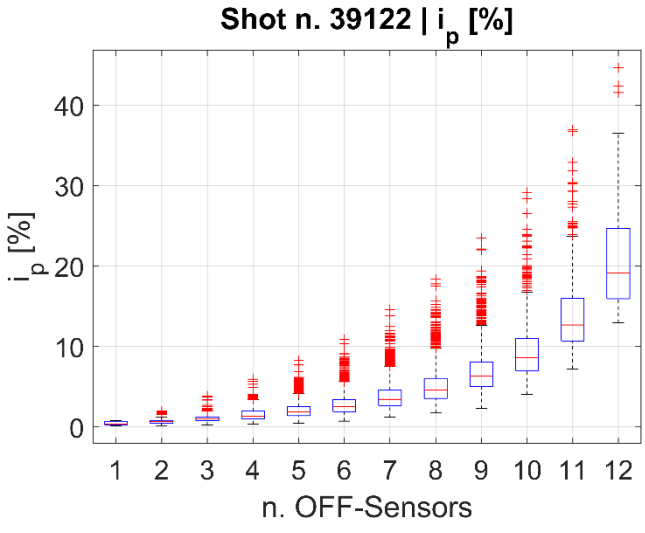

[%]

n.	*Median*	*75 pc*	*25 pc*
1	0.38	0.66	0.28
2	0.70	0.83	0.46
3	0.98	1.25	0.77
4	1.33	1.97	1.03
5	1.90	2.52	1.40
6	2.55	3.40	1.90
7	3.44	4.60	2.65
8	4.61	6.05	3.55
9	6.34	8.01	5.04
10	8.61	10.97	7.01
11	12.68	15.97	10.69
12	19.15	24.68	15.94

Fig. 6.14b: *Shot 39122*: I_p error (Box-plot)

6.2.2 ΔCentroid vs. I_p error relation

Another interesting behaviour that has been found, is the gradual non-linearity of the plasma current error with respect to the correspondent centroid error of the faulty sensor set, while increasing the number of broken sensors.

To better visualize the results a linear fit and a cubic one has been chosen: the linear one is applied from 1 to 8 sensors off, and cubic fit is applied from 4 to 14 sensors off. This illustrates well the gradual sharpening of the characteristic.

Right away (Fig. 15-17) are reported three examples concerning *Shot n. 39122*, in particular cases with 1, 7 and 11 faulty sensors. Other cases and, respectively, considering other equilibria, are reported in Section B.3 of the Appendix.

Shot 39122

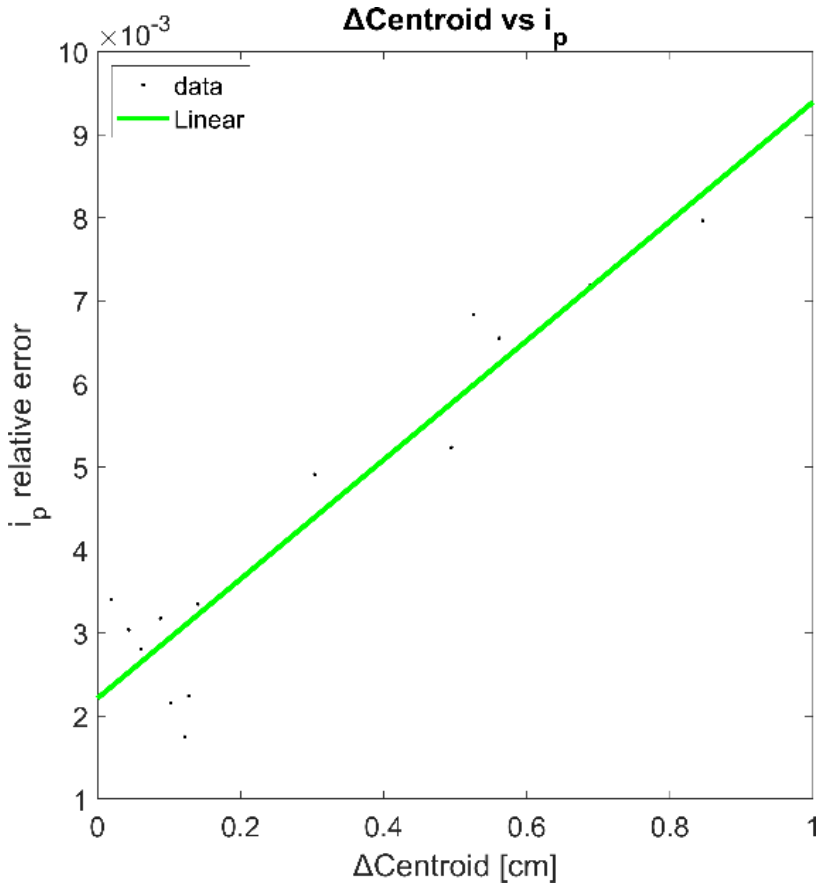

Fig. 6.15: *Shot 39122* – 1 sensor off: ΔC *vs* i_p%

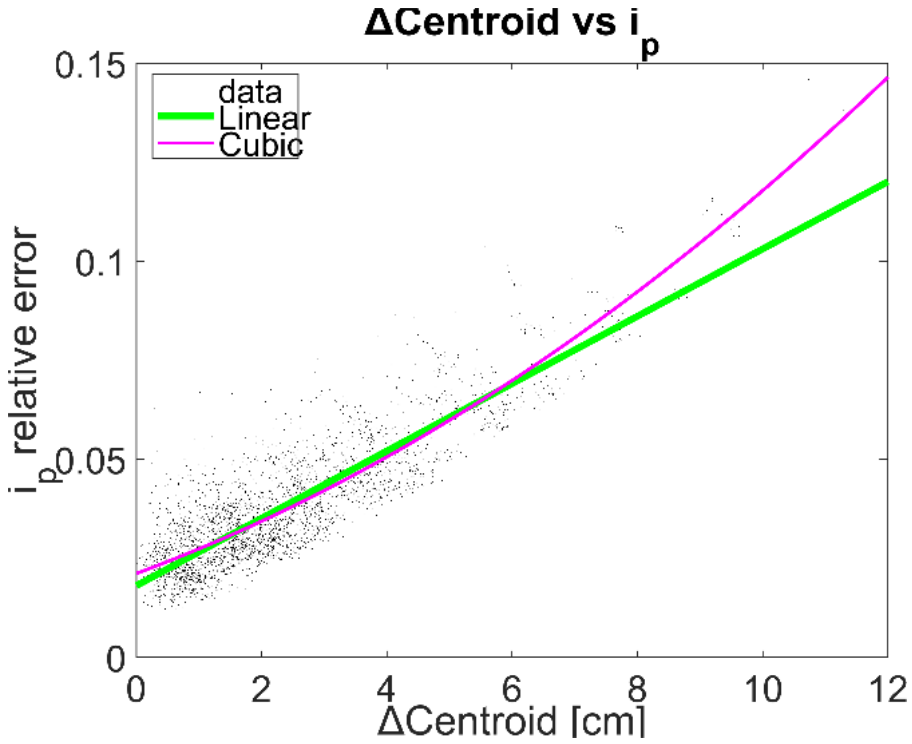

Fig 6.16: *Shot 39122* – 7 sensors off: ΔC *vs* i_p%

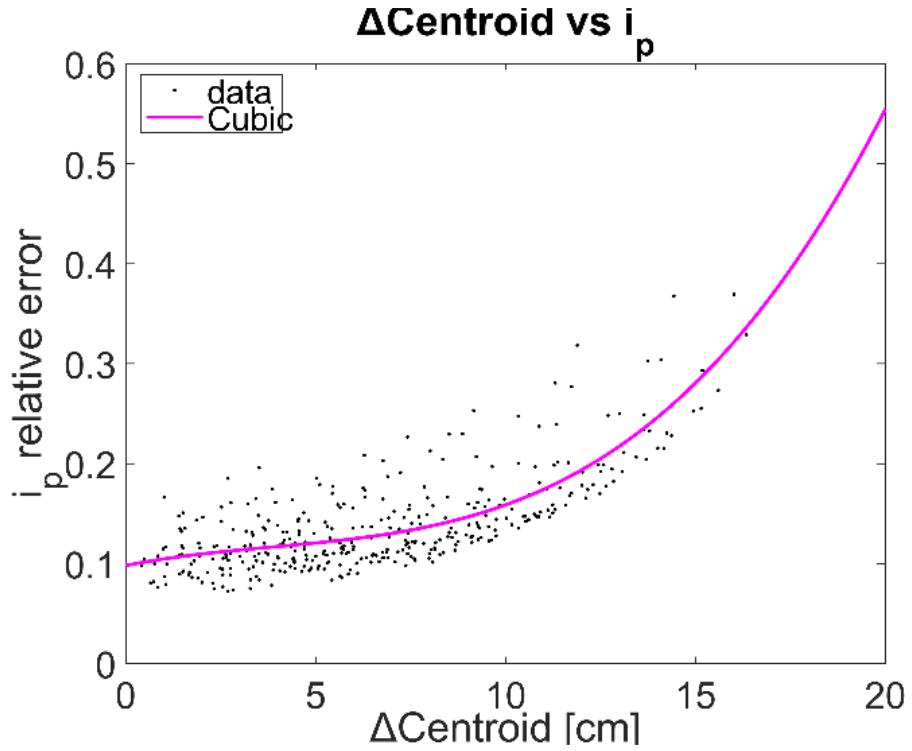

Fig 6.17: *Shot 39122* – 11 sensors off: ΔC *vs* i_p%

6.2.3 Noises analysis results

In the configurations that have been chosen to be analysed against noisy measurements, tangential component of the poloidal magnetic field has been added by 20 different amounts of noise values, with which the moment computation has been repeated 100 times each. Plasma parameters retrieved from moment calculation are then used to find the errors with respect to the case without noise. For each noise level the mean error μ and standard deviation σ are computed. The choice of changing the reference parameter for the error calculation is guided by the fact that noise contribution won't be so drastic when referring to FRIDA parameters, especially in worst configurations, where errors due to faults are dominant.

Knowing that the minimum value that could be measured by RFX-mod2 pick-up coils is $0.1\ mT$, noise levels has been chosen from 0.2% and 4% of the RMS of the magnetic field measured by the sensors. In absolute terms it is equal to ~ 0.2 to $\sim 4\ mT$.

The errors on both plasma parameters grow linearly with the noise level, as shown in Fig 6.18-19. It is found an error of centroid position from 0%-noise condition between $\sim 0.8\ cm$ and $\sim 1.5\ cm$ (mean values), considering $4\ \%$ noise ($\sim 4mT$), having a standard deviation σ scaling from $0.4\ cm$, for 1 faulty sensor, to $\sigma \approx 0.1\ cm$ with 12. As regards current error against 0%-noise case, the range span from $\sim 1\%$ to $\sim 1.5\%$ at the highest noise level ($\sigma \approx 0.53\ \%$).

Right away (Fig 6.18-19) are reported the results for the *shot n. 39122*, for 1 and 7 faulty sensors. Results for other shots, for same sensor numbers, could be found in the appendix at B.4, as they present similar behaviours, and similar magnitudes.

Shot 39122 (1 sensor off)

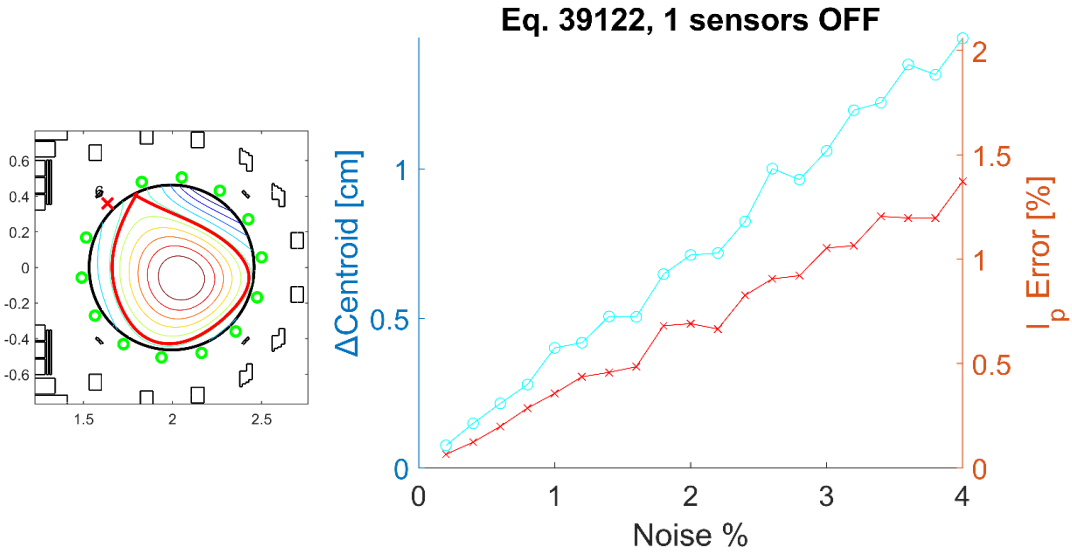

Fig. 6.18a: *Shot 39122*, 1 sensor off, best case, noise analysis

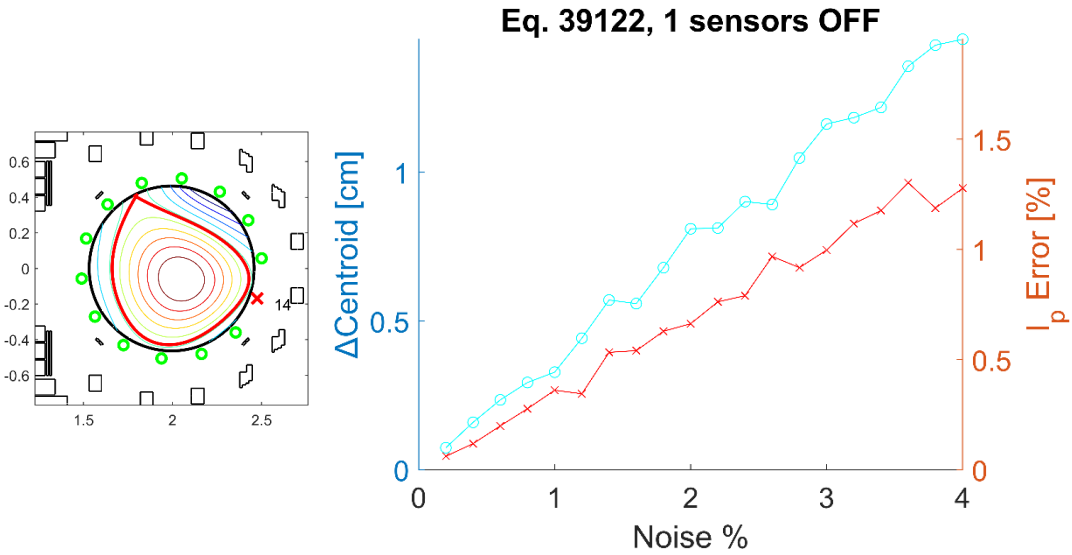

Fig. 6.18b: *Shot 39122*, 1 sensor off, worst case, noise analysis

Shot 39122 (7 sensors off)

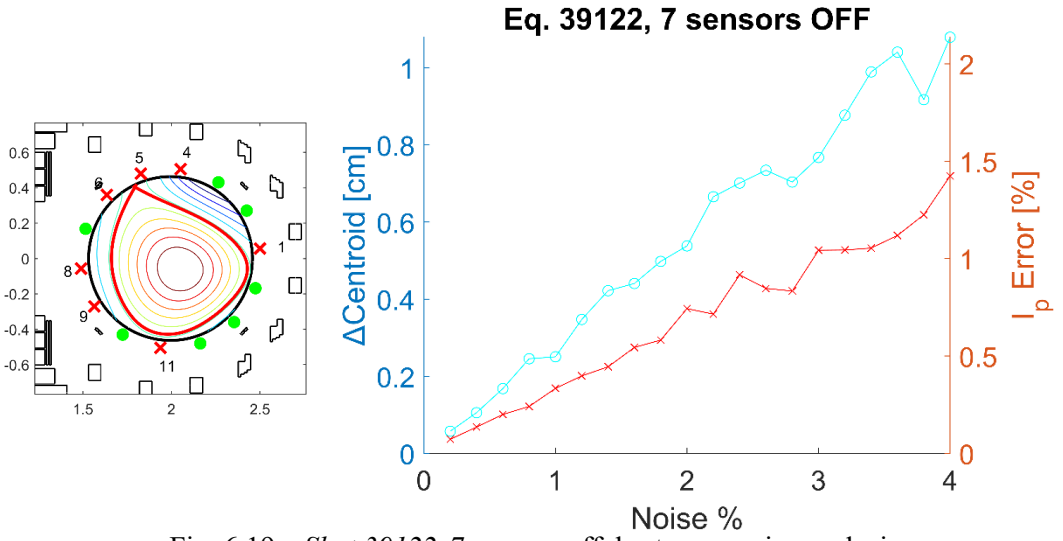

Fig. 6.19a: *Shot 39122*, 7 sensors off, best case, noise analysis

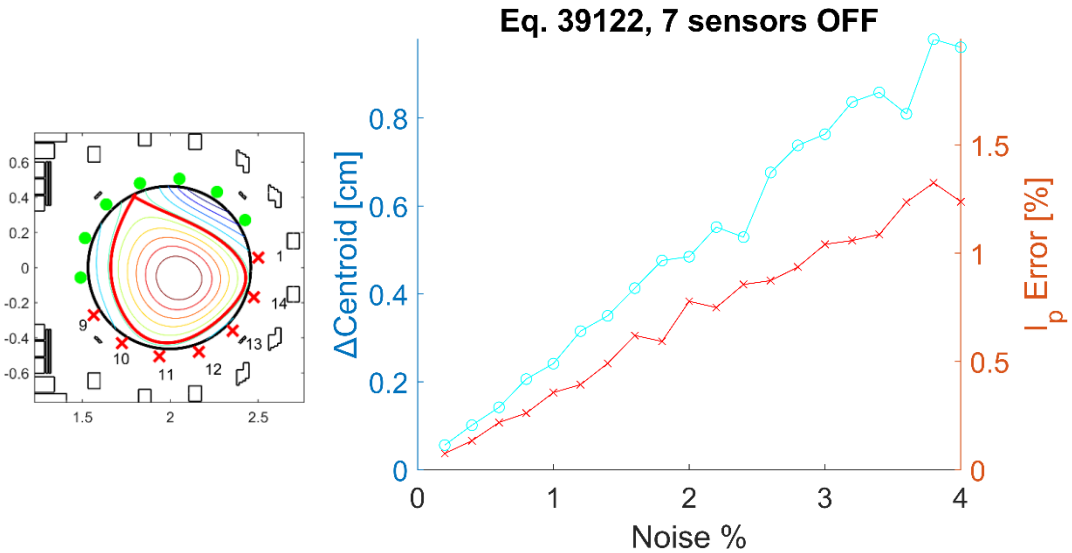

Fig. 6.19b: *Shot 39122*, 7 sensors off, worst case, noise analysis

Conclusions

The purpose of this work was to verify whether plasma parameters reconstruction could be sufficiently effective in condition of the fault of one or more sensors. All the possible failure configurations have been analysed to give a complete description of the scenario.

What emerged by the analysis is a strong equilibrium-dependent correlation between accuracies of reconstructed parameters and positions of the faulty sensors. The main equilibrium parameter that affects the moment computation is the position of the FRIDA equilibrium centroid with respect to the machine centre, meaning that losing sensors that are closer to the direction of FRIDA centroid with respect to the machine centre lead to a coarser reconstruction. This fact can be explained reminding that RFX-mod2 pick-up coils are placed along a circumference centred exactly in the machine centre, while plasma presents a current density distribution that is not centrosymmetric. Thus performing the moment computation by means of a set of measurements not uniformly distributed, could lead to higher errors. In fact, the worst configurations are exactly the most asymmetric ones. Conversely, symmetric configurations preserve some accuracy, thanks to compensations of sensors in opposite positions.

Another parameter that influences negatively the loss of a sensor in a determined area is the plasma-first-wall (PL-FW) distance. The smaller is this quantity, the worse would be the loss of a sensor in that region. This parameter relates to the previous one because, in a tokamak equilibrium, the plasma centroid is located in the opposite direction of the x-point with respect to the machine centre (as regards single null configurations) and in the same direction of limiter point for limiter plasmas. This translates in a smaller PL-FW distance in the direction of the plasma centroid with respect to the machine centre. Moreover, smaller PL-FW distance indicates a closeness between plasma and sensors, thus the presence of a higher current density near calculation points (i.e. higher magnetic field), makes them more sensitive. As regards the null point, the PL-FW is actually small, nevertheless we don’t observe severe errors in parameters reconstruction when turning off sensors in this area. This behaviour is due to the smaller intensity of the magnetic field in that region of space, de facto reducing the sensor’s contribution in the moment computation.

Another interesting correlation that has been found is that, having a higher number of faulty sensors, the plasma current error grows faster than correspondent centroid displacement. This behaviour has then been found also looking at error ranges in function of the number of faulty sensors. Focusing on the upper bound, i.e. the worst configurations for each number of faulty sensors, the error on

centroid position follows an almost linear behaviour, while plasma current error doesn't increase linearly.

Considering the lower bound, instead, could be confirmed how symmetrical sensor configurations could well reconstruct plasma parameters, even in the condition of high number of sensor failures.

As regards the noise analysis, plasma parameters showed a linear increase with respect to the noise level: centroid just displaces between $0.8\ cm$ and $1.5\ cm$ with $4\ \%$ noise (mean values, with $\sigma \approx 0.4\ cm$ for 1 faulty sensor till $\sigma \approx 0.1\ cm$ for configurations with 12 broken sensors), while current error span from $\sim 1\%$ to $\sim 1.5\%$ at the highest noise level ($\sigma \approx 0.53\ \%$). These values show how noise won't be the main constraint in the context of having a low number of working sensors. In fact, having too many inactive sensors, noise error results neglectable, thus the plasma parameters error is almost entirely attributable to the faults. Noise displacements, indeed, becomes relevant only when plasma parameters errors due to faulty sensors are lower than the noise displacement range, depending on the noise level.

To summarize, the computation of centroid position and plasma current by means of TSVD-optimized moment method, is preponderantly affected by the most asymmetric sensors configurations and the most inaccurate results are found when faults occur in the regions closer to reference centroid (i.e. reference direction), and smaller plasma-first-wall distance. For symmetric configurations, instead, the presence of noise could affect the quality of reconstruction, but, since the displacement is relatively small at a high noise percentage, it should not be considered as main constraint for practical applications.

Data obtained in this work could be then compared with real data that will be produced in RFX-mod2 for validation and/or verify, whether some of the sensors are unavailable, the order of magnitude of the accuracy in parameters reconstruction.

Since this analysis has availed only of the tangential component measured by magnetic field sensors, a possible extension of this work would be to involve the use of the B_n component, since the new RFX-mod2 pick-up coils are bi-axial. Then, the time domain could be introduced, deepening what could happen when the passive conductors contributions are present, or rapid plasma displacements would occur. In these cases, one should focus on whether the rapid local variation of the magnetic field may lead to trivial reconstructions, or whether the number of sensors would remain adequate for real-time performances.

Appendix

A. Characteristic angle of faulty sensors

The following procedure is meant to compute a direction towards which could be attributed the failure of the RFX-mod2 poloidal field sensors. Since the plasma does not display a prefect symmetry with respect to the machine centre, a suitable model is necessary to assess its displacement inside the vacuum chamber.

Evidence has shown that plasma parameters reconstruction, in the case of the loss of one or more sensors, finely depends on the positions that are not covered by magnetic measurements. A critical parameter that affects plasma parameters reconstruction in sensors failure conditions is the position of the FRIDA centroid reference, meaning that sensors in its direction have a higher impact if a failure would occur. Thus, a proper weighting metric has to be set up to account this fact.

A.1 Procedure sequence

Knowing the position of the reference centroid (from FRIDA code) and the machine centre (MC), an ellipse can be build considering these two points as its foci, being c the distance between these two ones.

Being c the focal distance and considering its length scale, the minor axis b is chosen properly and kept fixed at $4\,cm$. With this strategy, if an equilibrium presents a limit case of a centroid coinciding with the machine centre, the ellipse reduces to a circumference of radius b.

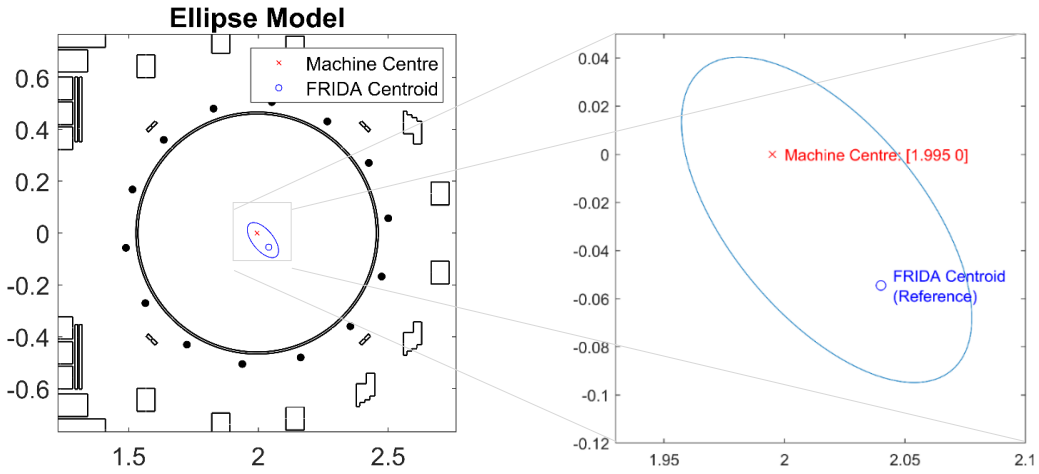

Fig. A.1: Ellipse model with highlighted foci

In the figures of this Appendix section is presented an example for the Shot n. 39122 equilibrium, with calculated centroid: $(r_c = 2.055, z_c = -0.04)$ and the failed sensors are: 2, 3, 7, 8, 12 from the Tab 4.3 numeration.

This set has been chosen to highlight the grouping method that will be presented further on.

The 14 poloidal field sensors of RFX-mod2, are located on a circumference centred on the machine centre, thus the points individuated by the interception of the perimeter of the ellipse and the straight line that connect each sensor with the machine centre can be easily calculated.

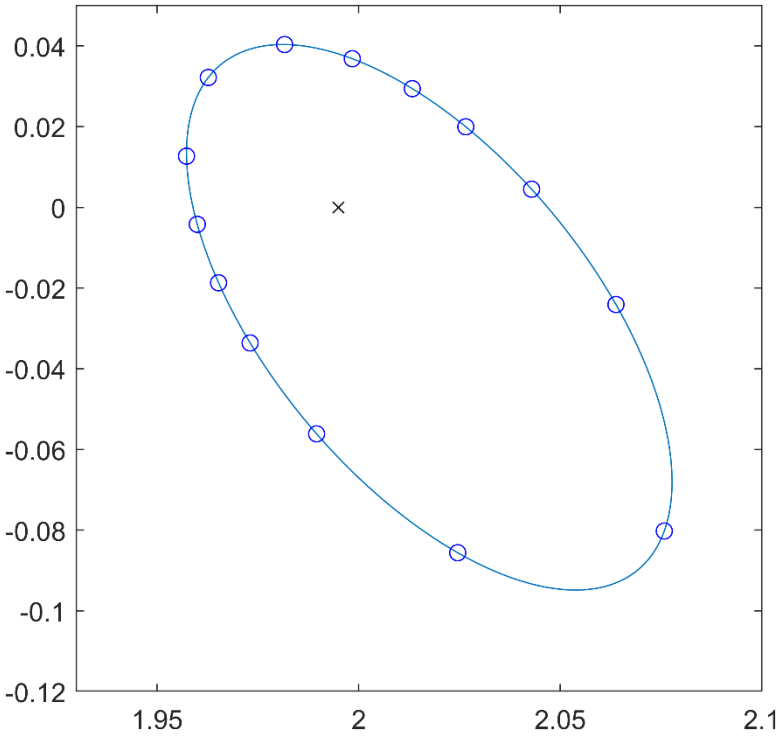

Fig. A.2 Crossing points of the MC-Sensors directions with the ellipse perimeter

The distance between each one of these points and the MC will play a key role in the determination of the characteristic angle, and it is clear that sensor that are located on the opposite side of the ellipse with respect to the MC will provide more weight in the final computation (since they have a longer distance towards the MC).

At this point, the set of faulty sensors is introduced. The scheme that lead to the characteristic angle starts with the arrangement of the sensors in groups of "nearby" sensors. If there are sensors that are, at most, three-steps consecutive, they are part of one group. This is done to emphasize the effect of losing sensors

that are close to each other, meanwhile the effect of distant failed sensors compensate in a certain way.

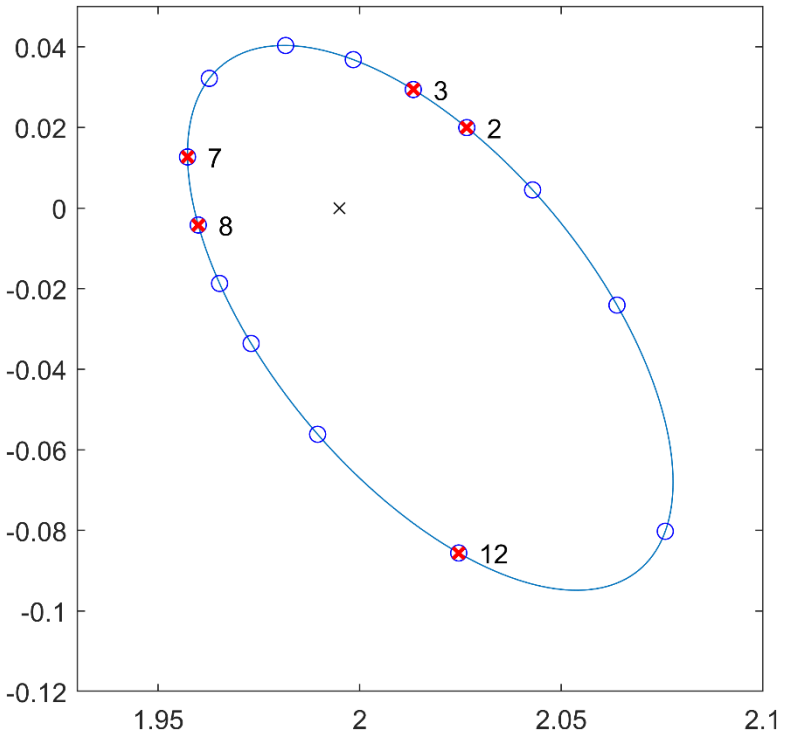

Fig. A.3: Perimeter points corresponding to the off-sensors (2,3,7,8,12)

Done this, the physical barycentre of those perimeter points of each group is found.

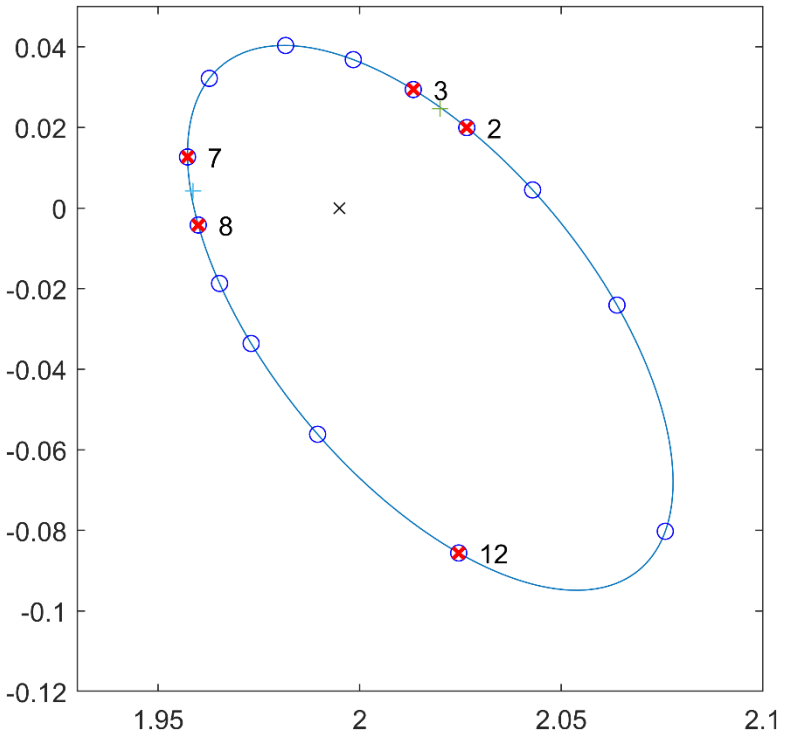

Fig. A.4: Group barycentres {2,3}, {7,8} are signed with '+'

The distances between group barycentres and isolated points with respect to the MC are then computed, minding that, to emphasize the effect of sensors failures in close positions, distances towards barycentres are multiplied by the number of sensors of their relative group.

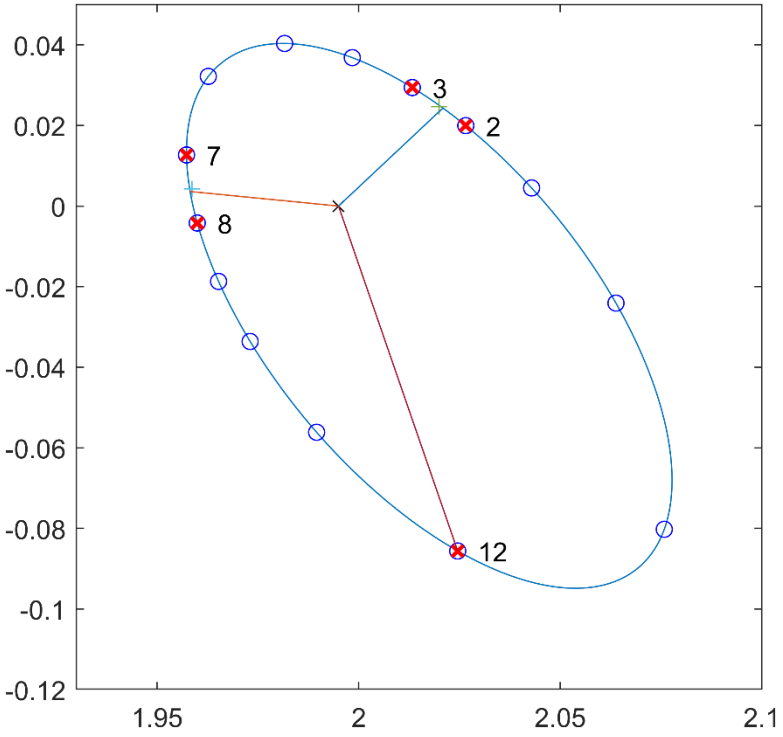

Fig. A.5: Distances of the calculated points with respect to the MC

Longest distance is taken, and, on its direction, all the other distances are projected. If the sum of all the projections is smaller than the longer distance, than, according to the reference system of Fig 6.1, the characteristic angle is the angle corresponding to the direction of longer distance itself, otherwise an addition of $\pm\pi$ is provided, depending on the quadrant.

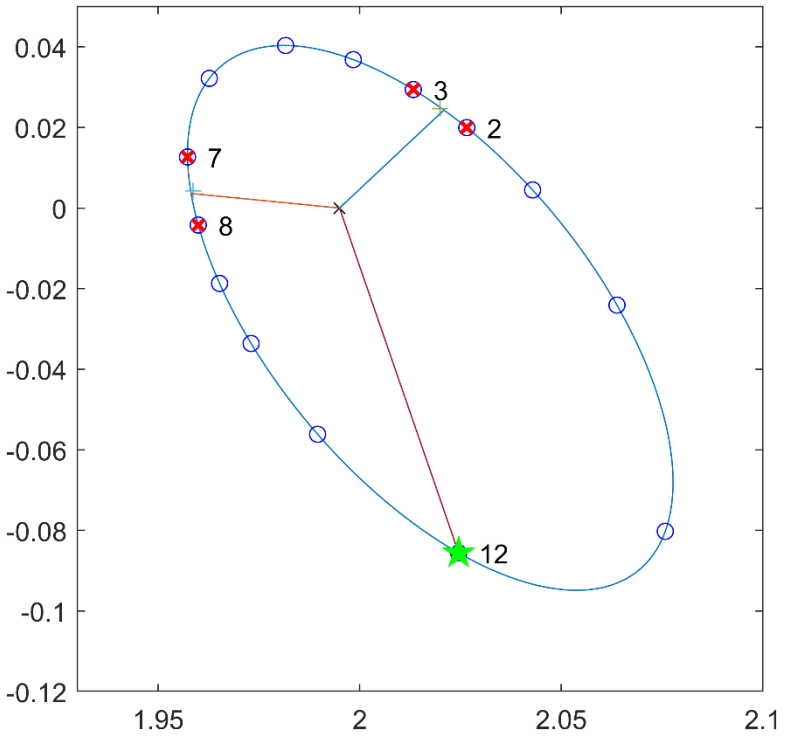

Fig. A.6: Marked with the star is the direction which corresponds the characteristic angle

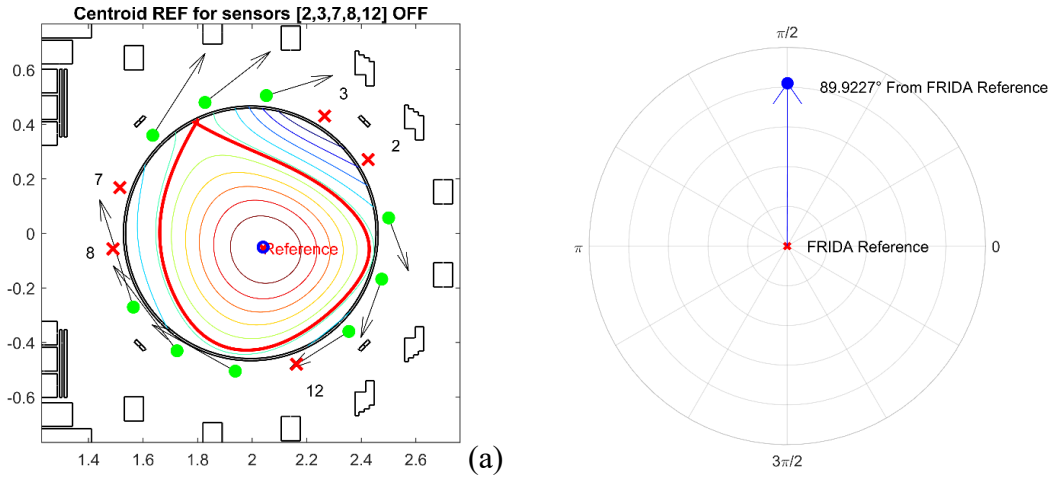

Fig. A.7 (a) Sensors turned off in the ellipse example with relative calculate centroid with the moments method, (b) angle of the calculated centroid with respect to the FRIDA reference

A.2 Code Listing (MATLAB)

A.2.1 Ellipse function

Inputs:

- rc, zc: FRIDA calculated centroid coordinates
- thc: FRIDA calculated centroid angle θ_c with respect to the MC
- ths: Sensor's angles $\theta_{s,n}$, $n = 1, \dots, 14$

Output

- ELL: Data structures with r, z coordinates of ellipse, θ_e of perimeter points with respect to the MC and coordinates r, z of perimeter points in the direction MC-sensors

```
function [ELL] = fun_weightEll(rc, zc, thc, ths)
    % Build an ellipse with foci: Machine Centre MC and FRIDA
Centroid
    % maintain constant b = 4 cm

    % FIND ELLIPSE
    xc = (rc+1.995)/2;
    yc = (zc)/2;

    c = norm([abs(rc-1.995) abs(zc)]);
    b = .04;
    a = sqrt(c^2+b^2);
    t = linspace(0, 2 * pi, 200);        % Absolute angle
parameter
    X = a * cos(t);
    Y = b * sin(t);
    r = xc + X * cos(thc) - Y * sin(thc);
    z = yc + X * sin(thc) + Y * cos(thc);

    % VALUES ON SENSOR DIRECTION
       % Compute angle between perimeter and machine centre
    for i = 1:length(r)
        th(i) = fun_RefCM([r(i) z(i)], [1.995 0]);
    end

    rs = zeros(1,14);
    zs = zeros(1,14);
    % Compare th with sensor angle and search for 0 crossing
minumum difference
    for k = 1:length(ths)
        tmp = abs(th-ths(k));
        mmp = min(abs(th-ths(k)));
        l = find(tmp==mmp);
        rs(k) = r(l);
        zs(k) = z(l);
    end

    ELL.R = r;
    ELL.Z = z;
    ELL.rs = rs;
    ELL.zs = zs;
    ELL.th = th;
end
```

A.2.2 Characteristic angle function

Inputs:

- ind_sens: Row vector of broken sensors' indices
- ELL: Data structure as defined in A.2.1
- ths: Sensor's angles $\theta_{s,n}$, $n = 1, \dots, 14$

Output

- the: Characteristic angle of broken sensors

```
function [the] = fun_thetaEquiv(ind_sens, ELL, ths)

% Group sensors that are closer than 3 units so to calculate
centroid of
% ellipse points in their directions


c = nchoosek(ind_sens, 2);
diff = abs(c(:,1)-c(:,2));
% Must account for the closeness of sensors 1 and 14
% if sensor's difference is greater than 11, then we are in that
range
k_11 = diff >= 11;
diff(find(k_11)) = 14 - diff(find(k_11));

k_3 = diff <= 3;
c_3 = c(find(k_3),:);
ind_groups = 0;
groups = {};

e_3 = unique(sort(c_3))';
if isempty(e_3) == 0
    ind_groups = 1;
    g = [];
    g = [g; e_3(1)];
    groups{ind_groups} = g;
    for i = 1:length(e_3)-1
        if e_3(i+1)-e_3(i) <= 3
            g = [g; e_3(i+1)];
            groups{ind_groups} = g;
        else
            g = [];
            g = [g; e_3(i+1)];
            ind_groups = ind_groups + 1;
            groups{ind_groups} = g;
        end
    end

    % reconnect groups carrying 1-14
gg = [];
for i=1:length(groups)
    gg = [gg; groups{i}];
end
mm = min(gg);
MM = max(gg);
if ((mm <= 3) && (MM > 11))
    if 14-(MM-mm)<=3
        for i=1:length(groups)
```

```
            if any(ismember(groups{i}, mm))
                rec_m = i;
            end
            if any(ismember(groups{i}, MM))
                rec_M = i;
            end
        end
        if rec_m ~= rec_M
            groups{rec_m} = [groups{rec_m}; groups{rec_M}]; %
reconnect close sensors of different indices
            groups(rec_M) = [];
        end
    end
end

% Find  groups centroid
ng = length(groups);
bg = zeros(ng,3);
thd_all = [];
for i = 1:ng
    bg(i,1) = sum(ELL.rs(groups{i}))/length(groups{i});
    bg(i,2) = sum(ELL.zs(groups{i}))/length(groups{i});
    bg(i,3) = fun_RefCM([bg(i,1) bg(i,2)], [1.995 0]);

    % multilply by number of sensor in group to enhance their
contribute
    thd_all(i,1) = norm([abs(bg(i,1)-1.995)
abs(bg(i,2))])*length(groups{i});
    thd_all(i,2) = bg(i,3);
    thd_all(i,3) = i;

end
end

ng = length(groups);

% Now consider isolated sensors and the centroids of found groups
% These are placed for sure at an angular distance >75° (3
sensors)

ce = unique(sort(c));   % isolated sensors
e_n3 = [];
for i=1:length(ce)
    if isempty(e_3) == 1
        if isempty(ismember(e_3, ce(i)))
            e_n3 = [e_n3 ce(i)];
        end
    else
        if ismember(e_3, ce(i)) == 0
            e_n3 = [e_n3 ce(i)];
        end
    end
end
th_iso = ths(e_n3);

for i=1:length(e_n3)
   thd_all(ng+i,1) = norm([abs(ELL.rs(e_n3(i))-1.995)
abs(ELL.zs(e_n3(i)))]);
   thd_all(ng+i,2) = th_iso(i);
   thd_all(ng+i,3) = e_n3(i);
end
```

```
% Along these angular directions compute the CM->Ellipse distance
and evaluate
% the major one

majdir = max(thd_all(:,1));
i_maj = find(thd_all(:,1)==majdir);

% Consider the direction correspondent to the major distance, so
% calculate the sum of the projections of the other distances
along this
% direction

eq_dir = thd_all(i_maj,2);
% if i_maj>ng
%    i_maj = thd_all(i_maj,3);
% end
other_dir = thd_all(find(thd_all(:,1)~=majdir),2);
proj_dist = zeros(length(other_dir),1);

% Calcolate projections on main direction
for i = 1:length(other_dir)
    if eq_dir < pi/2
        if (abs(other_dir(i)-eq_dir) < pi/2 && other_dir(i)<pi) ||
(other_dir(i)>=eq_dir+3*pi/2)
            if other_dir(i)>=eq_dir+3*pi/2
                proj_dist(i) = thd_all(i,1)*cos(abs(eq_dir+(2*pi-
other_dir(i))));
            else
                proj_dist(i) = thd_all(i,1)*cos(abs(eq_dir-
other_dir(i)));
            end
        else
            proj_dist(i) = -thd_all(i,1)*cos(abs(eq_dir+pi-
other_dir(i)));
        end
    elseif eq_dir >= pi/2 && eq_dir < pi
        if abs(other_dir(i)-eq_dir) < pi/2
            proj_dist(i) = thd_all(i,1)*cos(abs(eq_dir-
other_dir(i)));
        else
            if other_dir(i)>=eq_dir+pi/2
                proj_dist(i) = -thd_all(i,1)*cos(abs(eq_dir+pi-
other_dir(i)));
            else
                proj_dist(i) = -thd_all(i,1)*cos(abs(pi-
eq_dir+other_dir(i)));
            end
        end
    elseif eq_dir >= pi && eq_dir <= 3*pi/2
        if abs(other_dir(i)-eq_dir) < pi/2
            proj_dist(i) = thd_all(i,1)*cos(abs(eq_dir-
other_dir(i)));
        else
            if other_dir(i)>=eq_dir+pi/2
                proj_dist(i) = -thd_all(i,1)*cos(abs(eq_dir-
pi+(2*pi-other_dir(i))));
            else
                proj_dist(i) = -thd_all(i,1)*cos(abs(eq_dir-pi-
other_dir(i)));
            end
```

```
        end
    elseif eq_dir >= 3*pi/2 && eq_dir < 2*pi
        if (abs(other_dir(i)-eq_dir) < pi/2 && other_dir(i)>pi) ||
(other_dir(i)<=eq_dir-3*pi/2)
            if other_dir(i)<=eq_dir-3*pi/2
                proj_dist(i) = thd_all(i,1)*cos(abs(2*pi-
eq_dir+other_dir(i)));
            else
                proj_dist(i) = thd_all(i,1)*cos(abs(eq_dir-
other_dir(i)));
            end
        else
            proj_dist(i) = -thd_all(i,1)*cos(abs(eq_dir-pi-
other_dir(i)));
        end
    end
end

sum_proj = sum(proj_dist);

% compare this sum with the major distance calculated before and
depending
% on the result chose properly in which direction consider the
characteristic
% angle

if abs(sum_proj)>majdir % assume that, if equals, characteristic
angle is the
% one of major distance
    if eq_dir>=0 && eq_dir<pi
        the = eq_dir+pi;
    else
        the = eq_dir-pi;
    end
else
    the = eq_dir;
end


end
```

B Plasma Parameters reconstruction results

B.1 Angular dependent results

Shot 39122

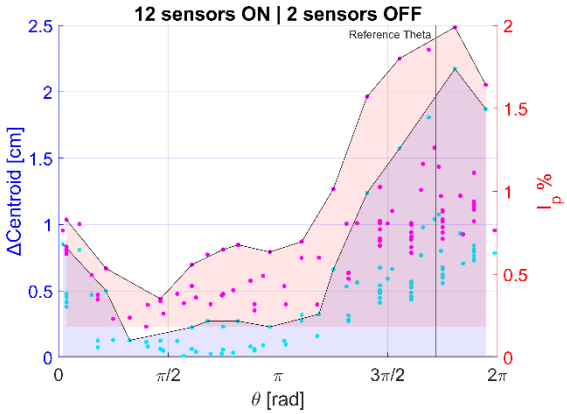

Fig. B.1a: *Shot 39122* – 2 sensors off

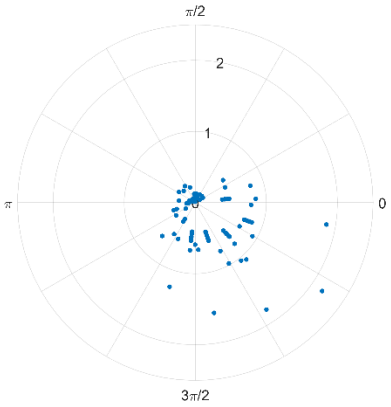

Fig B.1b: *Shot 39122* – 2 sensors OFF (polar plot): Centroid distance from reference

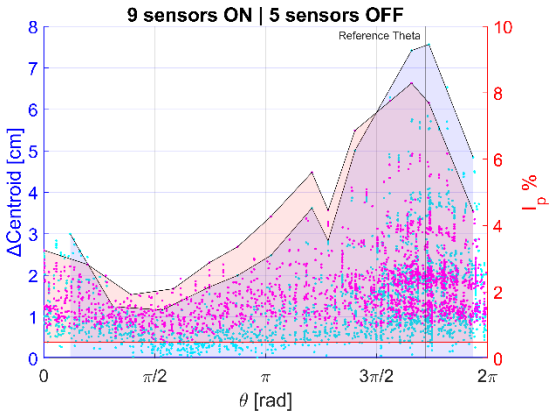

Fig. B.1c: *Shot 39122* – 5 sensors off

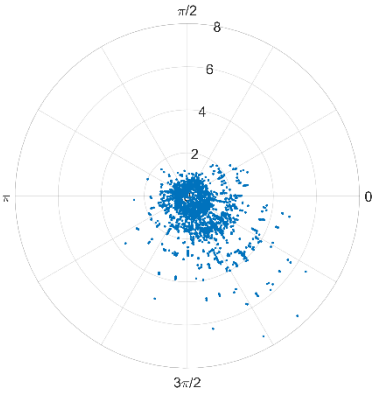

Fig B.1d: *Shot 39122* – 5 sensors OFF (polar plot): Centroid distance from reference

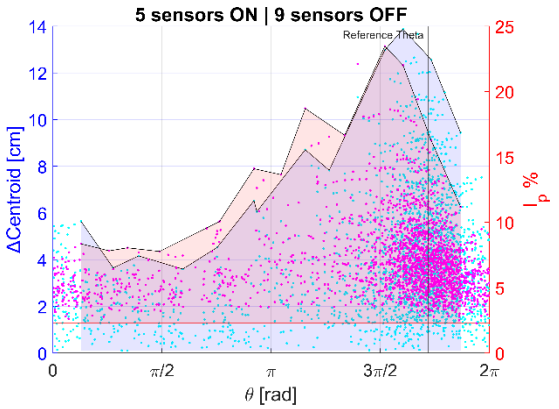

Fig. B.1e: *Shot 39122* – 9 sensors off

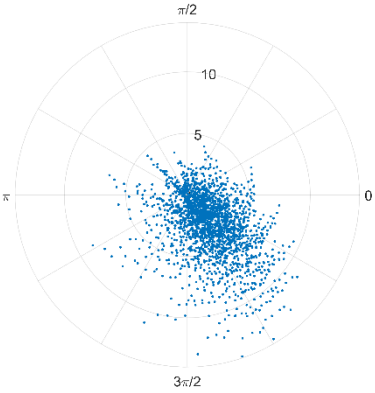

Fig B.1f: *Shot 39122* – 9 sensors OFF (polar plot): Centroid distance from reference

Shot 36922

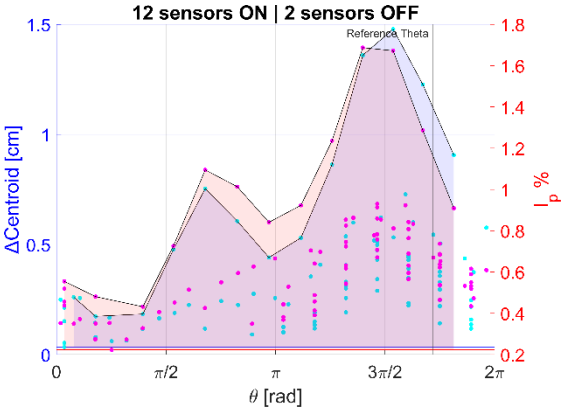

Fig. B.2a: *Shot 36922* – 2 sensos off

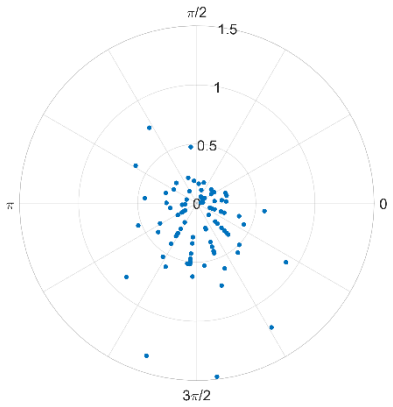

Fig B.2b: *Shot 36922* – 2 sensors off (polar plot): Centroid distance from reference

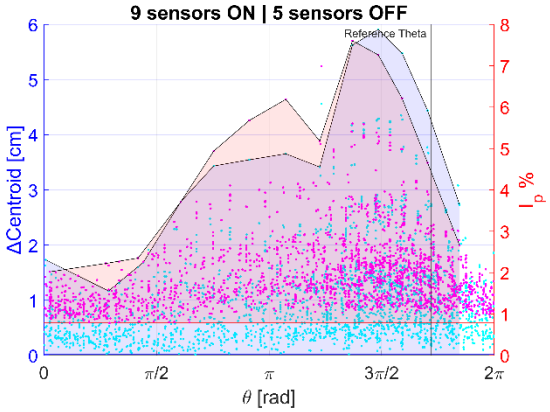

Fig. B.2c: *Shot 36922* – 5 sensors off

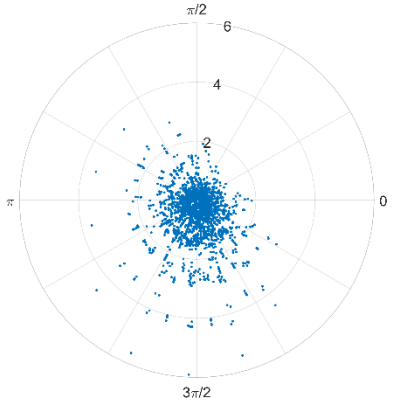

Fig B.2d: *Shot 36922* – 5 sensors OFF (polar plot): Centroid distance from reference

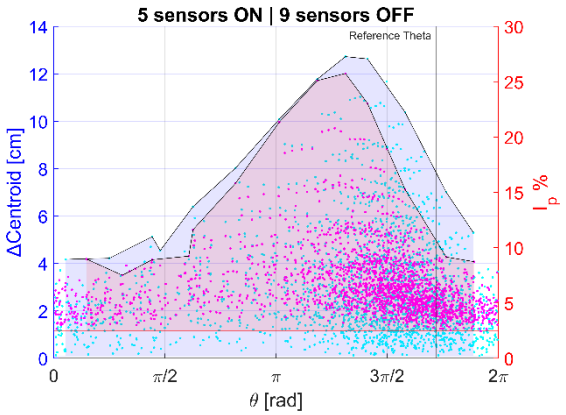

Fig. B.2e: *Shot 36922* – 9 sensors off

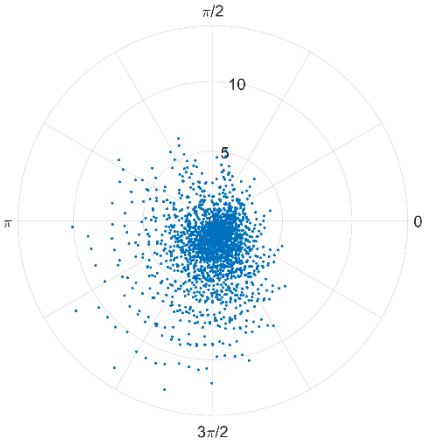

Fig B.2f: *Shot 36922* – 9 sensors OFF (polar plot): Centroid distance from reference

Shot 37829

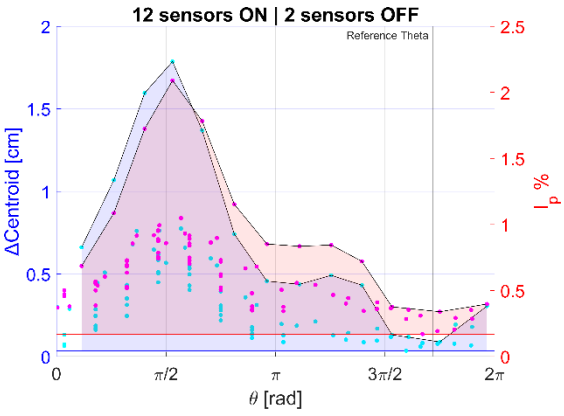

Fig. B.3a: *Shot 37829* – 2 sensors off

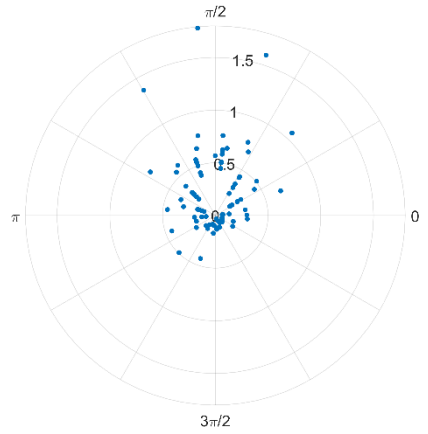

Fig B.3b: *Shot 37829* – 2 sensors off (polar plot)_ Centroid distance from reference

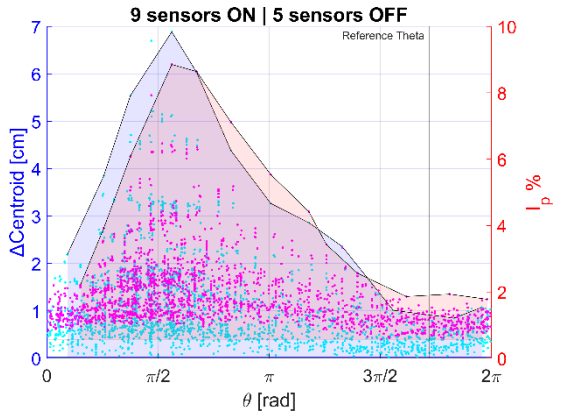

Fig. B.3c: *Shot 37829* – 5 sensors off

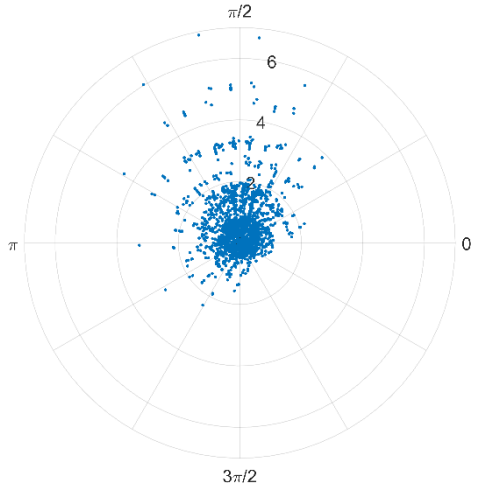

Fig B.3d: *Shot 37829* – 5 sensors OFF (polar plot): Centroid distance from reference

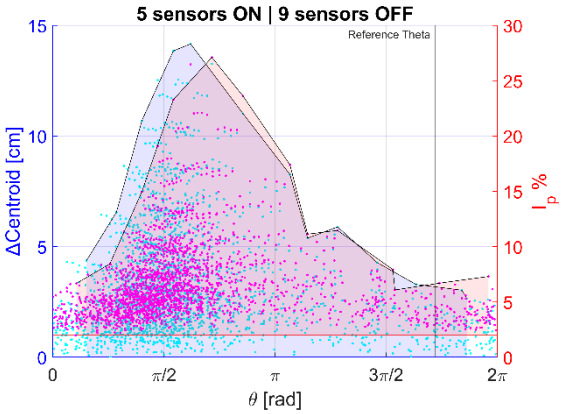

Fig. B.3e: *Shot 37829* – 9 sensors off

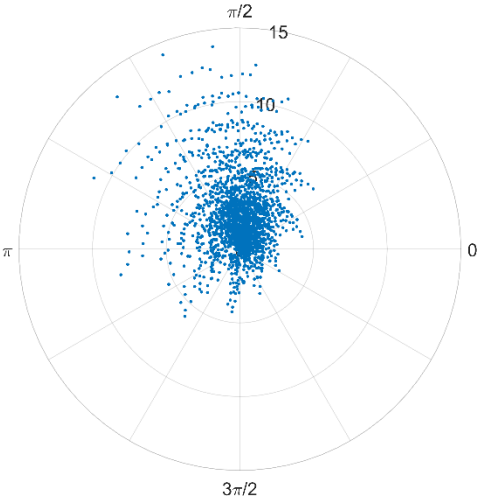

Fig B.3f: *Shot 37829* – 9 sensors OFF (polar plot): Centroid distance from reference

Shot DEMO-like δ_L

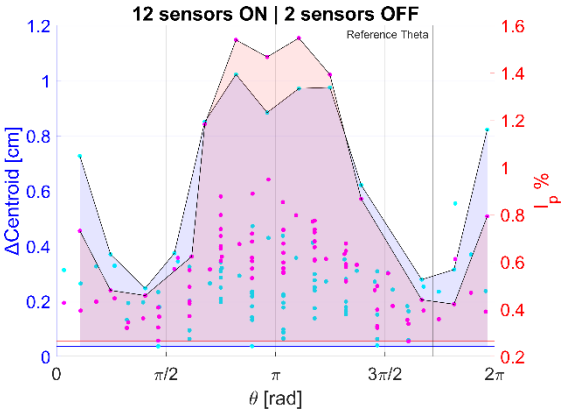

Fig. B.4a: *Shot* δ_L – 2 sensors off

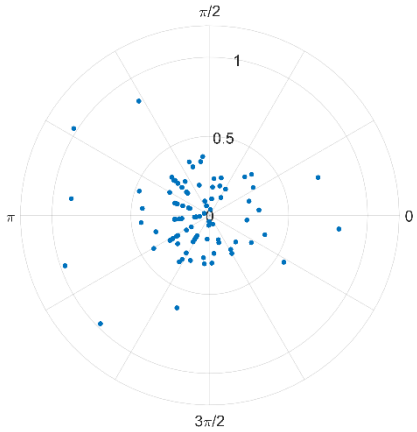

Fig B.4b: *Shot* δ_L – 2 sensors off (polar plot): Centroid distance from reference

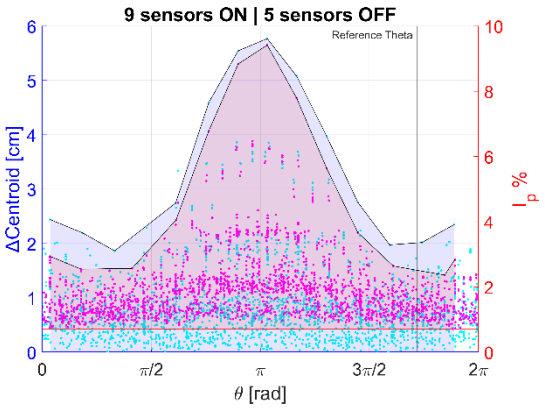

Fig. B.4c: *Shot* δ_L – 5 sensors off

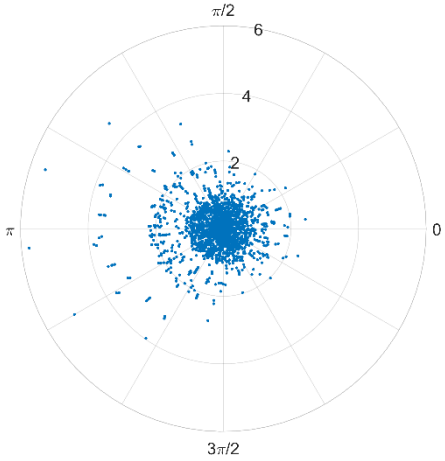

Fig B.4d: *Shot* δ_L – 5 sensors off (polar plot): Centroid distance from reference

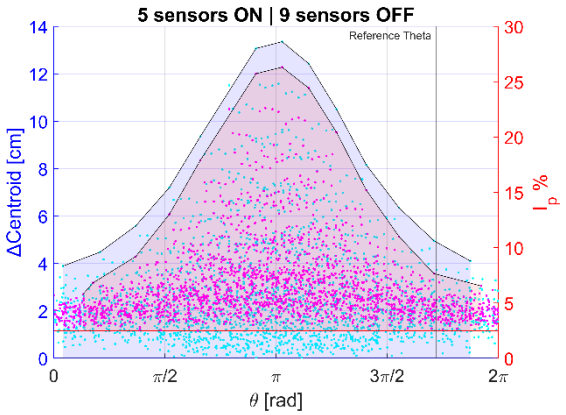

Fig. B.4e: *Shot* δ_L – 9 sensors off

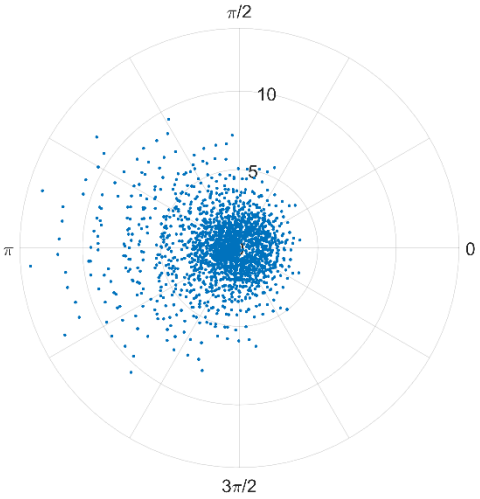

Fig B.4f: *Shot* δ_L – 9 sensors OFF (polar plot): Centroid distance from reference

Shot NT_L

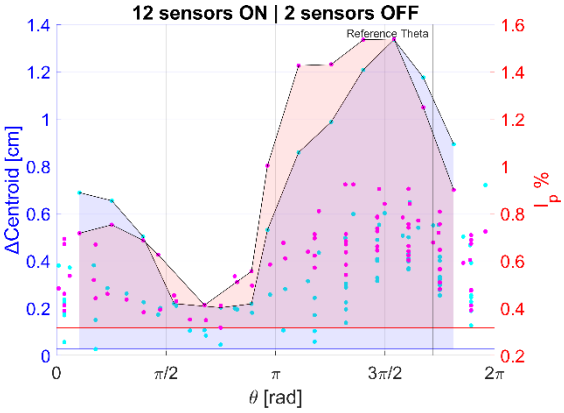

Fig. B.5a: *Shot NT_L* – 2 sensors off

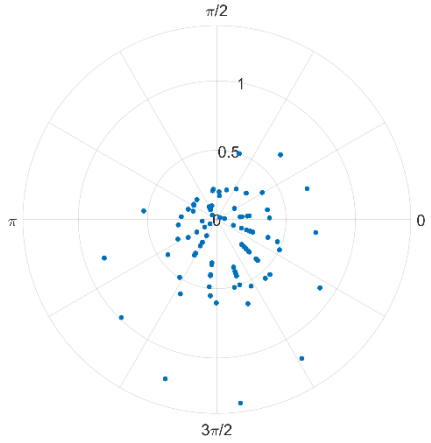

Fig B.5b: *Shot NT_L* – 2 sensors off (polar plot): Centroid distance from reference

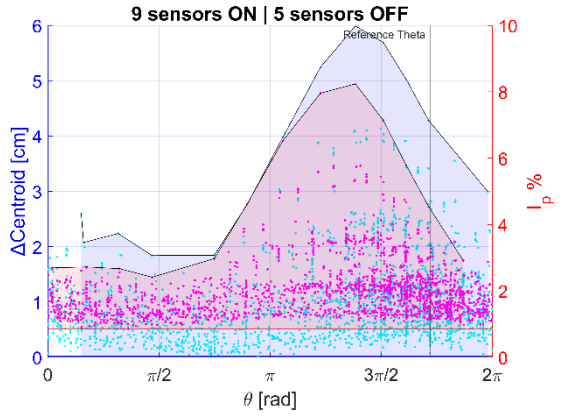

Fig. B.5c: *Shot NT_L* – 5 sensors off

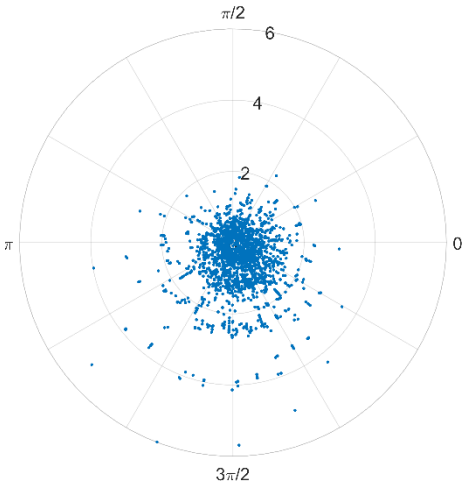

Fig B.5d: *Shot NT_L* – 5 sensors off (polar plot): Centroid distance from reference

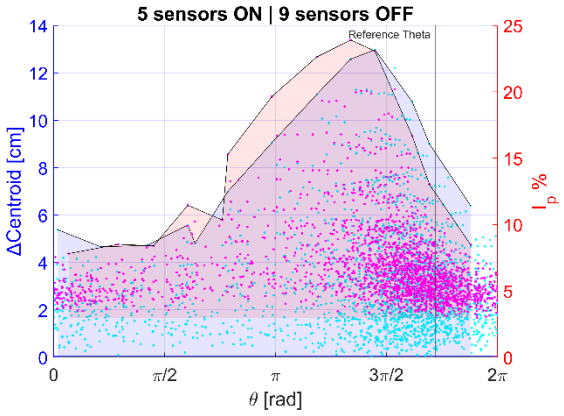

Fig. B.5e: *Shot NT_L* – 9 sensors off

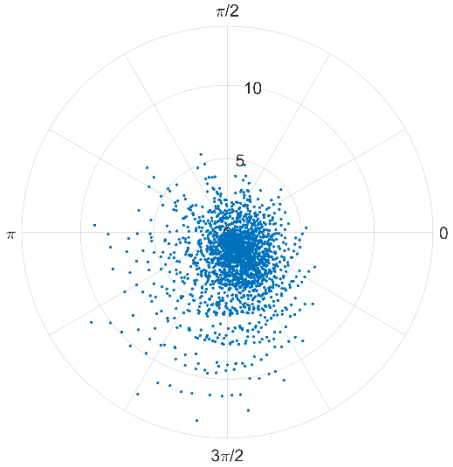

Fig B.5f: *Shot NT_L* – 9 sensors off (polar plot): Centroid distance from reference

B.2 Configuration's overview

Shot 39122

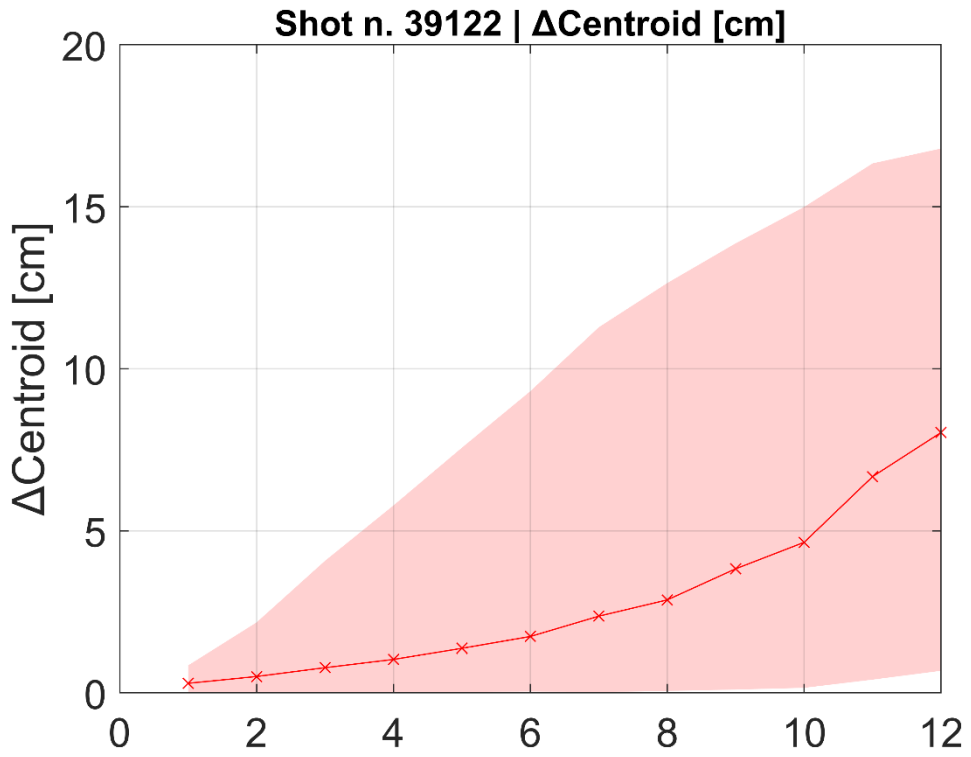

Fig. B.6a: *Shot 39122*: **Δ**Centroid (range plot vs. n. of faulty sensors)

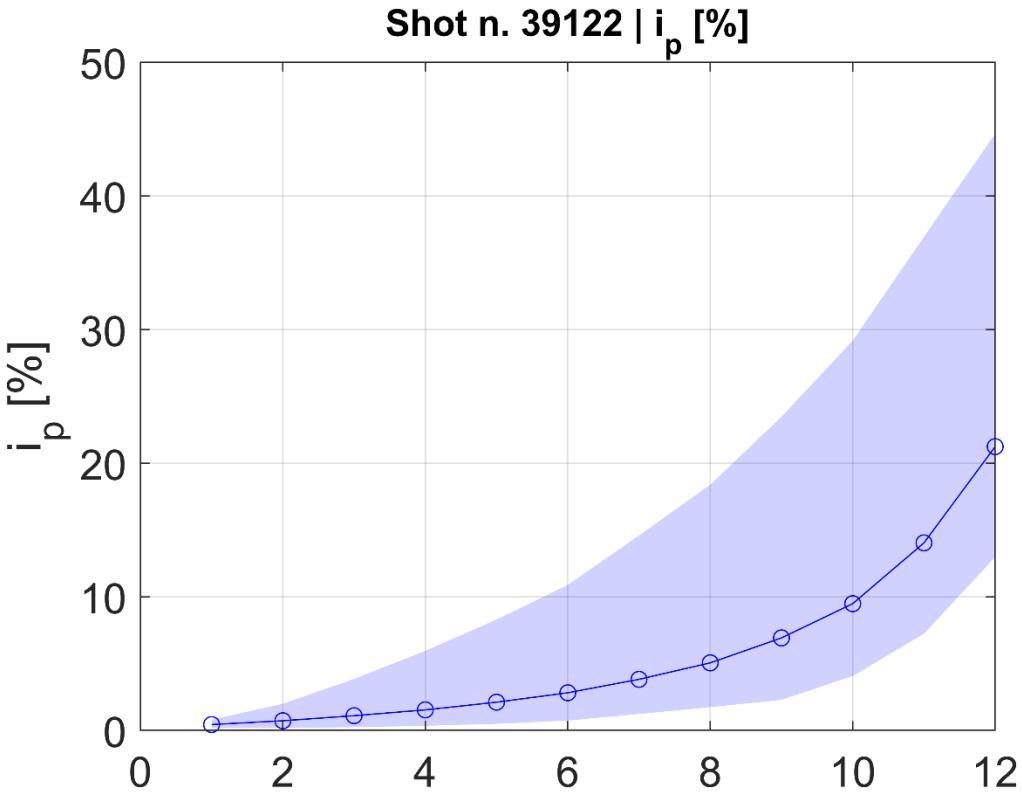

Fig. B.6b: *Shot 39122*: $\boldsymbol{I_p}$ error (range plot vs. n. of faulty sensors)

Shot 36922

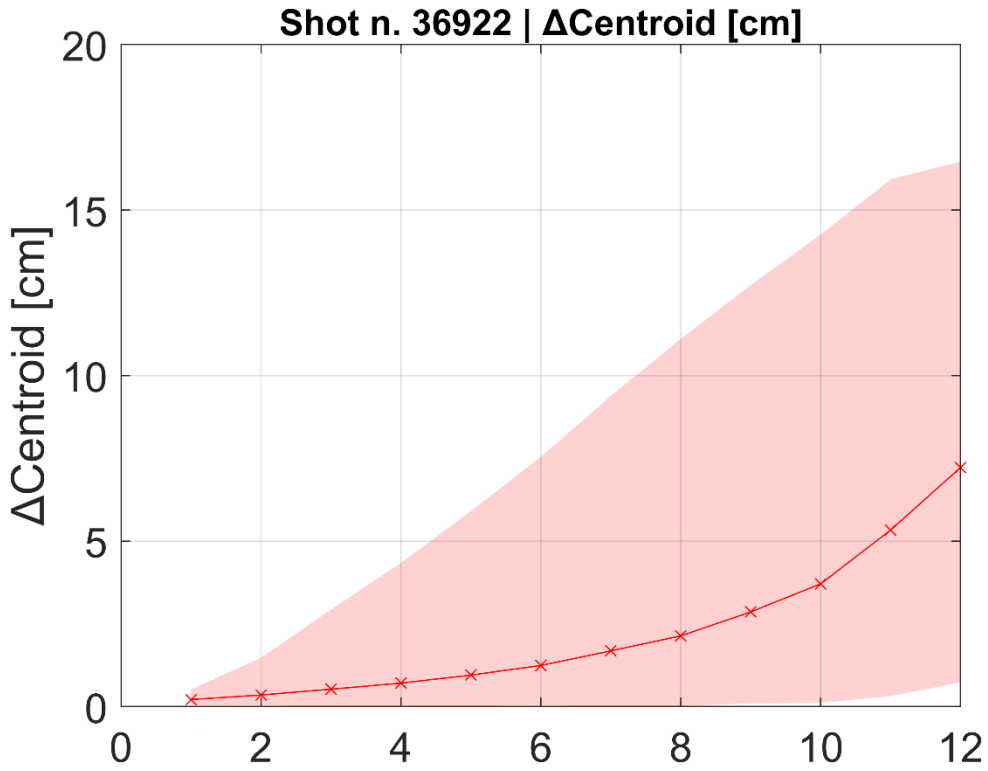

Fig. B.7a: *Shot 36922*: **Δ**Centroid (range plot vs. n. of faulty sensors)

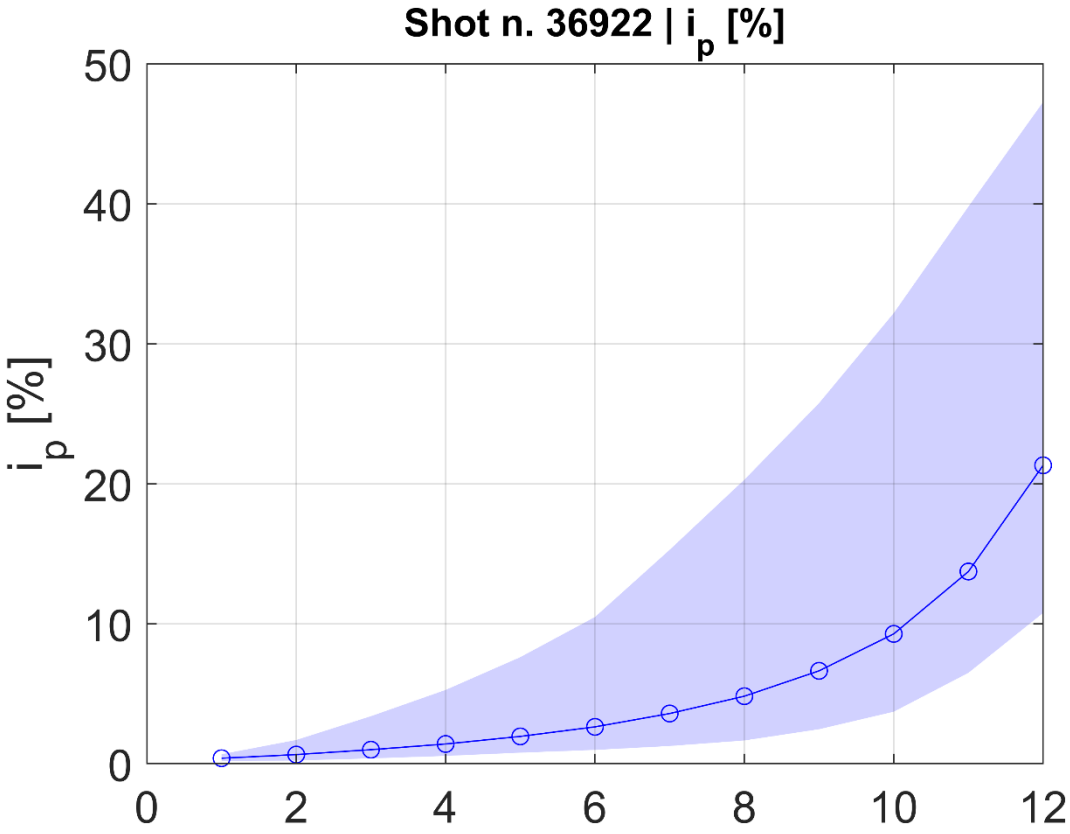

Fig. B.7b: *Shot 36922*: $\boldsymbol{I_p}$ error (range plot vs. n. of faulty sensors)

Shot 37829

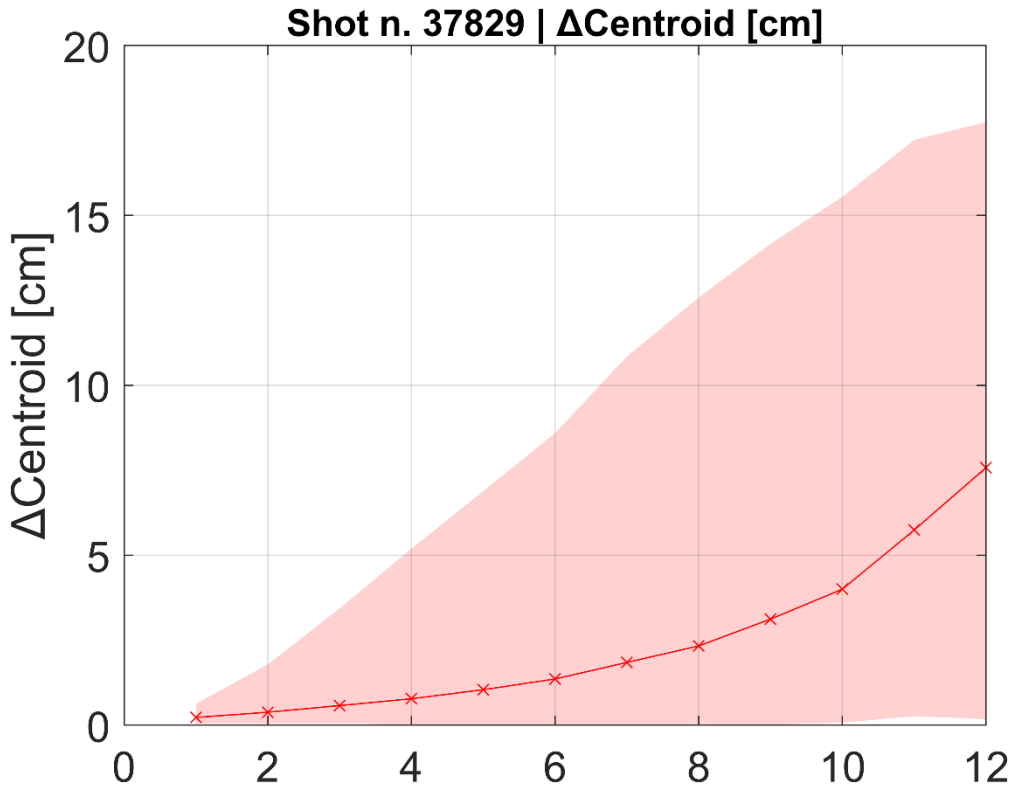

Fig. B.8a: *Shot 37829*: **Δ**Centroid (range plot vs. n. of faulty sensors)

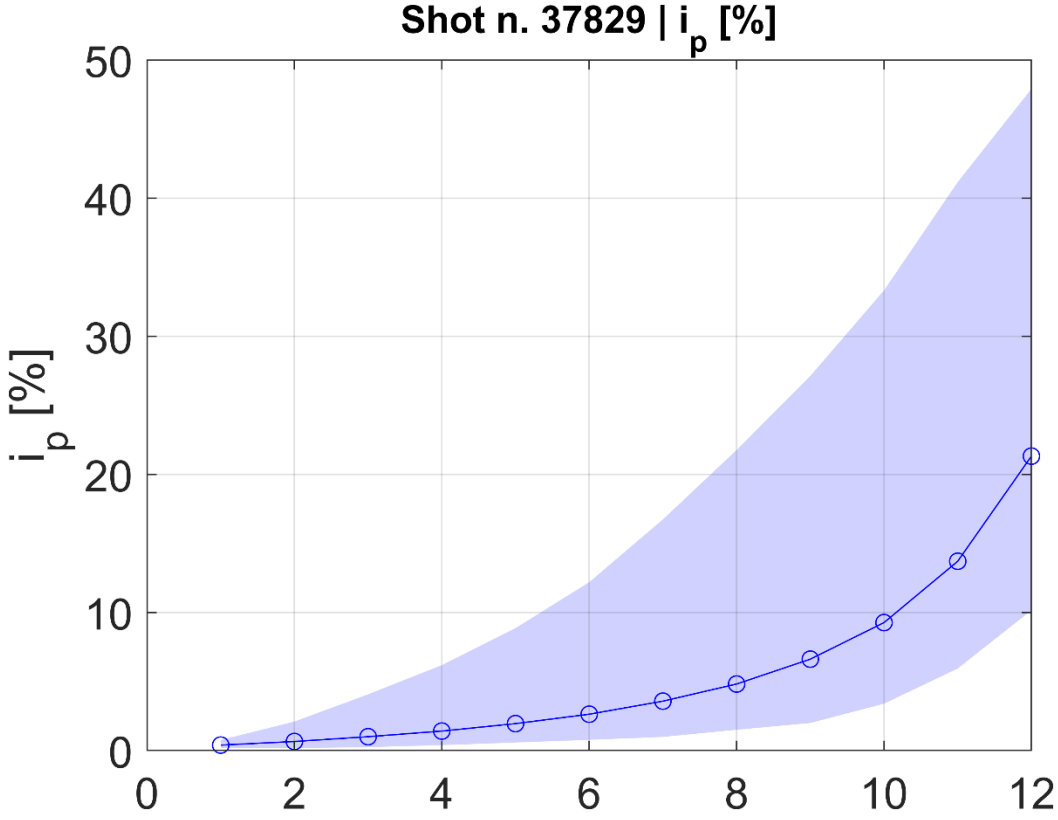

Fig. B.8b: *Shot 37829*: $\boldsymbol{I_p}$ error (range plot vs. n. of faulty sensors)

Shot DEMO-like δ_L

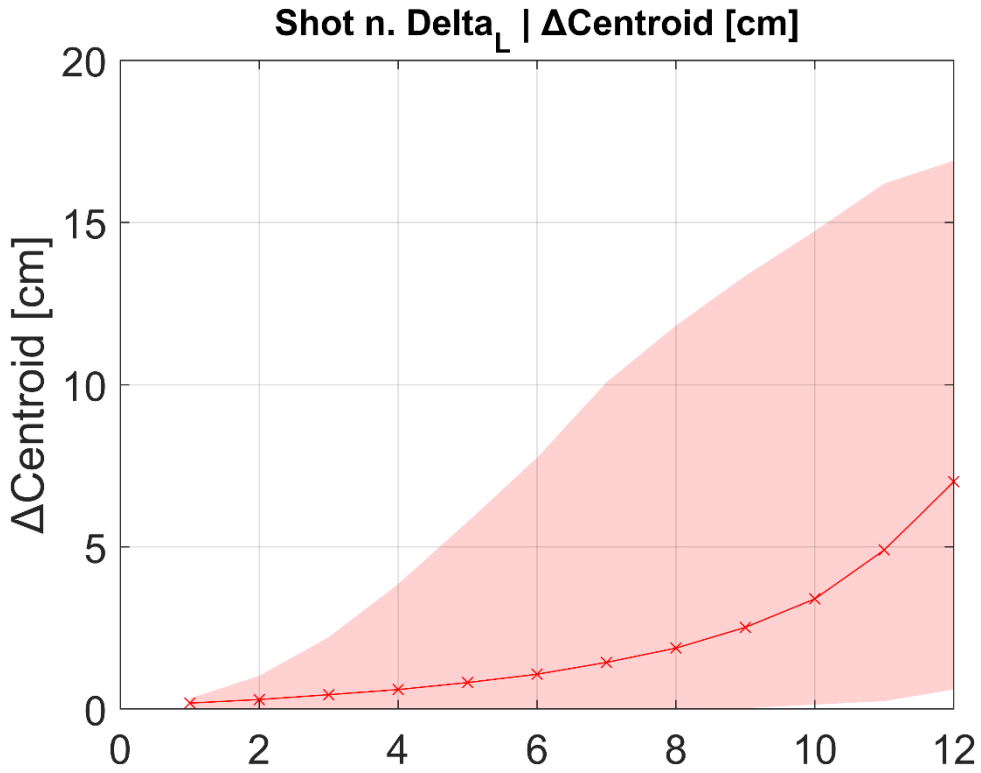

Fig. B.9a: *Shot* δ_L: **Δ**Centroid (range plot vs. n. of faulty sensors)

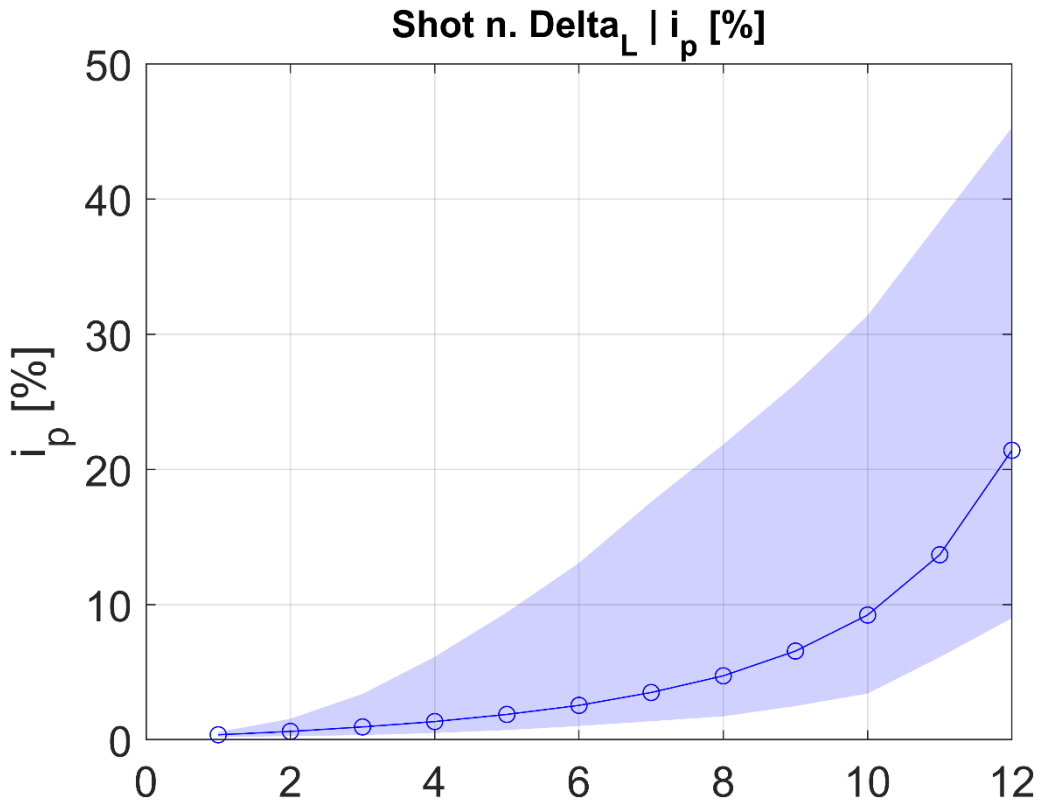

Fig. B.9b: *Shot* δ_L: $\boldsymbol{I_p}$ error (range plot vs. n. of faulty sensors)

Shot NT_L

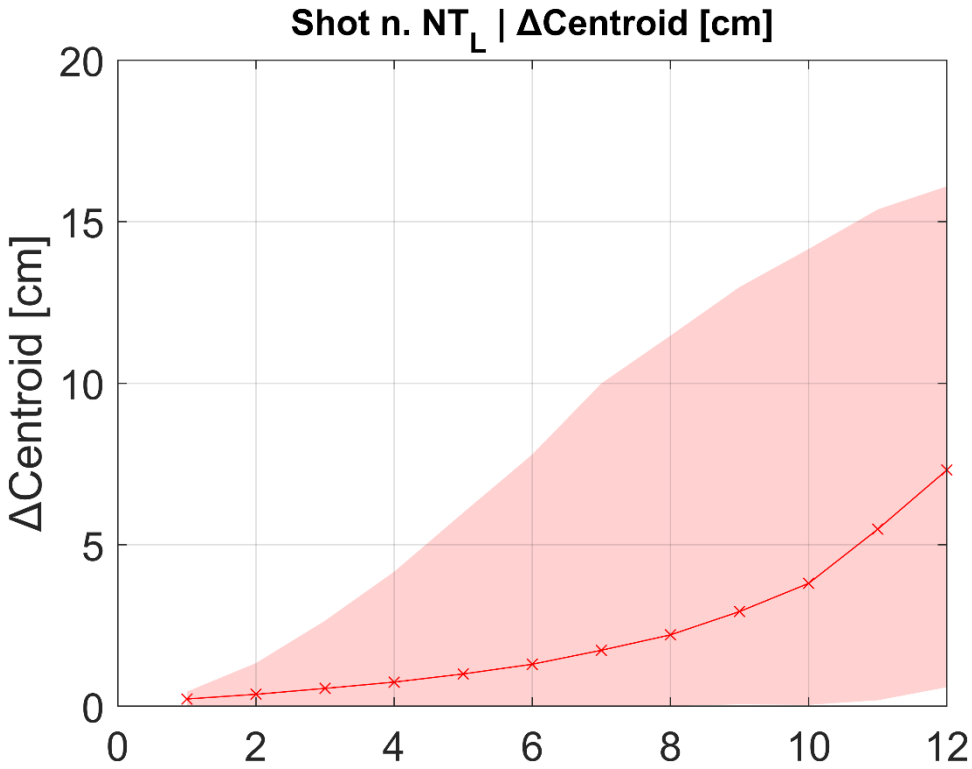

Fig. B.10a: *Shot NT_L*: **Δ**Centroid (range plot vs. n. of faulty sensors)

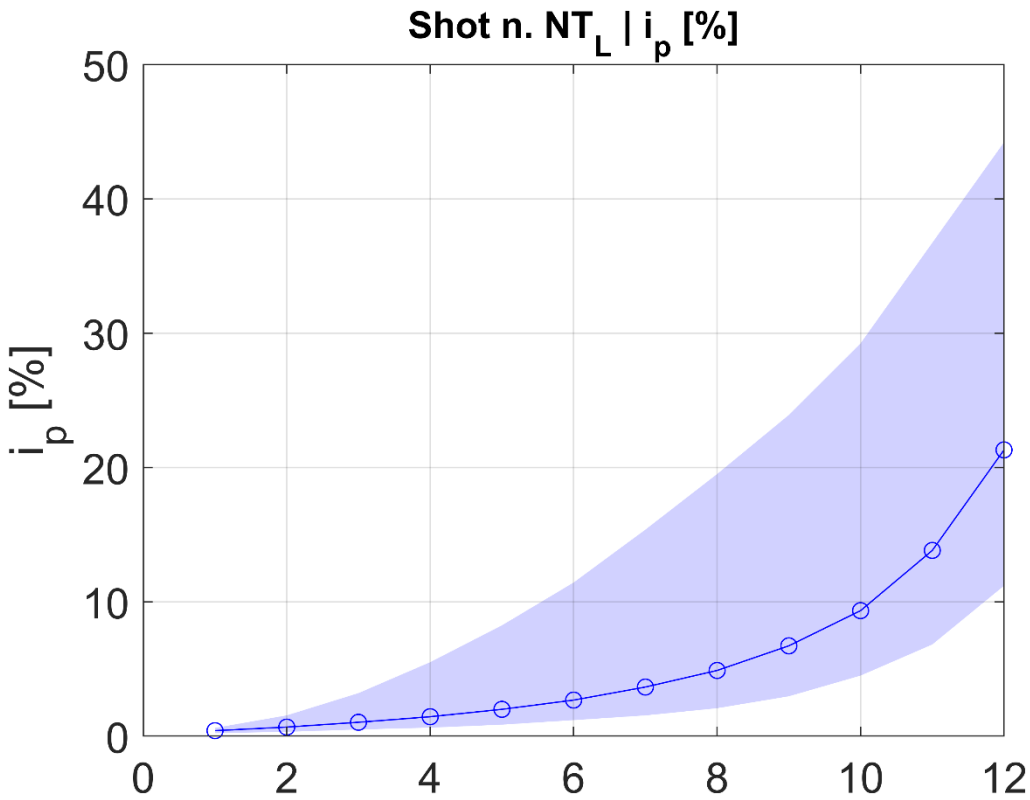

Fig. B.10b: *Shot NT_L*: $\boldsymbol{I_p}$ error (range plot vs. n. of faulty sensors)

Shot 39122

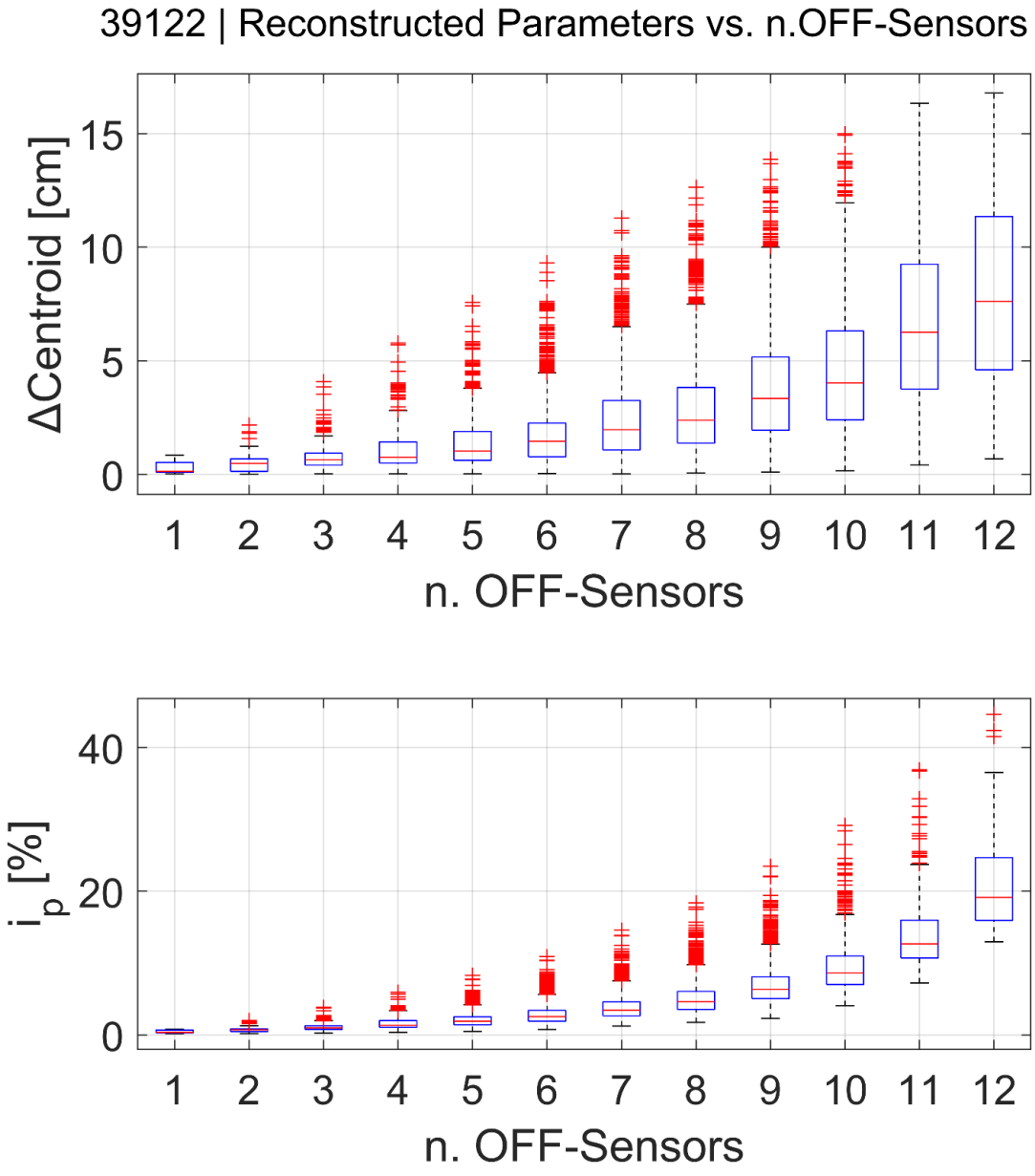

Fig. B.11: *Shot 39122*: Box-plot

Shot 36922

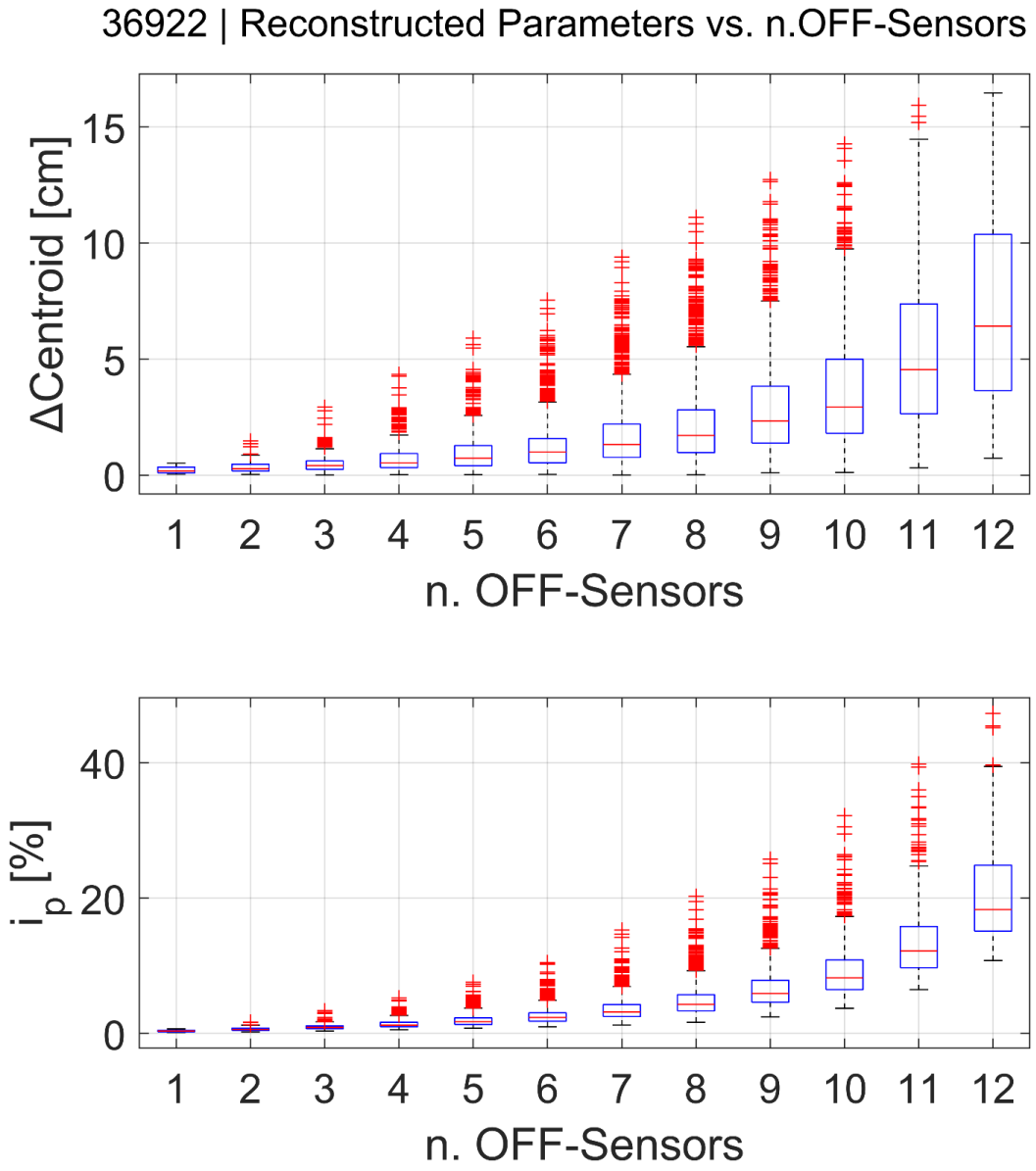

Fig. B.12: *Shot 36922*: Box-plot

Shot 37829

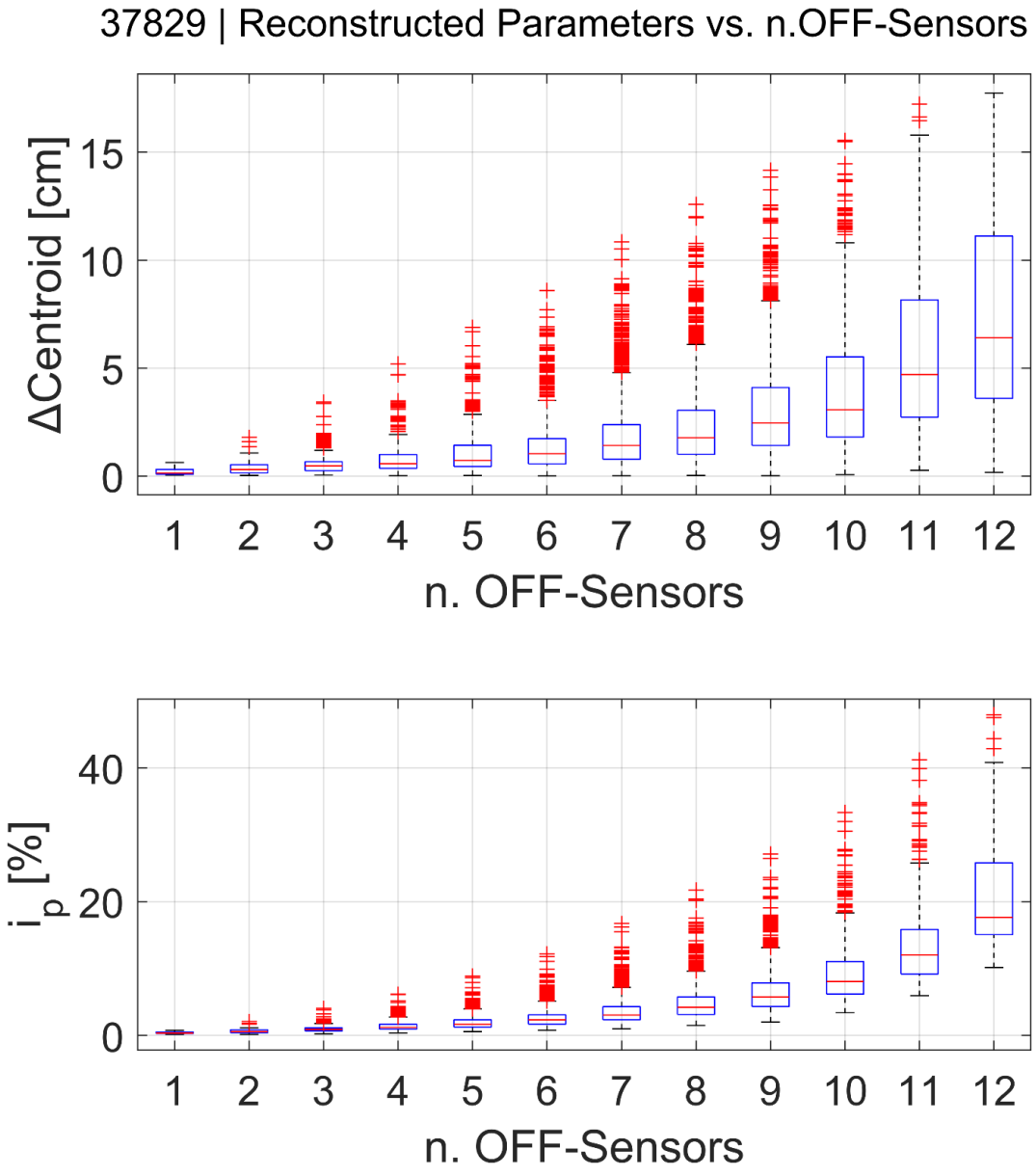

Fig. B.13: *Shot 37829*: Box-plot

Shot DEMO-like δ_L

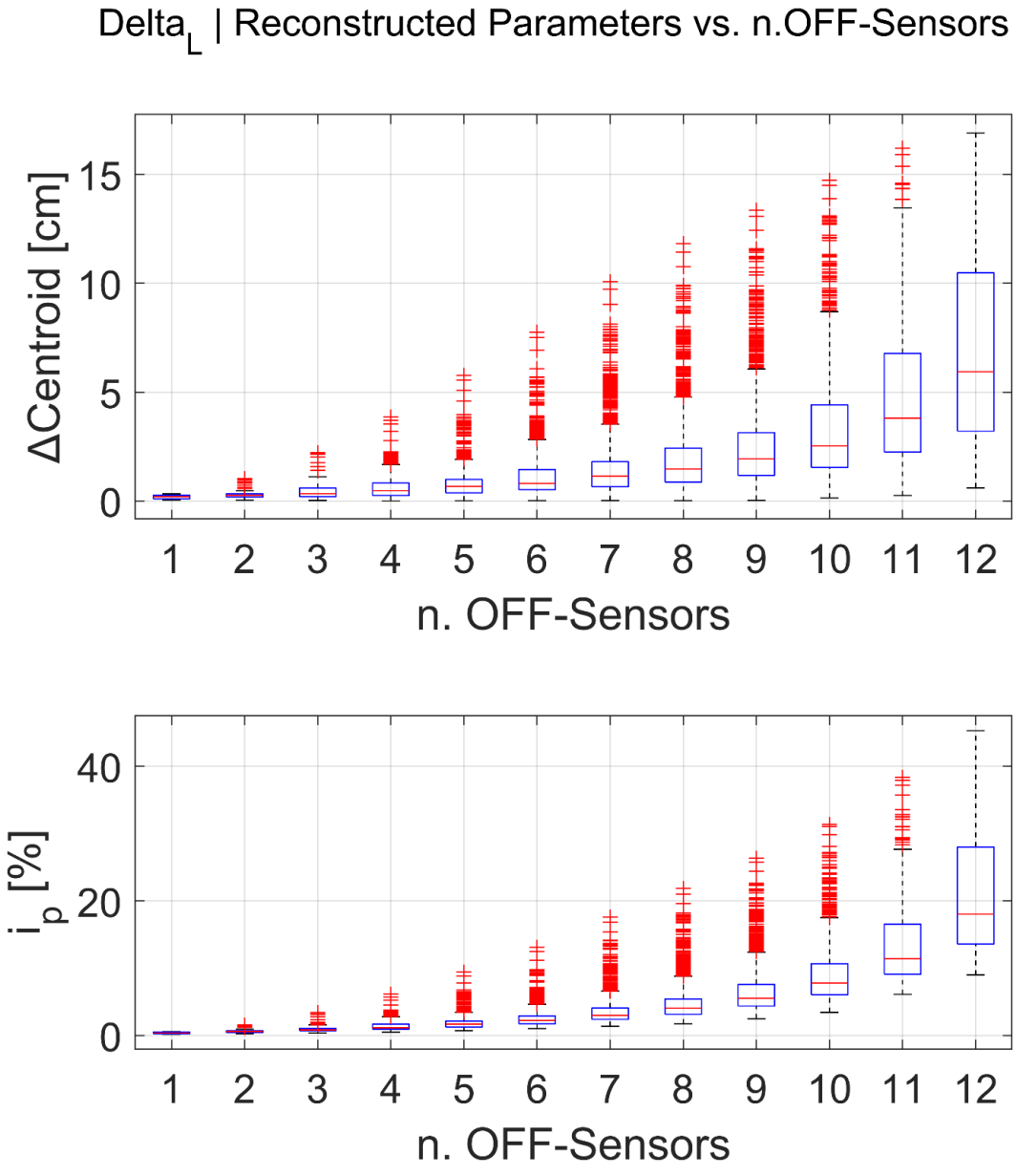

Fig. B.14: *Shot* δ_L: Box-plot

Shot NT_L

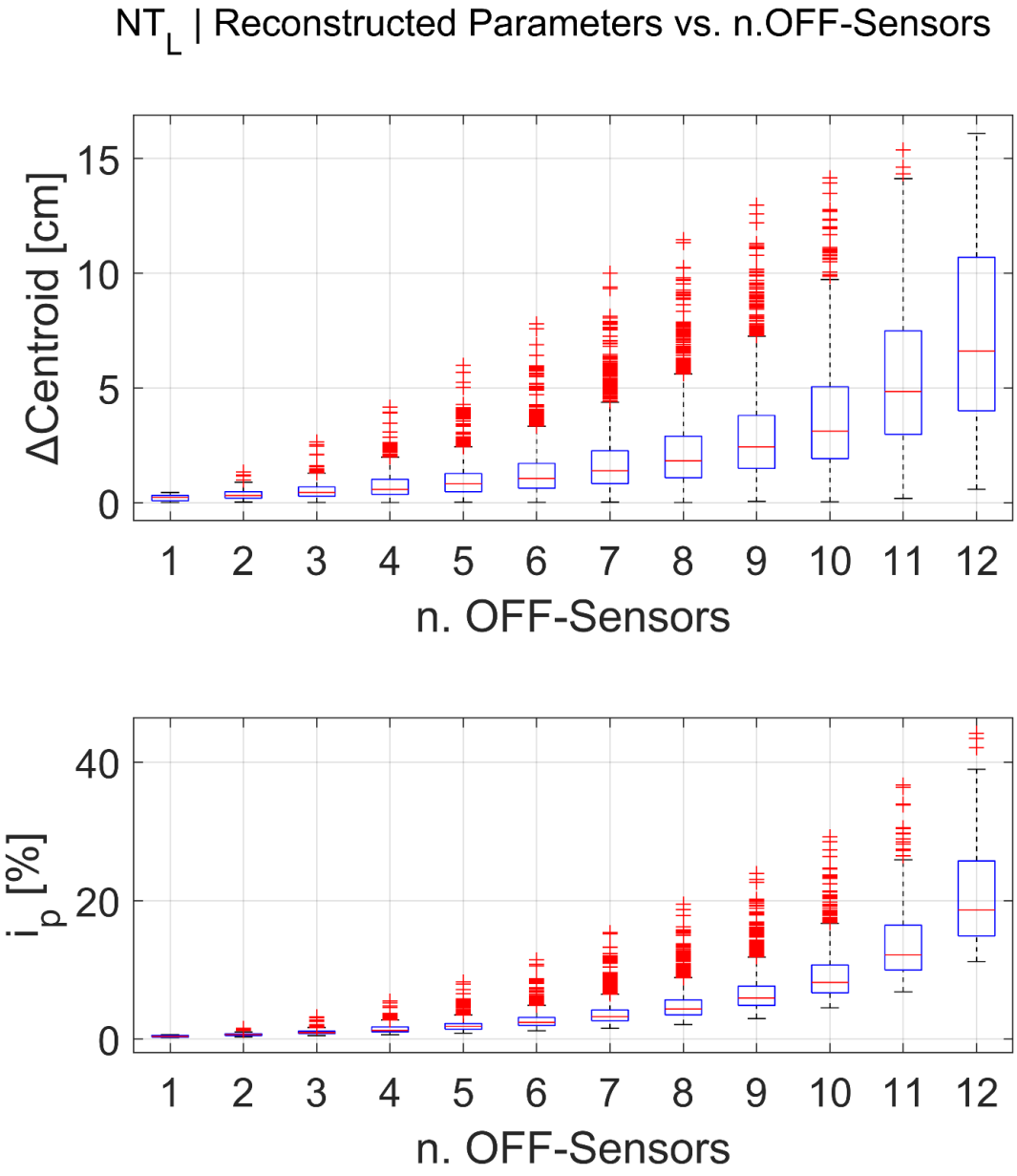

Fig. B.15: *Shot NT_L*: Box-plot

B.3 ΔCentroid vs. I_p error

Shot 39122

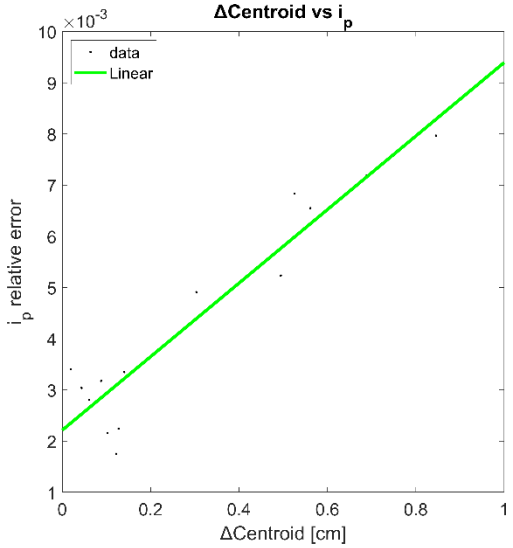

Fig. B.16a: *Shot 39122* – 1 sensor off: $\Delta C\ vs\ i_p\%$

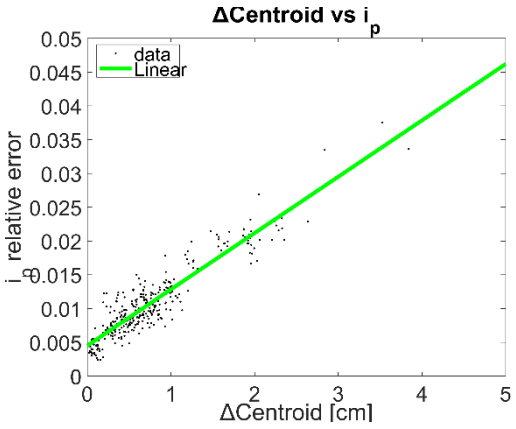

Fig B.16b: *Shot 39122* – 3 sensors off: $\Delta C\ vs\ i_p\%$

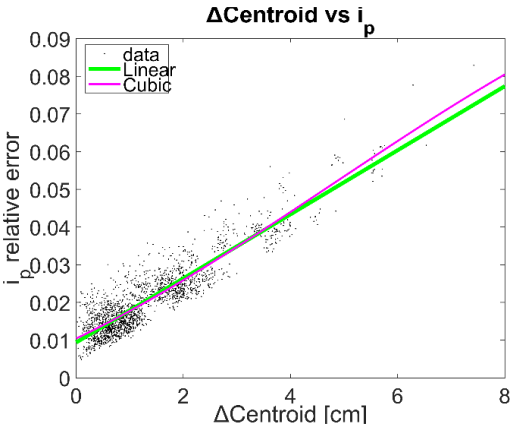

Fig. B.16c: *Shot 39122* – 5 sensors off: $\Delta C\ vs\ i_p\%$

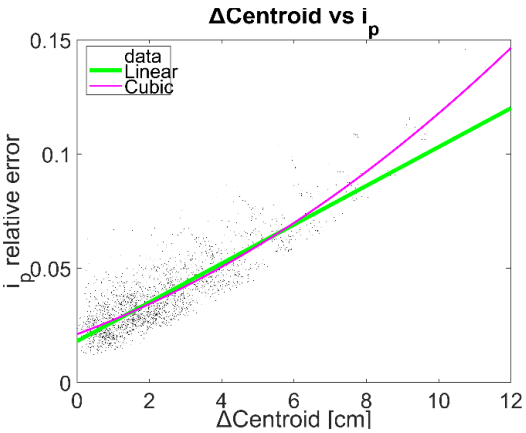

Fig B.16d: *Shot 39122* – 7 sensors off: $\Delta C\ vs\ i_p\%$

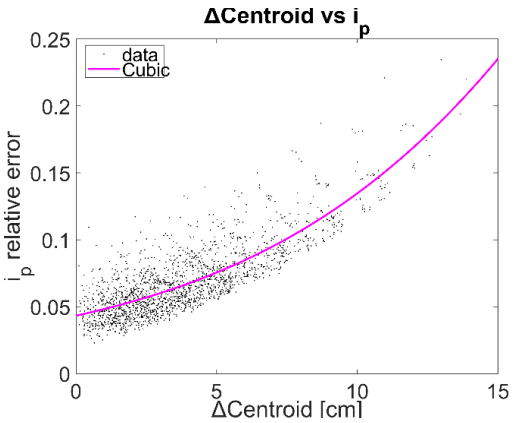

Fig. B.16e: *Shot 39122* – 9 sensors off: $\Delta C\ vs\ i_p\%$

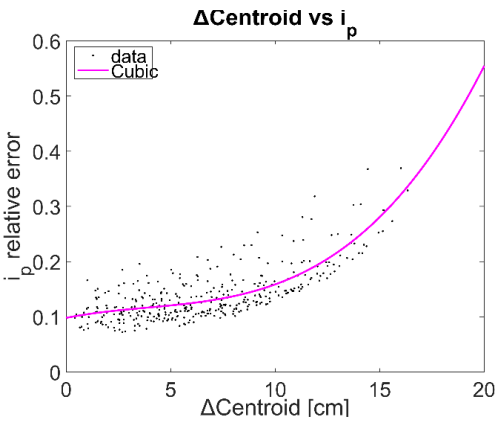

Fig B.16f: *Shot 39122* – 11 sensors off: $\Delta C\ vs\ i_p\%$

Shot 36922

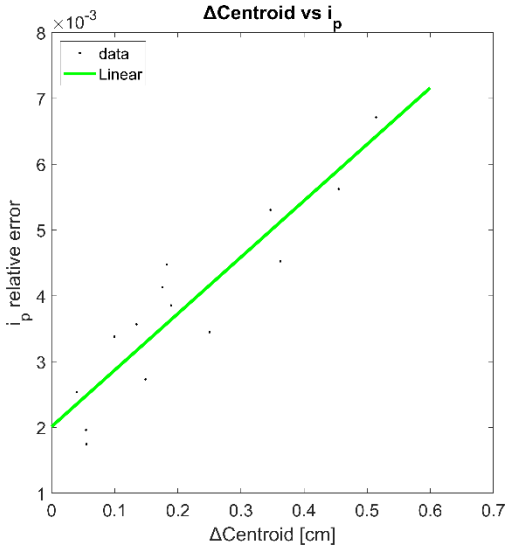

Fig. B.17a: *Shot 36922* – 1 sensor off: $\Delta C\ vs\ i_p\%$

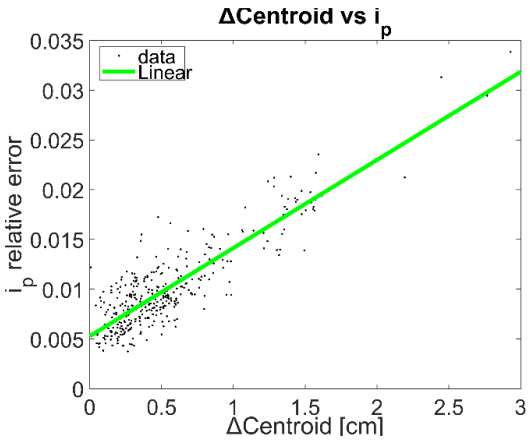

Fig B.17b: *Shot 36922*– 3 sensors off: $\Delta C\ vs\ i_p\%$

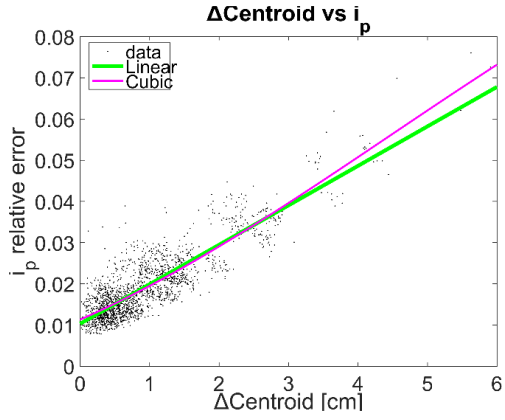

Fig. B.17c: *Shot 36922* – 5 sensors off: $\Delta C\ vs\ i_p\%$

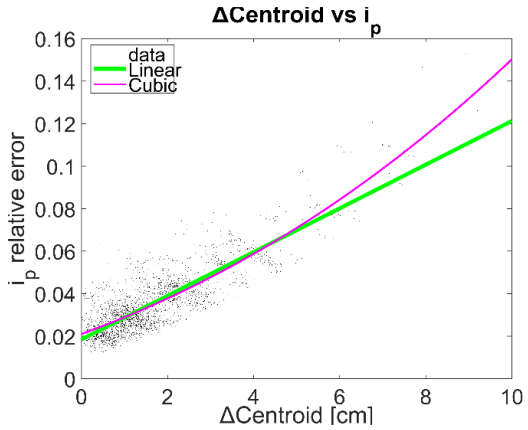

Fig B.17d: *Shot 36922*– 7 sensors off: $\Delta C\ vs\ i_p\%$

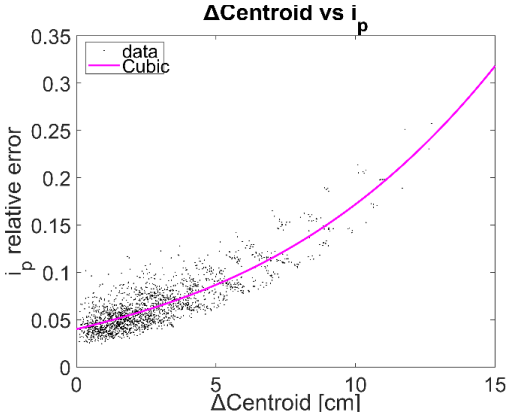

Fig. B.17e: *Shot 36922* – 9 sensors off: $\Delta C\ vs\ i_p\%$

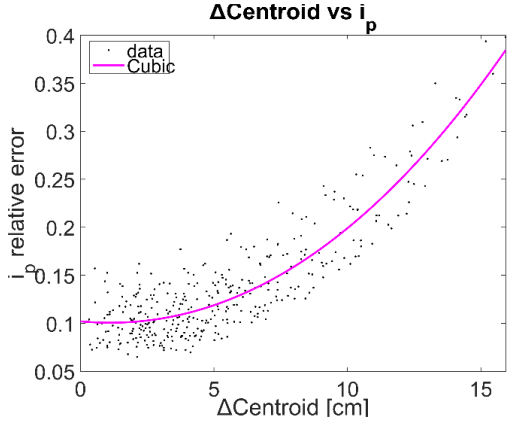

Fig B.17f: *Shot 36922* – 11 sensors off: $\Delta C\ vs\ i_p\%$

Shot 37829

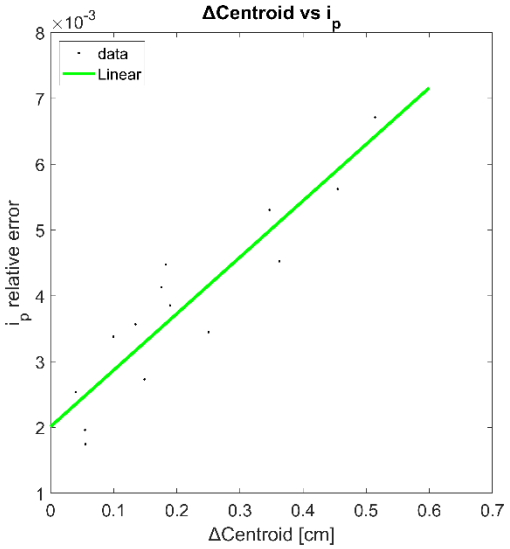

Fig. B.18a: *Shot 37829* – 1 sensors off: $\Delta C\ vs\ i_p\%$

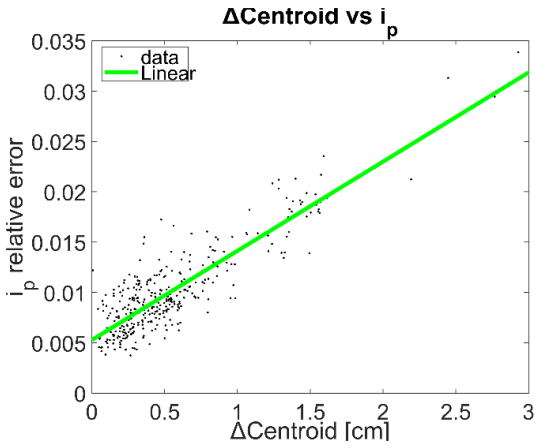

Fig B.18b: *Shot 37829* – 3 sensors off: $\Delta C\ vs\ i_p\%$

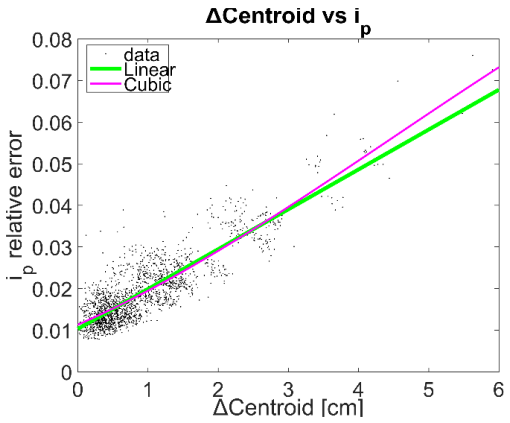

Fig. B.18c: *Shot 37829* – 5 sensors off: $\Delta C\ vs\ i_p\%$

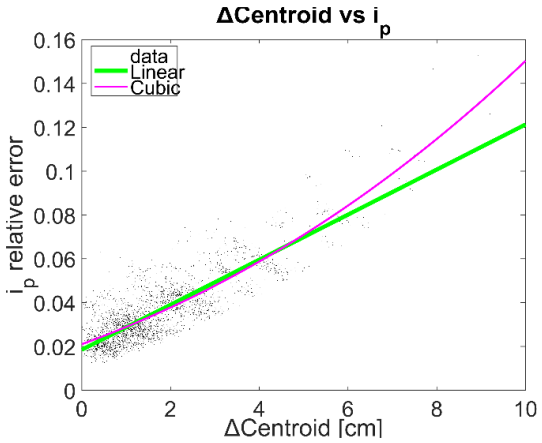

Fig B.18d: *Shot 37829* – 7 sensors off: $\Delta C\ vs\ i_p\%$

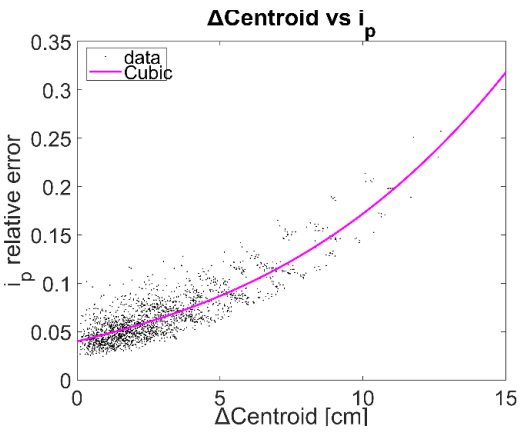

Fig. B.18e: *Shot 37829* – 9 sensors off: $\Delta C\ vs\ i_p\%$

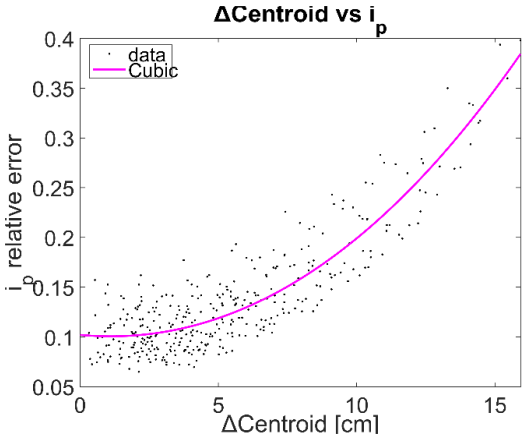

Fig B.18f: *Shot 37829* – 11 sensors off: $\Delta C\ vs\ i_p\%$

Shot DEMO-like δ_L

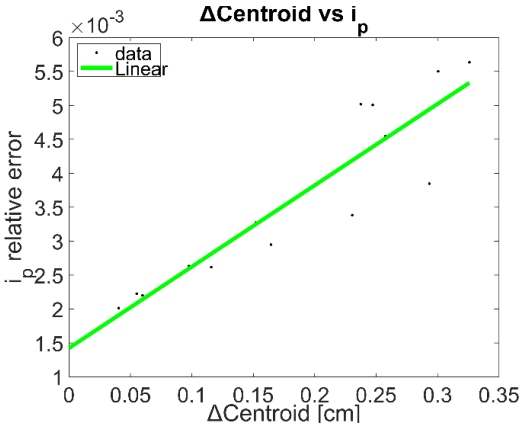

Fig. B.19a: *Shot* δ_L– 1 sensors off: ΔC *vs* i_p%

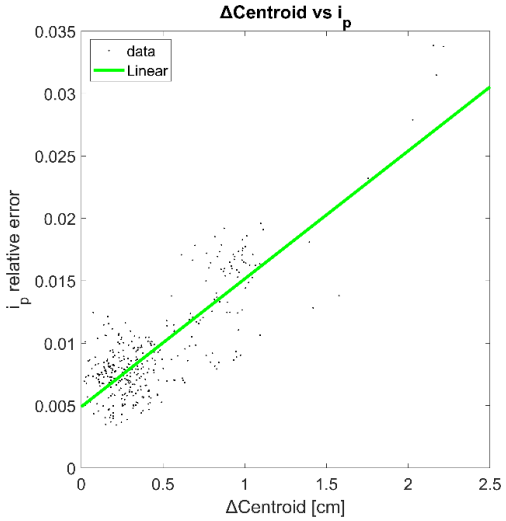

Fig B.19: *Shot* δ_L – 3 sensors off: ΔC *vs* i_p%

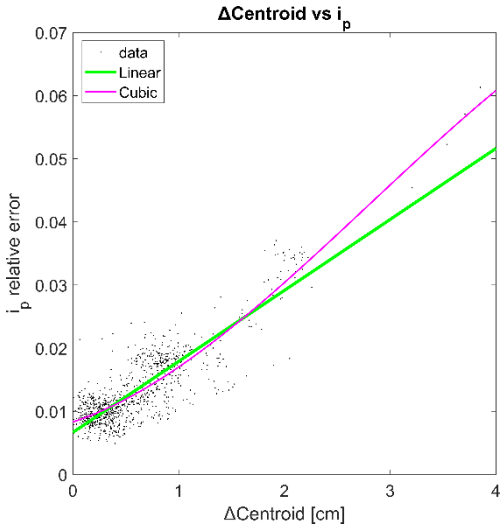

Fig. B.19c: *Shot* δ_L – 4 sensors off: ΔC *vs* i_p%

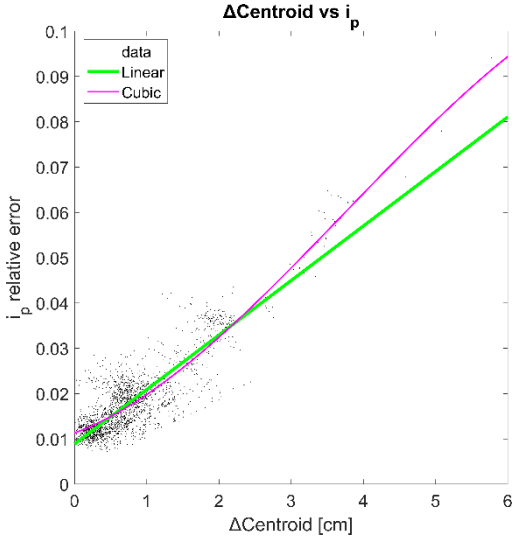

Fig B.19d: *Shot* δ_L – 5 sensors off: ΔC *vs* i_p%

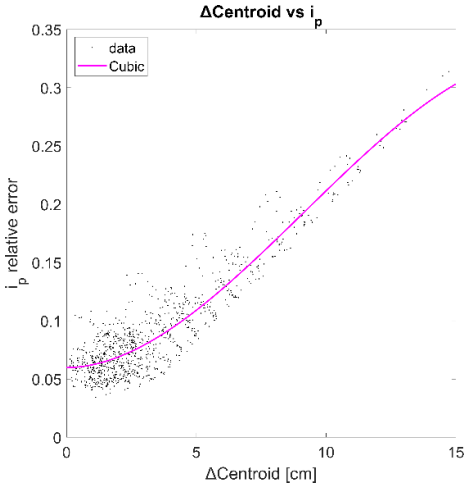

Fig. B.19e: *Shot* δ_L – 10 sensors off: ΔC *vs* i_p%

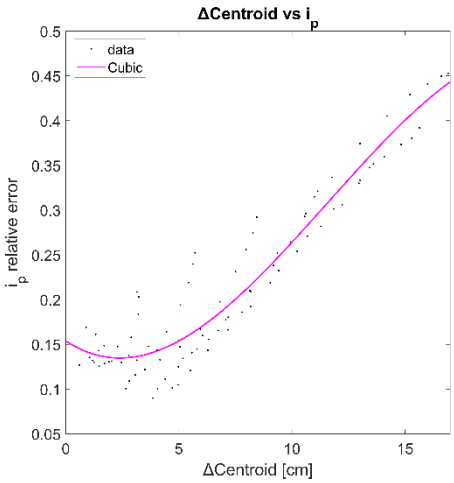

Fig B.19f: *Shot* δ_L – 12 sensors off: ΔC *vs* i_p%

Shot NT_L

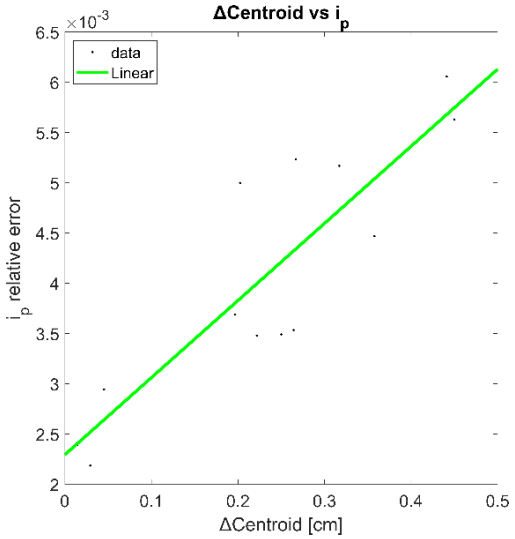

Fig. B.20a: *Shot* NT_L – 1 sensors off: $\Delta C\ vs\ i_p\%$

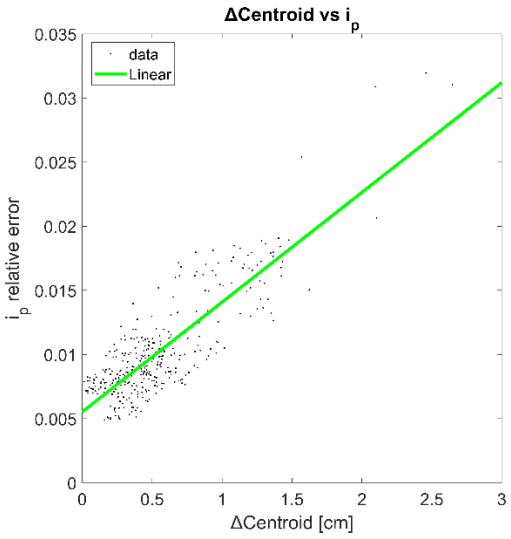

Fig B.20b: *Shot* NT_L – 3 sensors off: $\Delta C\ vs\ i_p\%$

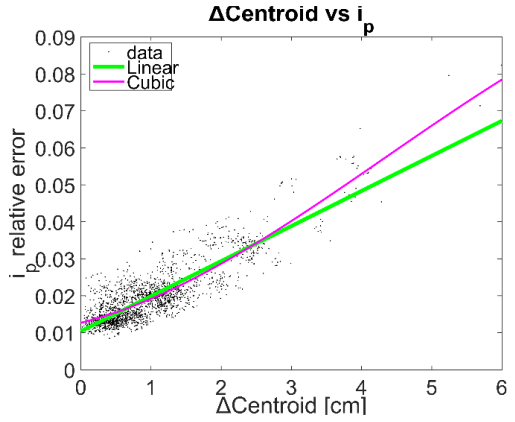

Fig. B.20c: *Shot* NT_L – 5 sensors off: $\Delta C\ vs\ i_p\%$

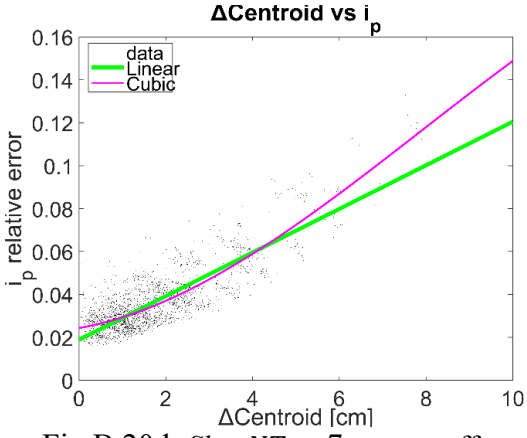

Fig B.20d: *Shot* NT_L – 7 sensors off: $\Delta C\ vs\ i_p\%$

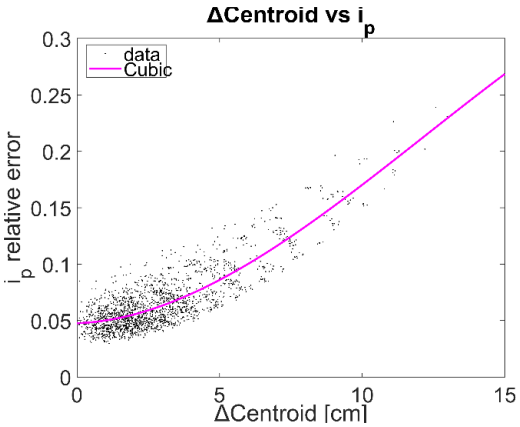

Fig. B.20e: *Shot* NT_L – 9 sensors off: $\Delta C\ vs\ i_p\%$

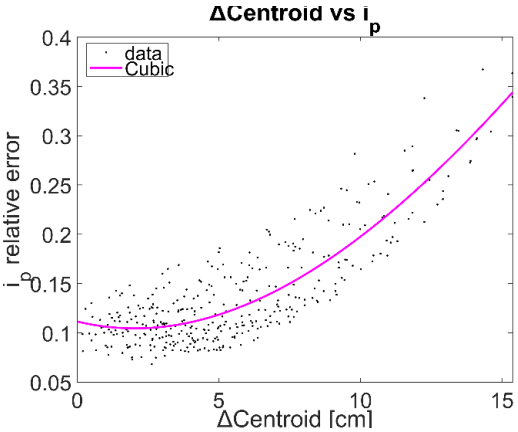

Fig B.20fb: *Shot* NT_L – 11 sensors off: $\Delta C\ vs\ i_p\%$

B.4 Noise Analysis

Shot 39122 (1 sensor off)

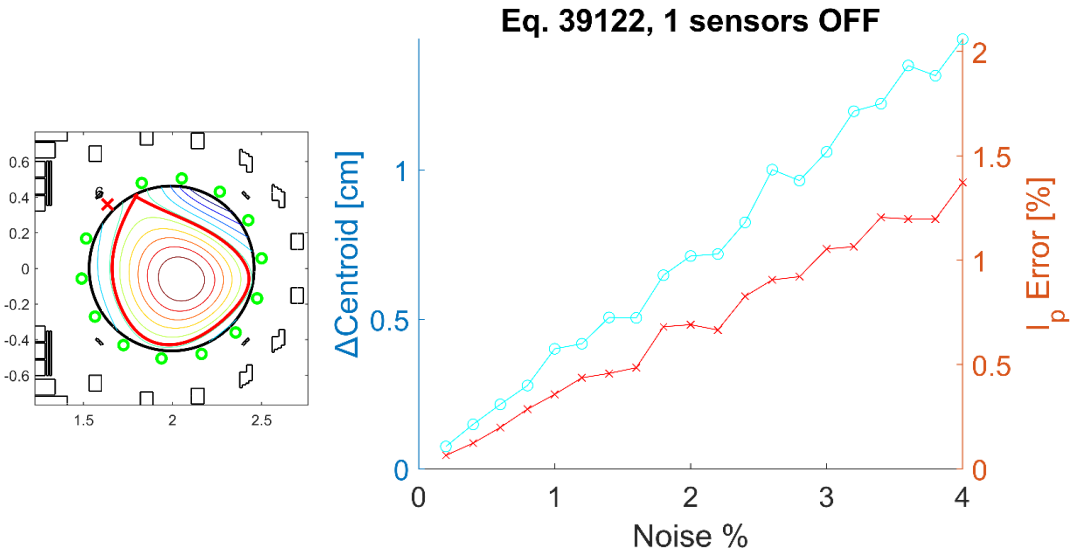

Fig. B.21a: *Shot 39122*, 1 sensor off, best case, noise analysis

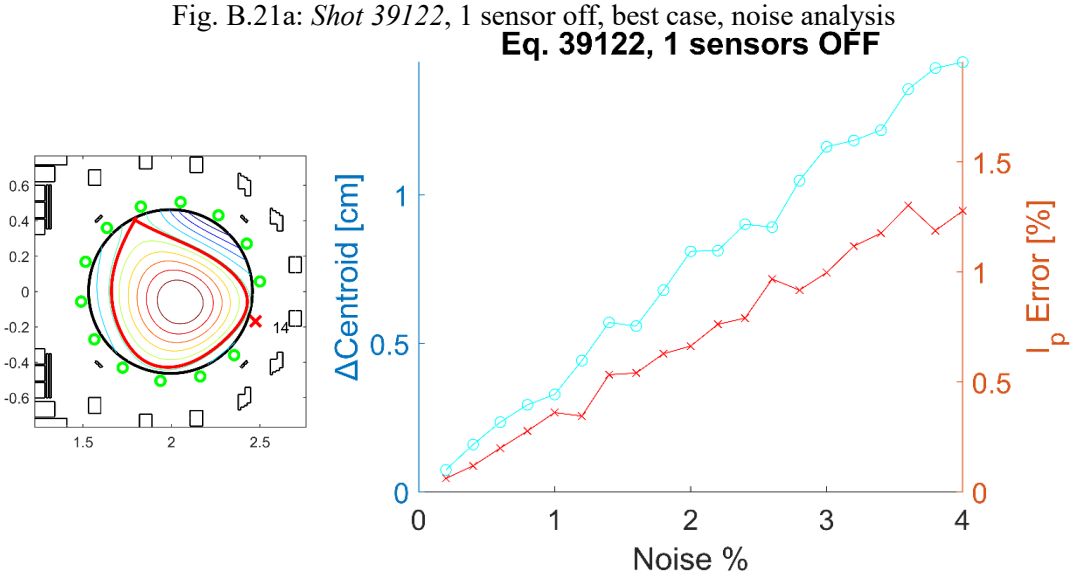

Fig. B.21b: *Shot 39122*, 1 sensor off, worst case, noise analysis

Shot 39122 (7 sensors off)

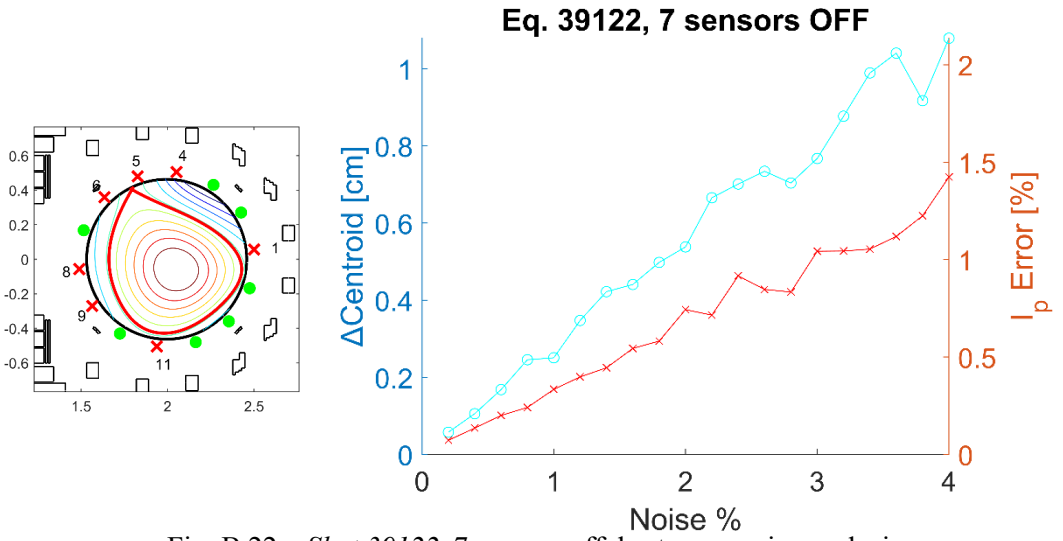

Fig. B.22a: *Shot 39122*, 7 sensors off, best case, noise analysis

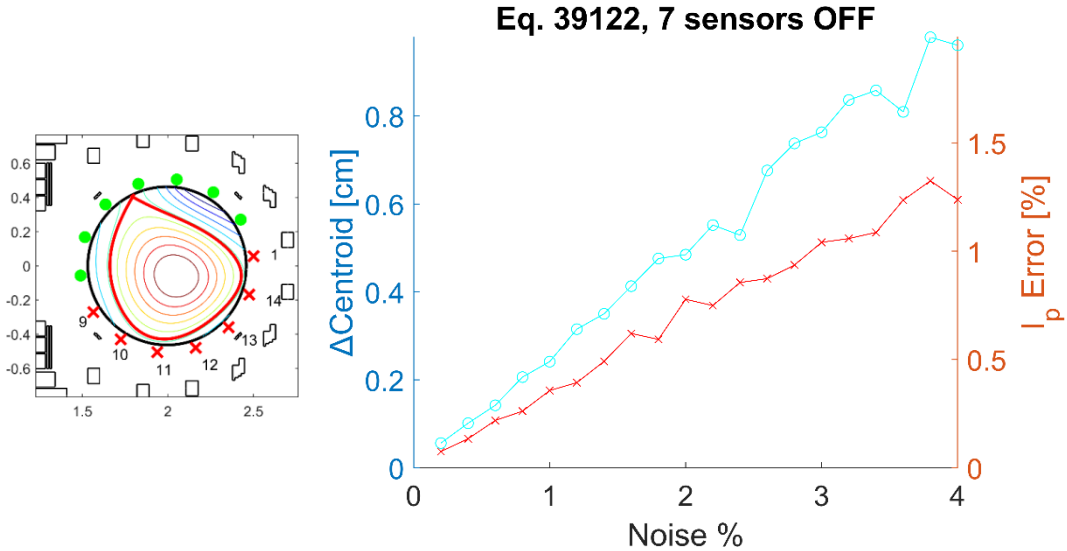

Fig. B.22b: *Shot 39122*, 7 sensors off, worst case, noise analysis

Shot 36922 (1 sensor off)

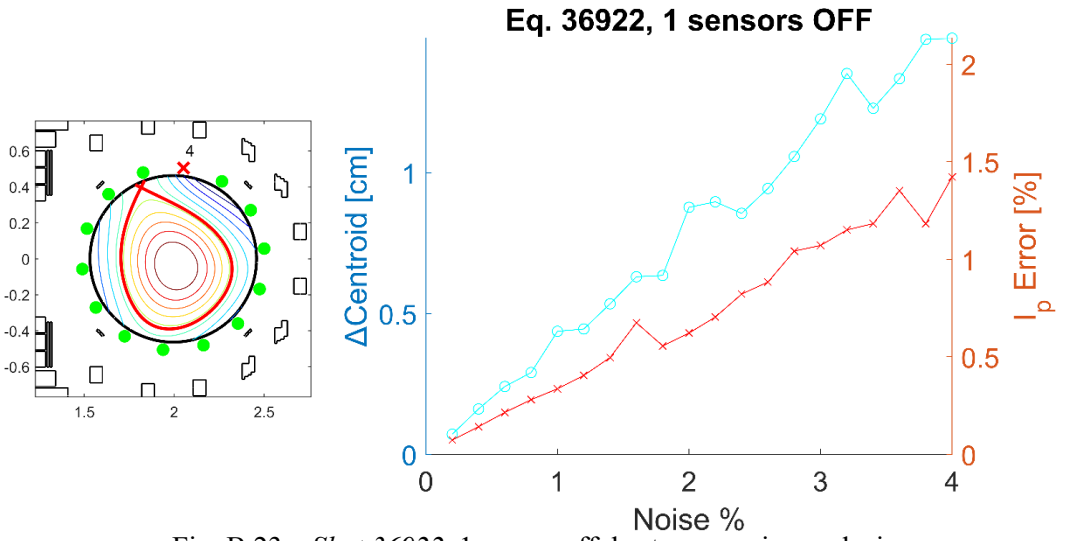

Fig. B.23a: *Shot 36922*, 1 sensor off, best case, noise analysis

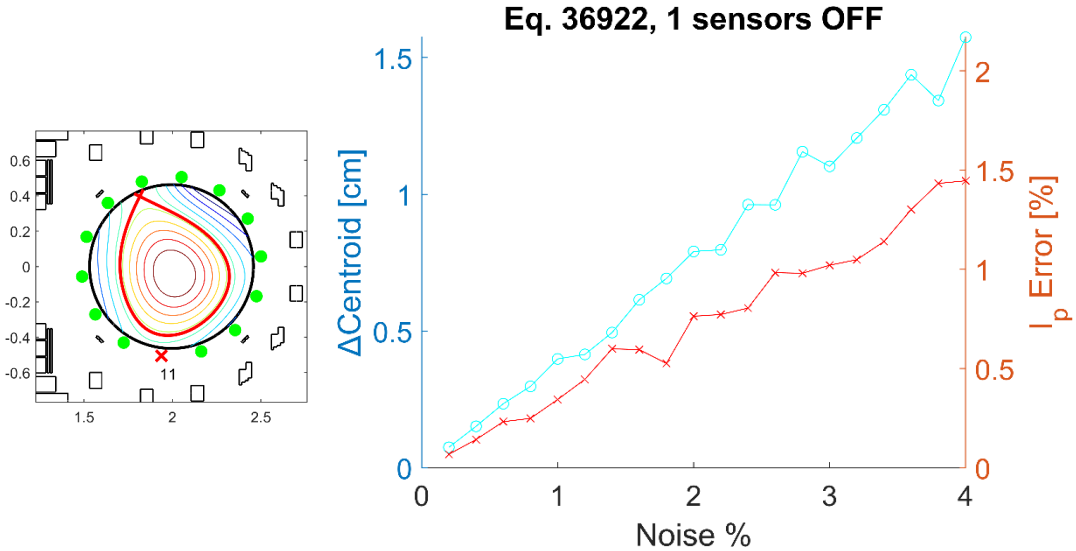

Fig. B.23b: *Shot 36922*, 1 sensor off, worst case, noise analysis

Shot 36922 (7 sensors off)

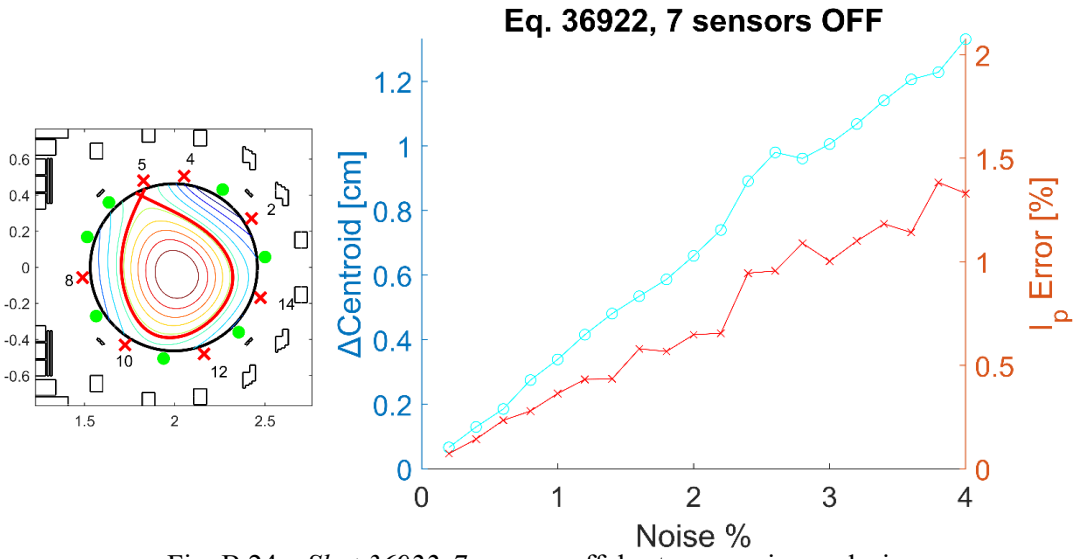

Fig. B.24a: *Shot 36922*, 7 sensors off, best case, noise analysis

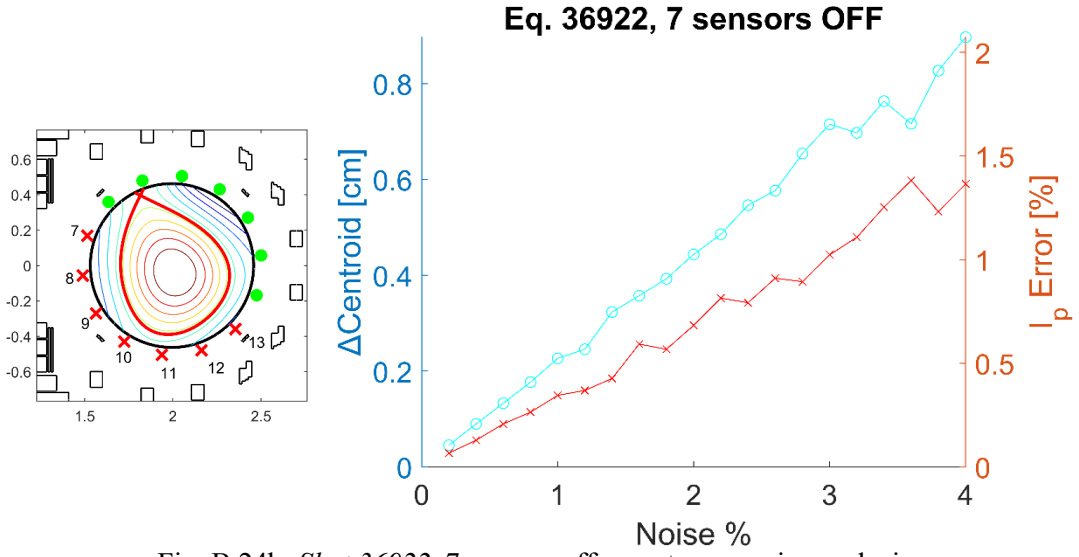

Fig. B.24b: *Shot 36922*, 7 sensors off, worst case, noise analysis

Shot 37829 (1 sensor off)

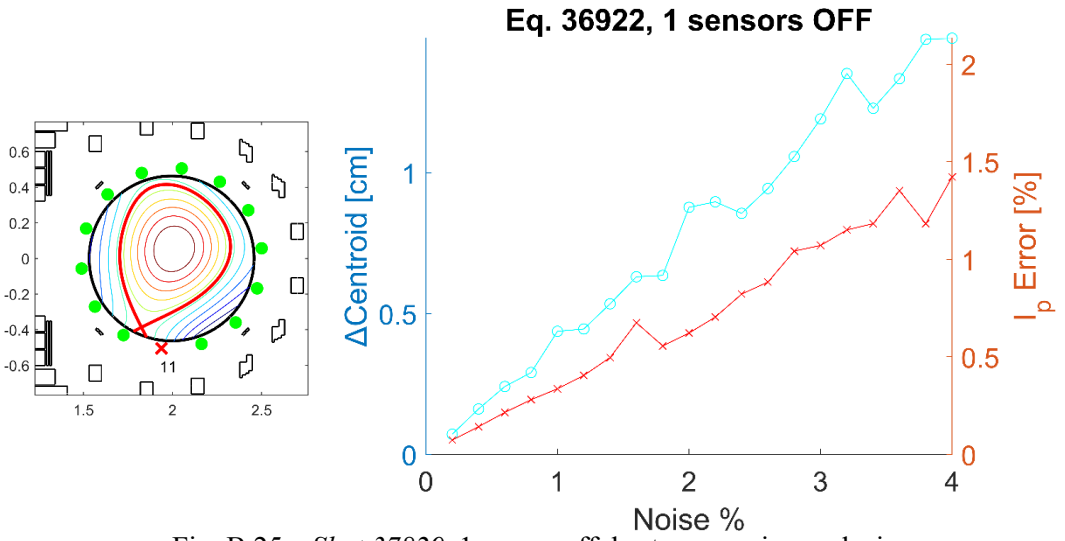

Fig. B.25a: *Shot 37829*, 1 sensor off, best case, noise analysis

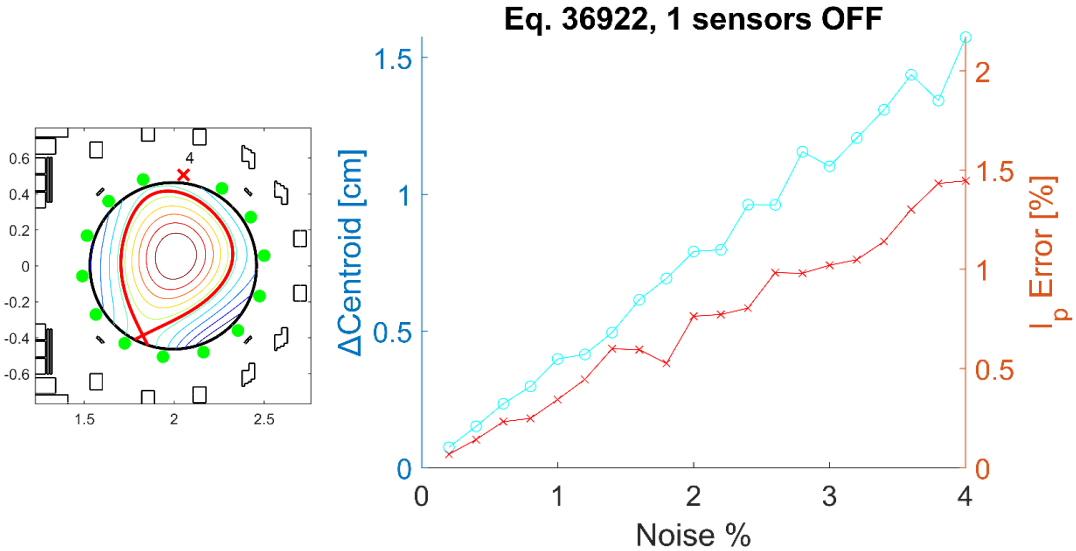

Fig. B.25b: *Shot 37829*, 1 sensor off, worst case, noise analysis

Shot 37829 (7 sensors off)

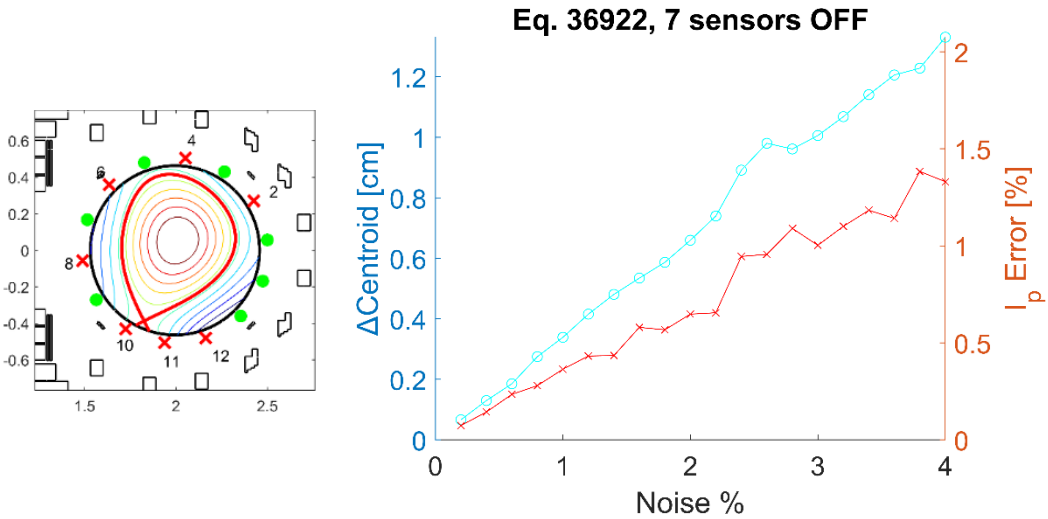

Fig. B.26a: *Shot 37829*, 7 sensors off, best case, noise analysis

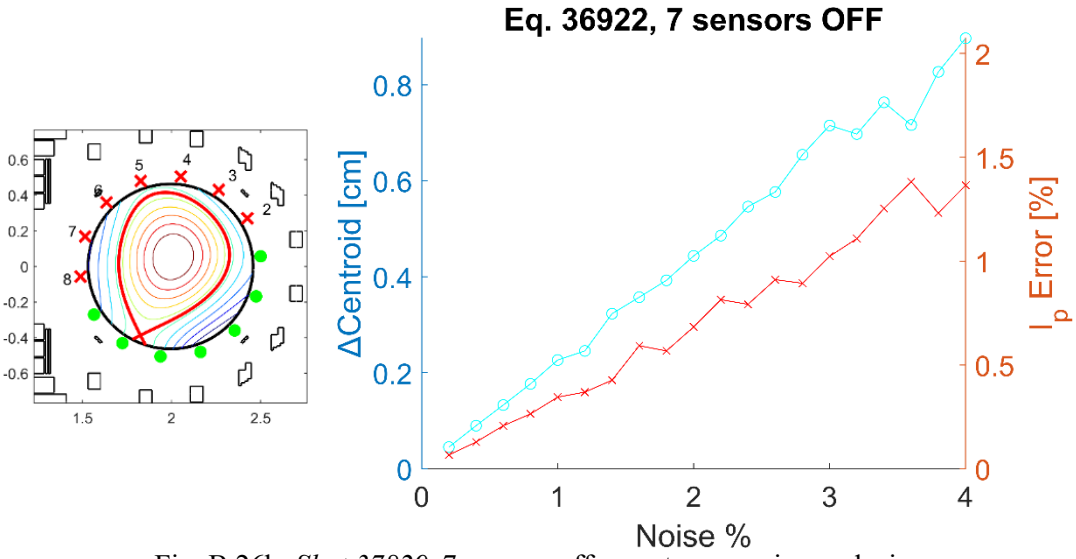

Fig. B.26b: *Shot 37829*, 7 sensors off, worst case, noise analysis

Shot DEMO-like δ_L (1 sensor off)

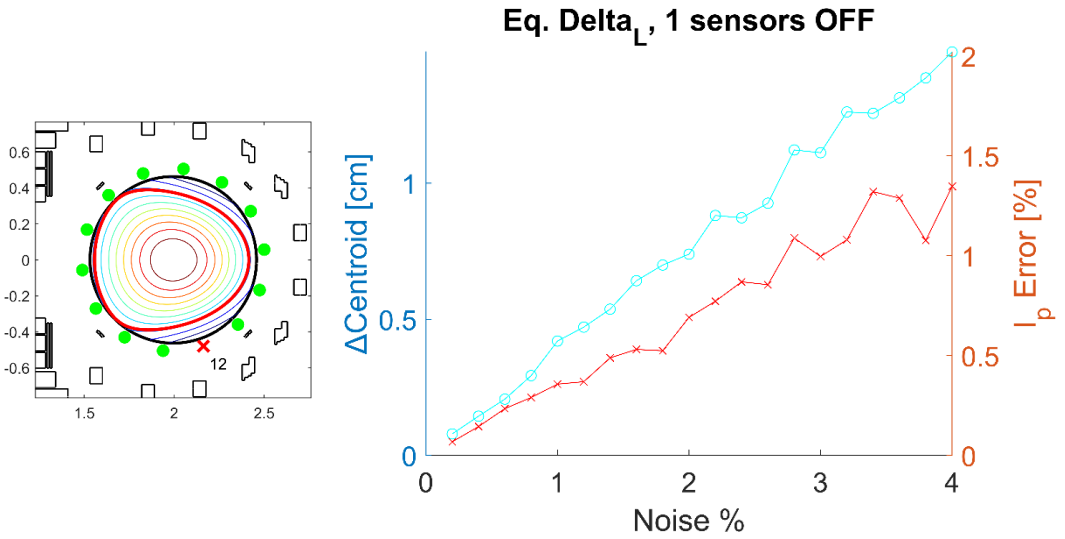

Fig. B.27a: *Shot* δ_L, 1 sensor off, best case, noise analysis

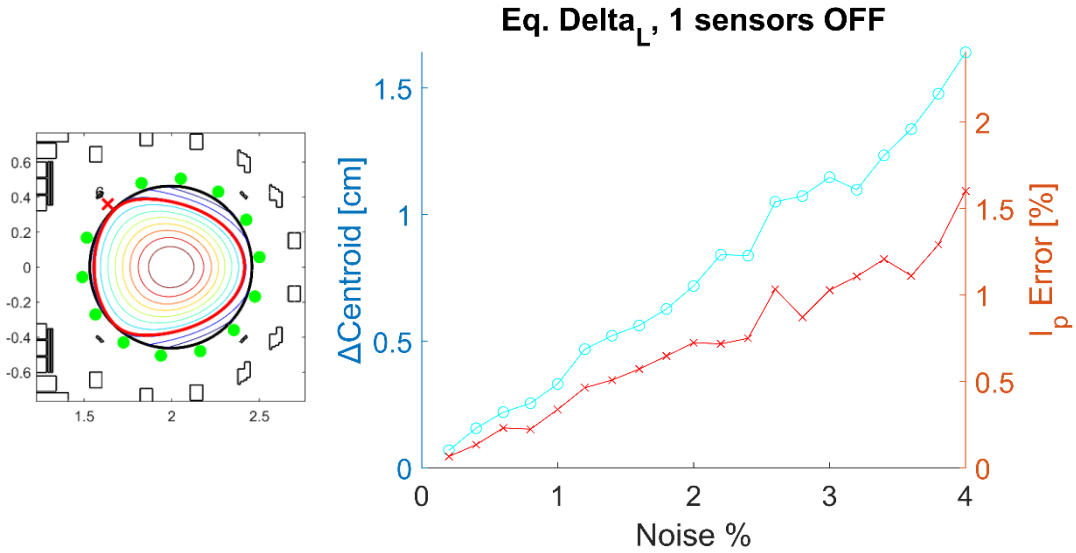

Fig. B.27b: *Shot* δ_L, 1 sensor off, worst case, noise analysis

Shot DEMO-like δ_L (7 sensor off)

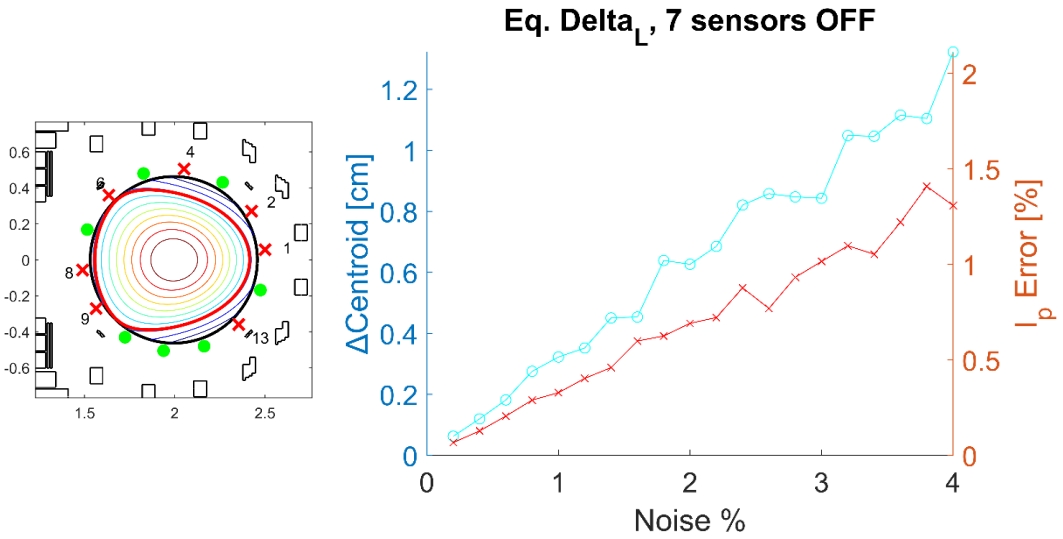

Fig. B.28a: *Shot* δ_L, 7 sensors off, best case, noise analysis

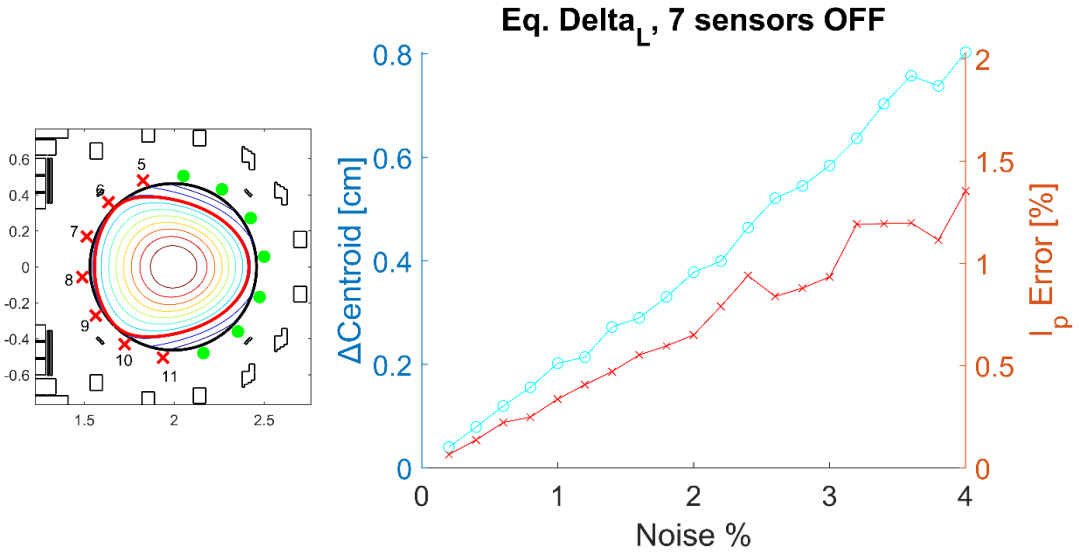

Fig. B.28b: *Shot* δ_L, 7 sensors off, worst case, noise analysis

Shot NT_L (1 sensor off)

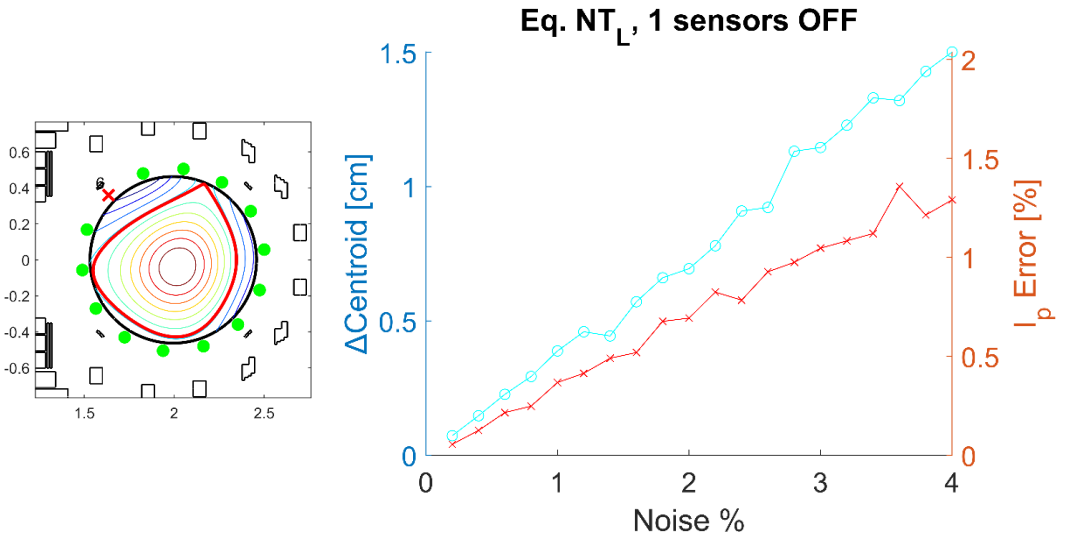

Fig. B.29a: *Shot* NT_L, 1 snsor off, best case, noise analysis

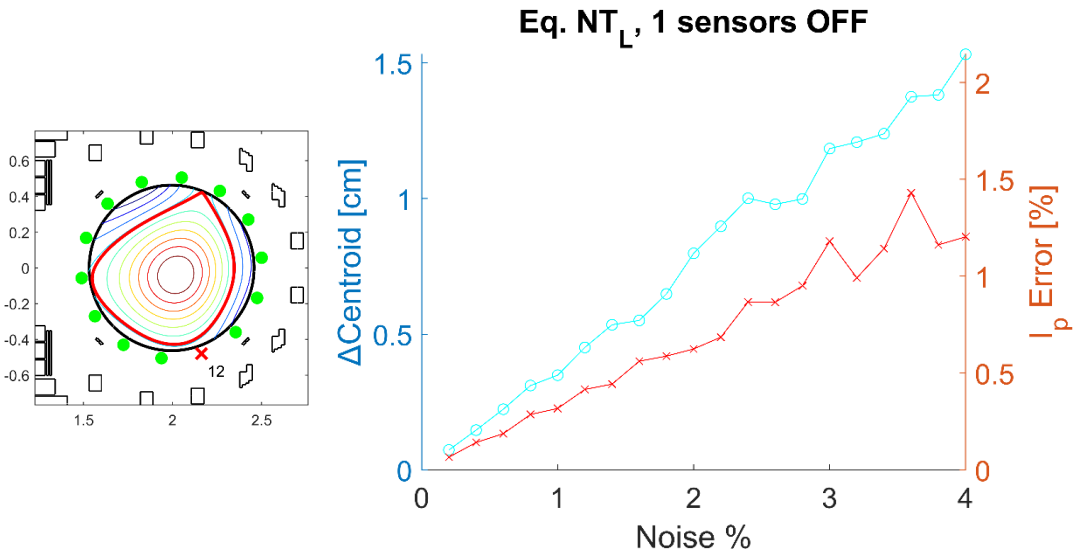

Fig. B.29b: *Shot* NT_L, 1 sensor off, worst case, noise analysis

Shot NT_L (7 sensors off)

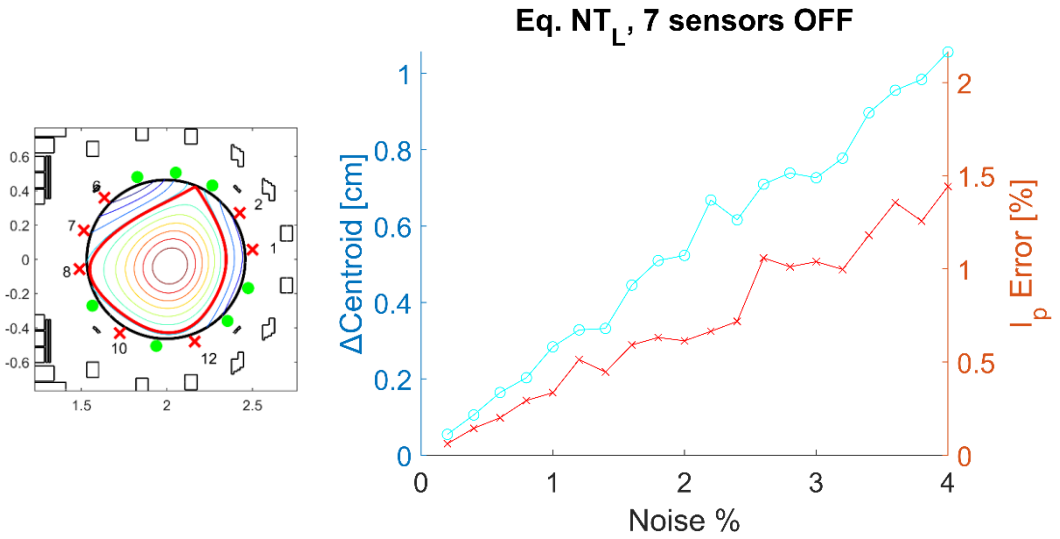

Fig. B.30a: *Shot NT_L*, 7 sensors off, best case, noise analysis

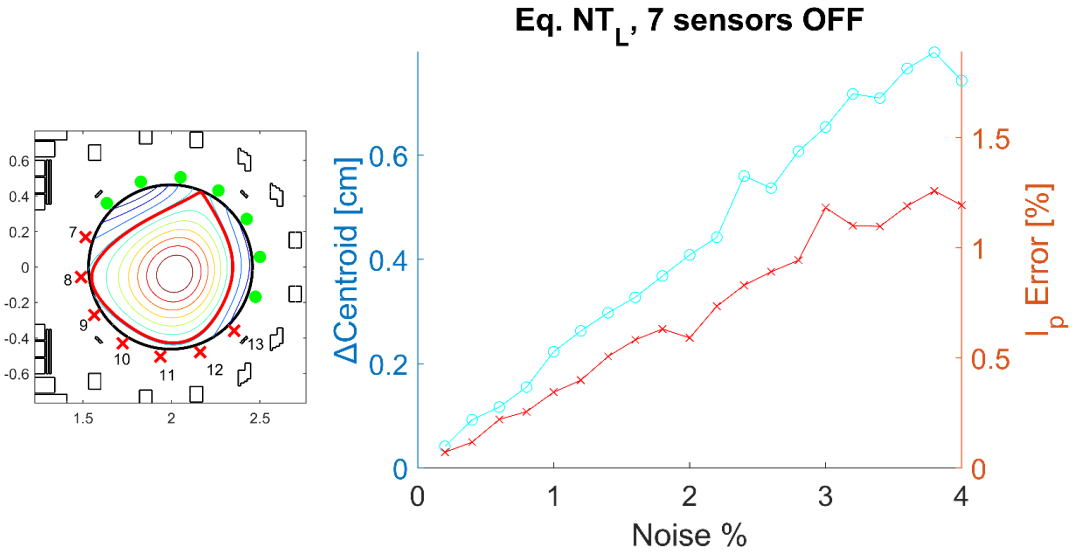

Fig. B.30b: *Shot NT_L*, 7 sensors off, worst case, noise analysis

List of Figures

List of Figures

Bibliography

[1]. IEA, *World Energy Outlook 2021*, 2021, Paris

[2]. IRENA, *Renewables Capacity Statistics 2021,* 2021

[3]. C. Bustreo, G. Meneghini, C. Petrocvich, G. Zollino, I. Vignotto, *Comparing energy scenarios by means of ternary diagrams*, 2015

[4]. Samuel J. Ling, *Nuclear Binding Energy*, University Physics, Volume 3, 2019

[5]. M. Höök, X.Tang, *Depletion of fossil fuels and anthropogenic climate change – A review*, Energy Policy, Volume 52, 2013, Pages 797-809

[6]. Rubel M., *Fusion Neutrons: Tritium Breeding and Impact on Wall Materials and Components of Diagnostic Systems*, Pages 1-3, Journal of Fusion Energy (2019) 38:315–329

[7]. INFCE, *Heavy water requirements and availability*, Chapters 4 and 5, 1979

[8]. J. Friedberg, *Plasma Physics and Fusion Energy*, Cambridge University Press, 2007

[9]. J. Ongena, R.Koch, R.Wolf, H. Zohm, *Magnetic-confinement fusion*, Nature Physics, 2016

[10]. J. Wesson, D.J. Campbell, *Tokamaks*, 4th Edition, Oxford University Press, 2011

[11]. H.A.B. Bodin, *The reversed field pinch*, Nuclear Fusion 30, 1990

[12]. L. Marelli et al., *The reversed field pinch - Review*, Nuclear Fusion 61, 2021

[13]. J. Friedberg, *Ideal MHD*, Cambridge University Press, 2014

[14]. M. Bonotto, D. Abate, P.Bettini, F. Villone, *A coupled FEM-BEM approach for the solution of the free-boundary axi-symmetric plasma equilibrium problem*, Communications in Computational Physics, Vol 31, 2022, 27-59

[15]. K. Lackner, *Computation of ideal MHD equilibria*, Computer Physics Communications, vol. 12, no. 1, pp. 33 – 44, 1976.

[16]. C. Geuzaine and J.-F. Remacle, *Gmsh: A 3-D finite element mesh generator with built-in pre- and post-processing facilities*, International Journal for Numerical Methods in Engineering, vol. 79, pp. 1309 – 1331, 09 2009.

[17]. M. Bonotto, *Calcolo dei momenti di corrente per la ricostruzione in tempo reale della frontiera di plasma*, Tesi di Laurea Magistrale in Ingegneria Elettrica, Università di Padova, 2015

[18]. G. Rostagni, *RFX: an expected step in RFP research*, Fusion Engineering and Design 25, 1995

[19]. L. Marelli et al., *Upgrades of the RFX-mod reversed field pinch and expected scenario improvements*, Nuclear Fusion 69, 2019

[20]. S. Peruzzo et al., *Detailed design of the RFX-mod2 machine load assembly*, Fusion Engineering and Design 136, 2018

[21]. S. Peruzzo et al., *Technological challenges for the design of the RFX-mod2 experiment*, Fusion Engineering and Design 146, 2019

[22]. A. Stella, M. Guarnieri, F. Bellina, P.P. Campostrini, G. Chitarin, F. Trevisan, P. Zaccaria, *The RFX magnet system*, Fusion Engineering and Design 25, 1995, 393-399

[23]. F. Bellina, G. Chitarin, M. Guarnieri, A. Stella, *The RFX Field Shaping Winding Design*, IEEE Transactions on magnetics, Vol 24, n. 2, 1988

[24]. D. Abate, G. Marchiori, P. Bettini, F. Villone, *Modelling of RFX-mod2 tokamak equilibria with DEMO-like shape conditions and negative triangularity*, Plasma Physics and Controlled Fusion 62, 2020

[25]. MATLAB, *Controlling random number generation*, MATLAB User's Guide, The MathWorks, 2011